Understanding the Intergranular Stress Corrosion Cracking of an Al-Mg Alloy

---

A Thesis

Presented to

the faculty of the School of Engineering and Applied Science

University of Virginia

---

in partial fulfillment

of the requirements for the degree

Master of Science

in Materials Science and Engineering

By

Gabriella Annette Marino

May 2024

Approval Sheet

This Thesis is submitted in partial fulfillment of the requirements for the degree of

Master of Science

in Materials Science and Engineering

Author: Gabriella Marino

This Thesis has been read and approved by the examining committee:

Advisor: Dr. James Burns

Committee Member: Dr. Robert Kelly

Committee Member: Dr. Sean Agnew

Accepted for the School of Engineering and Applied Science:

Jennifer L. West

Dean, School of Engineering and Applied Science

May 2024

Abstract

Al-Mg alloys have historically been used in a variety of different engineering applications. These alloys are strengthened using work hardening and solid solution strengthening via Mg supersaturation (above 3 wt% Mg). When these alloys are exposed to sufficiently elevated temperatures, the thermodynamically stable β phase (Al_3Mg_2) precipitates primarily along the grain boundaries in a process known as sensitization. Sensitized Al-Mg alloys are therefore susceptible to grain boundary attack such as intergranular corrosion (IGC) or intergranular stress corrosion cracking (IGSCC) when also exposed to an electrolyte because of the known potential difference that exists between the anodic β phase and the surrounding α-Al matrix. This behavior has been extensively studied and is well understood.

IGC and IGSCC can cause pre-mature failures of engineering components, as such, significant work has been performed to understand the susceptibility of Al-Mg alloys to specific environmental conditions. Utilizing linear elastic fracture mechanics (LEFM) testing, knowledge gained from laboratory tests can easily be transferred to in-service engineering components exposed to the same mechanical driving force and environmental conditions by the principle of similitude. The LEFM testing approach has also been used to give mechanistic insights on the crack growth of these alloys. Recent studies have proposed an anodic dissolution enabled hydrogen embrittlement mechanism, where anodic dissolution of the β phase (from the electrochemical potential difference of the α and β) and α phase (from exposure of the bare metal to the corrosive electrolyte) releases Al^{3+} and Mg^{2+} ions into solution. These ions combine with surrounding water molecules to enable hydrolysis where H^+ is formed as a product. Chloride ingress into the crack tip and a low pH promote an aggressive crack tip chemistry which also induces hydrogen (H) production. This hydrogen is first adsorbed onto the surface of the material and then adsorbed into the material at the crack tip. Diffusion of the hydrogen into the fracture process zone enables local embrittlement of the grain boundary and/or the β/Al-matrix interface.

This critical understanding has opened up development of mitigation strategies and informs future material development. It also helps inform the results of further testing of Al-Mg materials. The work of this thesis looks at developing a thorough understanding of an Al-Mg alloy (Alloy 1) that has not been testing using LEFM previously. Specifically, this work seeks to understand: the effect of grain directionality on the Mode I crack path, the effect of applied cathodic potential on the environment assisted cracking (EAC) kinetics, the effect of atmospheric environments (i.e. misting and wicking) compared to that of full immersion, and the effect of slightly basic, low chloride concentrated solutions on the EAC behavior compared to more acidic and higher chloride containing solutions in an atmospheric environment. All of these results are analyzed in the context of the anodic dissolution enabled hydrogen

embrittlement mechanism. Collectively, these results will inform potential mitigation strategies and root cause analysis of in-service components comprised of Alloy 1. Additionally, this work will be integrated into lifetime prediction models of in-service components.

The key results show that Alloy 1 does have an applied potential dependence, as has been observed for other Al-Mg systems previously. Specifically, cathodic applied potentials decrease the IGSCC susceptibility of Alloy 1, with complete mitigation of crack growth at an applied potential of -1100 mV_{SCE}. This allows for the development of techniques that will mitigate the susceptibility of Alloy 1 as a means of cathodic protection. The study of the grain microstructure showed that Alloy 1 had little grain directionality as compared to other Al-Mg alloys, and showed minimal effect of loading orientation on EAC kinetics. Atmospheric testing of Alloy 1 exposed to a low chloride, slightly basic solution gave enhanced crack growth kinetics over the full immersion environment because of increased oxygen transport through the thin film electrolyte. Lastly, atmospheric exposure of Alloy 1 to high chloride containing, slightly acidic solutions showed faster EAC kinetics over the more benign low chloride containing solution. However, the fastest cracking kinetics were observed during exposure to a solution of pH 2, which was explained by increased anodic current densities allowing for more active dissolution of the Al.

Acknowledgements

The research in this Thesis was funded by the National Aeronautics and Space Administration under grant numbers 80NSSC22PA549 and 80NSSC23PA628 with Jamie Womack as the Scientific Officer.

Table of Contents

List of Tables

List of Figures

Chapter 1: Introduction and Research Objectives

1.1 Critical background of 5xxx series aluminum alloys (AA)

The 5xxx series Al-Mg alloys are a robust material due to their high strength to weight ratio, good weldability, and general corrosion resistance, making them a desirable choice for structural components where material light-weighting is necessary. These materials are strengthened via work hardening and solid solution strengthening via Mg supersaturation. However, sufficient thermal exposure can cause sensitization, which occurs by Mg diffusion to the grain boundaries where the thermally stable β phase (Al_3Mg_2) precipitates. β phase precipitation along the grain boundaries is known to cause intergranular corrosion (IGC) and intergranular stress corrosion cracking (IGSCC) when exposed to aqueous chloride-containing environments [1]. These damage modes can cause pre-mature failure of in-service components.

Typically, IGC/IGSCC susceptibility is characterized via ASTM G67 [2], nitric acid mass lost testing (NAMLT). The test exposes the alloy to nitric acid and then quantifies the mass lost in mg/cm^2. This method assumes that all mass loss is due to grain boundary attack and subsequent grain fall out. The NAMLT testing is widely used and accepted as a proxy for IGC/IGSCC susceptibility; where higher NAMLT values are considered to be more sensitized and more susceptible. However, recent work demonstrated that comparison across different alloy systems is compromised by mass loss that is associated with matrix attack [3]. For example, IGSCC studies conducted on two alloys, aluminum alloy (AA) 5083 and AA5456 exhibited different levels of IGSCC susceptibility despite a consistent NAMLT result [3], displaying the limited ability to accurately determine IGSCC susceptibility. One method sought to better represent the IGSCC susceptibility by determining the linear grain boundary beta coverage, which demonstrated better correlation with IGSCC behavior than NAMLT values [3].

Testing of 5xxx series AA with linear elastic fracture mechanics (LEFM) is a powerful technique for quantifying IGSCC susceptibility. This technique captures crack growth kinetics as a function of stress intensity (K) which are easily comparable by the principle of similitude. Extensive research efforts using this technique have identified several phenomenological dependencies of IGSCC for AA5xxx including: composition [3], aging time [4], applied electrochemical potential [5], thin-film electrolytes [6], grain directionality [7], chloride concentration [5,8], and atmospheric environments [8,9]. These studies also advanced mechanistic understanding of IGSCC in AA5xxx series, providing strong evidence of a coupled anodic dissolution-hydrogen embrittlement mechanism. As the name suggests, the dual-phased mechanism begins with anodic dissolution of both the α and β phases. β dissolution is driven by the

electrochemical potential difference between the α-Al matrix and the intergranular β, while dissolution of the α phase is caused by exposure of the bare metal surface to the chloride containing electrolyte. An excess of Al^{3+} ions combined with surrounding water molecules enables hydrolysis, where H^{+} is formed as a product. These reactions promote an aggressive crack tip environment with a low pH and high [Cl-]. This local environment also promotes generation of hydrogen (atomic H), which is adsorbed onto the surface then absorbed into the material at the crack tip and diffuses into the material ahead of the crack tip enabling local embrittlement of the 1. grain boundary and/or 2. the β-matrix interface.

While significant research and understanding has been developed for common Al-Mg alloy systems used for marine applications, these efforts have largely been focused on material systems with modest Mg contents (between 4-5.2 wt%) and with rolled microstructures that exhibit a high degree of grain directionality. It is useful to explore the IGSCC behavior of other engineering relevant systems with a higher Mg content and an equiaxed grain structure. Furthermore, while the effect of electrolyte composition has been explored, these different environments were largely centered around high [Cl-] conditions due to the importance of Al-Mg systems in marine applications. However, there is an engineering justification for exploring the IGSCC behavior in different environments.

Recent research has been devoted to understanding the differences in IGSCC susceptibility of AA5xxx in atmospheric environments versus full immersion electrolyte environments [6,8,9]. These works have shown marked differences in crack growth kinetics when compared to full immersion testing because of a limiting cathodic area necessary to support anodic reactions at the crack tip. For all of these experiments, however, there has been a significant amount of chloride in the solutions exposed to the material (0.6 M and above). Additionally, the pH of these solutions is important to note because of the electrochemical equilibria of aluminum at different pH and electrochemical potential ranges, as stated by Pourbaix [10]. So, while high chloride containing, and mildly acidic solutions have been tested on AA5xxx in an atmospheric environment, it is relevant to explore the atmospheric exposure of very acidic and basic, low chloride containing solutions. These different electrolyte exposures will potentially create a different crack tip chemistry that may induce important differences in the cracking behavior; this behavior has not been studied. Together with existing data, these types of studies can enhance the expected level of IGSCC susceptibility of AA5xxx to atmospheric environments.

The mechanistic understanding of IGSCC for Al-Mg alloys is important for future alloy design and for mitigation strategies of in-service materials. The current work will aim to explore the governing mechanism in a new Al-Mg alloy (Alloy 1). This work will help to inform modeling and mitigation techniques. This work also seeks to understand the IGSCC susceptibility in targeted environments that are

relevant to in-service applications. Specifically, the effect of the electrolyte geometry (volume) and electrolyte constituents (including chloride concentration and pH) on the IGSCC susceptibility of Alloy 1 is explored.

1.2 Research Objectives

The overarching objective of this research is to determine the susceptibility of an Al-Mg alloy (Alloy 1) to IGSCC in targeted environments, specifically exploring the effect of solution chloride concentration, pH, and electrolyte geometry. No research has been conducted on Alloy 1 due to its proprietary nature and it has become essential to understand the sensitivities of this alloy to certain environmental conditions so effective mitigation strategies can be developed. Understanding these dependencies can also shed light onto the state of the in-service components based on known exposure conditions. Like any alloy system, it is important to understand the subtleties associated with the microstructure which impact macro-scale performance.

These knowledge gaps and objectives motivate the following research questions:

1. What is the role of grain directionality and sensitization on the EAC crack growth kinetics of Alloy 1?
2. Does Alloy 1 exhibit a polarization dependence similar to other Al-Mg alloys?
3. How are the crack growth kinetics influenced by coupled atmospheric environments and benign solution chemistries?
4. What is the IGSCC susceptibility of Alloy 1 to atmospheric environments and solutions with increasing chloride concentration and decreased pH?

1.3 Thesis Overview

The above research questions are addressed in individual chapters of this Thesis. Chapter 2 focuses on the characterization of Alloy 1 with respect to grain size and amount of beta phase precipitation on the grain boundaries in the as received material compared to the sensitized condition (after exposure to 100C for 14 days). This information will be critical to informing subsequent Chapters where environment assisted cracking (EAC) tests conducted via LEFM and utilizing the direct current potential difference (dcPD) method to monitor crack growth as a function of different material and environmental parameters.

Chapter 3 focuses on the potential dependence of Alloy 1, as has been studied for other similar Al-Mg systems [5,11]. Electrochemical testing of Alloy 1 and the Al_3Mg_2 beta phase is first conducted in 0.6 M NaCl. These tests expose the sample to the solution while current is measured as a function of

potential using a Biologic potentiostat. Following these experiments, LEFM tests with applied potentials ranging from -800 to -1100 mV_{SCE} are conducted to determine the effects of polarization on the IGSCC susceptibility. These tests will verify the operating IGSCC mechanism.

Chapter 4 will explore the impact of atmospheric environmental environments on the crack growth kinetics; comparisons will be made of fully immersed sample to a misting and wicking atmospheric environment. The misting environment is akin to the ASTM B117-19 [12] salt-spray test and involves continuous misting of solution on to the specimen. The wicking condition is meant to simulate conditions where the only solution exposure to the sample is within the crack. The solution used for these experiments is of low chloride concentration and is slightly basic, something which has yet to be studied in Al-Mg systems. Lastly, Chapter 5 shows a comparative study on the effect of atmospheric environments to IGSCC susceptibility of Alloy 1 for different electrolyte chemistries.

Altogether, the IGSCC performance of Alloy 1 is evaluated with specific environmental parameters. Each chapter reminds the reader of the key background points and the targeted objective, followed by a thorough description of the experimental techniques and materials used. The results are provided and discussed in the context of the proposed mechanism and suggestions that can propel future research.

References

[1] G.M. Scamans, N.J.H. Holroyd, C.D.S. Tuck, THE ROLE OF MAGNESIUM SEGREGATION IN THE INTERGRANULAR STRESS CORROSION CRACKING OF ALUMINIUM ALLOYS, 1987.

[2] Standard Test Method for Determining the Susceptibility to Intergranular Corrosion of 5XXX Series Aluminum Alloys by Mass Loss After Exposure to Nitric Acid (NAMLT Test) 1, (n.d.). https://doi.org/10.1520/G0067-18.

[3] M.E. McMahon, R.L. Haines, P.J. Steiner, J.M. Schulte, S.E. Fakler, J.T. Burns, Beta phase distribution in Al-Mg alloys of varying composition and temper, Corros Sci 169 (2020). https://doi.org/10.1016/j.corsci.2020.108618.

[4] R.H. Jones, D.R. Baer, M.J. Danielson, J.S. Vetrano, Role of Mg in the Stress Corrosion Cracking of and Al-Mg Alloy, Metallurgical and Materials Transactions A 32A (2001) 1699–1711.

[5] M.E. McMahon, J.R. Scully, J.T. Burns, Mitigation of Intergranular Stress Corrosion Cracking in Al–Mg by Electrochemical Potential Control, JOM 69 (2017) 1389–1397. https://doi.org/10.1007/s11837-017-2362-2.

[6] P.J. Steiner, Z.D. Harris, C. Vicente Moraes, R.G. Kelly, J.T. Burns, Investigation of IG-SCC Growth Kinetics in Al-Mg Alloys in Thin Film Environments, Corrosion 77 (2021) 838–852. https://doi.org/10.5006/3833.

[7] M.E. McMahon, P.J. Steiner, A.B. Lass, J.T. Burns, The effect of loading orientation on the stress corrosion cracking of Al-Mg alloys, Corrosion 73 (2017) 713–723. https://doi.org/10.5006/2343.

[8] P.J. Steiner, Z.D. Harris, J.T. Burns, Effect of Chloride Concentration on the Environment-Assisted Cracking Behavior of an Al-Mg Alloy in Atmospheric Environments, Corrosion 79 (2023) 1223–1233. https://doi.org/10.5006/4279.

[9] P.J. Steiner, J.T. Burns, Mechanistic studies of intergranular stress corrosion cracking in Al-Mg alloys under atmospheric exposure conditions, Corrosion 74 (2018) 1117–1131. https://doi.org/10.5006/2853.

[10] M. Pourbaix, Atlas of Electrochemical Equilibria in-Aqueous Solutions, n.d.

[11] M.E. McMahon, Z.D. Harris, J.R. Scully, J.T. Burns, The effect of electrode potential on stress corrosion cracking in highly sensitized Al–Mg alloys, Materials Science and Engineering: A 767 (2019). https://doi.org/10.1016/j.msea.2019.138399.

[12] Standard Practice for Operating Salt Spray (Fog) Apparatus 1, (n.d.). https://doi.org/10.1520/B0117-19.

[13] D. Scotto D'Antuono, J. Gaies, W. Golumbfskie, M.L. Taheri, Direct measurement of the effect of cold rolling on β phase precipitation kinetics in 5xxx series aluminum alloys, Acta Mater 123 (2017) 264–271. https://doi.org/10.1016/j.actamat.2016.10.060.

[14] R. Zhang, R.K. Gupta, C.H.J. Davies, A.M. Hodge, M. Tort, K. Xia, N. Birbilis, The influence of grain size and grain orientation on sensitization in AA5083, in: Corrosion, 2016. https://doi.org/10.5006/1703.

[15] J.G. Kaufman, Stress-Corrosion Cracking of Aluminum Alloys, in: Properties and Selection of Aluminum Alloys, ASM International, 2019: pp. 79–95. https://doi.org/10.31399/asm.hb.v02b.a0006545.

[16] D. Scotto D'Antuono, J. Gaies, W. Golumbfskie, M.L. Taheri, Grain boundary misorientation dependence of β phase precipitation in an Al-Mg alloy, Scr Mater 76 (2014) 81–84. https://doi.org/10.1016/j.scriptamat.2014.01.003.

[17] Y. Zhao, M.N. Polyakov, M. Mecklenburg, M.E. Kassner, A.M. Hodge, The role of grain boundary plane orientation in the β phase precipitation of an Al-Mg alloy, Scr Mater 89 (2014) 49–52. https://doi.org/10.1016/j.scriptamat.2014.07.003.

[18] X. Sauvage, N. Enikeev, R. Valiev, Y. Nasedkina, M. Murashkin, Atomic-scale analysis of the segregation and precipitation mechanisms in a severely deformed Al-Mg alloy, Acta Mater 72 (2014) 125–136. https://doi.org/10.1016/j.actamat.2014.03.033.

[19] F. Qin, C. Yang, H. Qi, C. Liu, H. Qi, Grain Size, Precipitation Behavior, and Mechanical Properties through the Thickness of Al-Mg-Si Aluminum Alloy Rings Produced by Compact Cast-Rolling Compound Forming, J Mater Eng Perform 31 (2022) 2329–2340. https://doi.org/10.1007/s11665-021-06326-7.

[20] D.L. Foley, A.C. Leff, A.C. Lang, M.L. Taheri, Evolution of β-phase precipitates in an aluminum-magnesium alloy at the nanoscale, Acta Mater 185 (2020) 279–286. https://doi.org/10.1016/j.actamat.2019.10.024.

[21] M. Lyn, C. Lim, Intergranular Corrosion Propagation in Sensitized Al-Mg Alloys, 2016.

[22] J.H. Ai, M.L.C. Lim, J.R. Scully, Effective hydrogen diffusion in aluminum alloy 5083-H131 as a function of orientation and degree of sensitization, Corrosion 69 (2013) 1225–1239. https://doi.org/10.5006/0987.

[23] J. Desai Choundraj, J. Kacher, Influence of misorientation angle and local dislocation density on β-phase distribution in Al 5xxx alloys, Sci Rep 12 (2022). https://doi.org/10.1038/s41598-022-05948-8.

[24] Designation: E112 − 13 Standard Test Methods for Determining Average Grain Size 1, (n.d.). https://doi.org/10.1520/E0112-13R21.

[25] Standard Test Method for Linear-Elastic Plane-Strain Fracture Toughness of Metallic Materials 1, (n.d.). https://doi.org/10.1520/E0399-22.

[26] R.P. Gangloff, D.C. Slavik, R.S. Piascik, R.H. Van Stone, Direct Current Electrical Potential Measurement of the Growth of Small Cracks, American Society for Testing and Materials (1992) 116–168.

[27] Standard Test Method for Measurement of Fatigue Crack Growth Rates 1, (n.d.). https://doi.org/10.1520/E0647-23A.

[28] Z.D. Harris, J.T. Burns, On the loading rate dependence of environment-assisted cracking in sensitized AA5456-H116 exposed to marine environments, Corros Sci 201 (2022). https://doi.org/10.1016/j.corsci.2022.110267.

[29] R.P. Gangloff, H.M. Ha, J.T. Burns, J.R. Scully, Measurement and modeling of hydrogen environment-assisted cracking in monel K-500, Metall Mater Trans A Phys Metall Mater Sci 45 (2014) 3814–3834. https://doi.org/10.1007/s11661-014-2324-z.

[30] J.X. Zhang, M. Ma, W.C. Liu, Effect of initial grain size on the recrystallization and recrystallization texture of cold-rolled AA 5182 aluminum alloy, Materials Science and Engineering: A 690 (2017) 233–243. https://doi.org/10.1016/j.msea.2017.03.015.

[31] P. Ebenberger, P.J. Uggowitzer, B. Gerold, S. Pogatscher, Effect of compositional and processing variations in new 5182-type AlMgMn alloys on mechanical properties and deformation surface quality, Materials 12 (2019). https://doi.org/10.3390/ma12101645.

[32] W. Gao, D. Wang, M. Seifi, J.J. Lewandowski, Anisotropy of corrosion and environmental cracking in AA5083-H128 Al-Mg alloy, Materials Science and Engineering: A 730 (2018) 367–379. https://doi.org/10.1016/j.msea.2018.06.021.

[33] J.L. Searles, P.I. Gouma, R.G. Buchheit, Stress Corrosion Cracking of Sensitized AA5083 (Al-4.5Mg-1.0Mn), n.d.

[34] A.J. Davenport, Y. Yuan, R. Ambat, B.J. Connolly, M. Strangwood, A. Afseth, G.M. Scamans, Intergranular Corrosion and Stress Corrosion Cracking of Sensitised AA5182, Materials Science Forum 519–521 (2006) 641–646. https://doi.org/10.4028/www.scientific.net/msf.519-521.641.

[35] C.: Yuan, Yudie, Localised corrosion and stress cracking of aluminium-magnesium alloys, University of Birmingham, 2005.

[36] R. Zhang, S.P. Knight, R.L. Holtz, R. Goswami, C.H.J. Davies, N. Birbilis, A survey of sensitization in 5xxx series aluminum alloys, in: Corrosion, National Assoc. of Corrosion Engineers International, 2016: pp. 144–159. https://doi.org/10.5006/1787.

[37] C.B. Crane, R.P. Gangloff, Stress corrosion cracking of Al-Mg alloy 5083 sensitized at low temperature, in: Corrosion, National Assoc. of Corrosion Engineers International, 2016: pp. 221–241. https://doi.org/10.5006/1766.

[38] M.E. McMahon, P.J. Steiner, A.B. Lass, J.T. Burns, The effect of temper and composition on the stress corrosion cracking of Al-Mg alloys, Corrosion 73 (2017) 347–361. https://doi.org/10.5006/2317.

[39] Z.D. Harris, J.T. Burns, On the loading rate dependence of environment-assisted cracking in sensitized AA5456-H116 exposed to marine environments, Corros Sci 201 (2022). https://doi.org/10.1016/j.corsci.2022.110267.

[40] M.E. McMahon, J.R. Scully, J.T. Burns, Mitigation of Intergranular Cracking in Al-Mg Alloys via Zn-Based Electrode Potential Control in Sodium Chloride Solution, Corrosion 75 (2019) 911–928. https://doi.org/10.5006/3185.

[41] R. Sanders, J. Staley, A History of Wrought Aluminum Alloys and Applications, in: Properties and Selection of Aluminum Alloys, ASM International, 2019: pp. 157–201. https://doi.org/10.31399/asm.hb.v02b.a0006516.

[42] N. Brown, P. Kramer, F. Friedersdorf, M. Schindelholz, J. Siegel, Environmentally assisted cracking measurements in structural aluminum alloys under accelerated test conditions, Corrosion 72 (2016) 1351–1362. https://doi.org/10.5006/2085.

[43] C. Liu, J. Srinivasan, R.G. Kelly, Editors' Choice—Electrolyte Film Thickness Effects on the Cathodic Current Availability in a Galvanic Couple, J Electrochem Soc 164 (2017) C845–C855. https://doi.org/10.1149/2.1641713jes.

[44] F. Ge, L. Zhang, H. Tian, M. Yu, J. Liang, X. Wang, Stress Corrosion Cracking Behavior of 2024 and 7075 High-Strength Aluminum Alloys in a Simulated Marine Atmosphere Contaminated with SO2, J Mater Eng Perform 29 (2020) 410–422. https://doi.org/10.1007/s11665-019-04537-7.

[45] M. WANG, L. WANG, K. PANG, Y. LIU, Y. WANG, Z. CUI, Understanding stress corrosion cracking behavior of 7085-T7651 aluminum alloy in polluted atmosphere, Chinese Journal of Aeronautics 36 (2023) 408–421. https://doi.org/10.1016/j.cja.2023.06.011.

[46] E.M. Arnold, J.J. Schubbe, P.J. Moran, R.A. Bayles, Comparison of SCC thresholds and environmentally assisted cracking in 7050-T7451 aluminum plate, J Mater Eng Perform 21 (2012) 2480–2486. https://doi.org/10.1007/s11665-012-0204-5.

[47] PENAIR ® M5571, n.d.

[48] G.A. Truesdale, A.L. Downing, Solubility of Oxygen in Water, Nature 173 (1954) 1236.

[49] I.W. Huang, B.L. Hurley, F. Yang, R.G. Buchheit, Dependence on Temperature, pH, and Cl- in the Uniform Corrosion of Aluminum Alloys 2024-T3, 6061-T6, and 7075-T6, Electrochim Acta 199 (2016) 242–253. https://doi.org/10.1016/j.electacta.2016.03.125.

[50] C.N. Panagopoulos, E. Georgiou, K.I. Giannakopoulos, P.G. Orfanos, Effect of ph on stress corrosion cracking of 6082 al alloy, Metals (Basel) 8 (2018). https://doi.org/10.3390/met8080578.

[51] W.-T. Tsai, J.-B. Duh, J.-J. Yeh, J.-T. Lee, Y.-C. Chang"', Effect of pH on Stress Corrosion Cracking of 7050-T7451 Aluminum Alloy in 3.5 wt% NaCl Solution *, 1990. http://meridian.allenpress.com/corrosion/article-pdf/46/6/444/1530787/1_3585130.pdf.

[52] Z. Dan, I. Muto, N. Hara, Effects of environmental factors on atmospheric corrosion of aluminium and its alloys under constant dew point conditions, Corros Sci 57 (2012) 22–29. https://doi.org/10.1016/j.corsci.2011.12.038.

[53] T.F. Cui, D.X. Liu, P.A. Shi, J.J. Liu, Y.H. Yi, H.L. Zhou, Effect of NaCl concentration, pH value and tensile stress on the galvanic corrosion behavior of 5050 aluminum alloy, Materials and Corrosion 67 (2016) 72–83. https://doi.org/10.1002/maco.201408189.

[54] E. Bumiller, INTERGRANULAR CORROSION IN AA5XXX ALUMINUM ALLOYS WITH DISCONTINUOUS PRECIPITATION AT THE GRAIN BOUNDARIES A Dissertation Presented to, 2011.

[55] J.A. Lyndon, R.K. Gupta, M.A. Gibson, N. Birbilis, Electrochemical behaviour of the β-phase intermetallic (Mg2Al3) as a function of pH as relevant to corrosion of aluminium-magnesium alloys, Corros Sci 70 (2013) 290–293. https://doi.org/10.1016/j.corsci.2012.12.022.

[56] B. Zaid, D. Saidi, A. Benzaid, S. Hadji, Effects of pH and chloride concentration on pitting corrosion of AA6061 aluminum alloy, Corros Sci 50 (2008) 1841–1847. https://doi.org/10.1016/j.corsci.2008.03.006.

[57] C.B. Crane, R.G. Kelly, R.P. Gangloff, Crack chemistry control of intergranular stress corrosion cracking in sensitized Al-Mg, in: Corrosion, National Assoc. of Corrosion Engineers International, 2016: pp. 242–263. https://doi.org/10.5006/1852.

Chapter 2 : The effect of sensitization and loading orientation on the environment assisted crack (EAC) growth kinetics of Alloy 1 in 0.6 M NaCl

2.1 Introduction

The 5xxx series aluminum alloys (AA) have been used in a wide variety of applications due to their good corrosion resistance, high strength to weight ratio, and good weldability. The strength of these alloys comes from the supersaturation of Mg (typically above 3 wt%) in the Al matrix. However, when exposed to elevated temperatures (ranging from 50 -300°C), Mg can diffuse to grain boundaries and precipitate the stable β phase (Al_3Mg_2) [13,14]. This process is known as sensitization. Unfortunately, the sensitization phenomenon is deleterious to AA5xxx corrosion resistance, because the beta phase is more electrochemically active than the surrounding Al matrix causing preferential dissolution of the beta phase. Moreover, since the precipitation occurs primarily on the grain boundaries, these alloys become susceptible to intergranular corrosion (IGC) and intergranular stress corrosion cracking (IGSCC) in chloride containing environments [15].

The microstructure of these alloys depends heavily on the processing methods. As a result of different processing techniques, a wide variety of grain structures have been observed for this alloy system. Similarly, the beta phase precipitation also depends on the specific processing procedure performed. The complexity of beta phase precipitation is something that has had much attention in scientific literature [13,14,16–19]. It has been shown that the time [13] and temperature [20] of exposure can greatly affect the size of the beta precipitate. Others have shown the importance of high and low angle grain boundaries on the influence of beta precipitation [16,21–23]. Along with *inter*granular beta, *intra*granular beta precipitation also occurs, often because of reduced activation energies for precipitation at dislocations in the grains [14].

Engineers who are assessing the structural integrity of AA5xxx components have consistently relied on the ASTM G67 NAMLT (Nitric Acid Mass Lost Test) [2] to quantify the amount of sensitization (often called the degree of sensitization), which can be related to a measure of IGC and IGSCC susceptibility. The test involves exposure of the specific alloy to a concentrated nitric acid bath for 24 hours. The nitric acid selectively attacks the beta phase, but the α-Al matrix can also be removed, adding to the total mass loss and increasing the NAMLT value (in mg/cm^2). Despite this shortcoming, the test is still widely used because of its simplicity and cost effectiveness. One alternative, proposed by McMahon *et al*. [3], sought to provide another metric capable of assessing IGC and IGSCC susceptibility using a linear grain boundary tracing technique in which the percent of grain boundary area covered by intergranular beta was determined. While the authors do point out some limitations of the method, it was shown to

exhibit a better correlation with IGSCC susceptibility compared to NAMLT. Knowing the amount of beta phase on the grain boundaries is an important step in determining IGSCC susceptibility. The more intergranular beta phase, the greater the susceptibility.

Since the grain boundaries constitute the crack path, it is also important to consider the grain size and directionality (i.e. elongated or equiaxed) when evaluating susceptibility. A study by McMahon *et al*. explored the impact of loading orientation relative to the grain structure for AA5083-H131 and -H116 (and 5456-H116) with elongated grain structures, which were cut from thick plates [7]. When the loading direction of AA5083-H131 (NAMLT 40) was perpendicular to the elongated grains, and crack growth was parallel to the elongated grains (known as the SL orientation), the Stage II da/dt was approximately 2 $x10^{-3}$ mm/s, which was reached at a stress intensity of 6 MPa√m. On the other hand, when the loading orientation was parallel with the elongated grains and crack growth was perpendicular to the elongated grains (known as the TL orientation), the threshold stress intensity K_{TH} was approximately 30 MPa√m, a huge increase in IGSCC resistance, simply by changing the loading orientation. This study also showed that for each alloy type and heat treatment, increased sensitization exacerbated loading orientation effects.

In this chapter, the objective of gaining baseline material microstructure characteristics (grain size and amount of beta phase on the grain boundaries) was performed. The initial grain microstructure is imperative to understand as these features of the alloy will affect the environmentally assisted cracking (EAC) behavior. The effect of sensitization must also be understood because of its deleterious effect on corrosion resistance. These results are used to inform linear elastic fracture mechanics (LEFM) testing results to understand the effect of loading orientation and sensitization of Alloy 1 on the EAC kinetics.

2.2 Experimental Procedures

2.2.1 Material

The material under investigation throughout the entirety of the Thesis work is an aluminum alloy (AA) with a high Mg content (5.5-6 wt% Mg), and is named Alloy 1. The remainder of the composition is considered proprietary knowledge, and will not be discussed in the following work. This material was supplied by an external source, the condition in which the material was received will be referred to as the "as received" condition. In addition to the as received condition, specific samples were sensitized in a laboratory oven at 100°C for 1, 7, or 14 days, known as the sensitized condition.

The metallographic specimen used for this chapter were cut from a 3.5 mm sheet in the TL, LS, and ST planes where L is the longitudinal or parallel to the rolling direction, T is the transverse or normal to the rolling direction, and S is the short transverse direction or direction along plate thickness. Samples

were prepared for characterization at Acuren Inspection Inc. (formerly Anamet Inc.), where they were polished to 0.05 micron mirror finish using a colloidal silica slurry.

2.2.2 Grain Size Determination

Electron back scatter detection (EBSD) imaging of the TL, LS, and ST planes were obtained on a Helios UC G4 Dual Beam FIB-SEM (reference the NMFC). In addition, the LS plane was imaged at the sample edge, 0.25, 0.33, and 0.5 through the thickness of the sample plane to gather information about the through thickness grain microstructure. A schematic detailing where the EBSD images were taken on the sample through the thickness is illustrated in Figure 2.1. Images were taken with a step size of 0.88 microns and a resolution of 512.

The procedure for grain size determination was adopted from ASTM E112 [24] and involved EBSD image analysis using MTEX, a free MATLAB toolbox. To start, a line with a defined length was overlaid onto the EBSD image and the MTEX grain boundary intersection function was utilized to give the number of grain boundary intersections with the drawn line. This number was divided by the total line length, and gave the average grain diameter. The grain boundary – line intersection procedure was repeated five times for each image in each direction (L, T, or S), and the reported grain size is an average of these five repetitions.

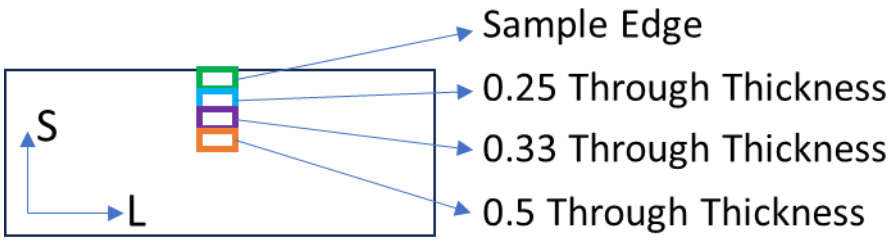

Figure 2.1: Schematic illustration of how EBSD images were taken through the thickness of the LS plane. The S direction runs vertical, and the L direction runs horizontal. There were four through thickness locations of interest, the sample edge, 0.25 through the thickness, 0.33 through the thickness, and 0.5 (mid) through the thickness.

2.2.3 Grain Boundary Beta Coverage Analysis

It has been shown that the extent of beta phase on the grain boundaries using a chemical etch in 10% ammonium persulfate adjusted to pH 1.2 with sulfuric acid, rather than the traditional NAMLT test can be a better proxy at estimating intergranular attack [3]. Therefore, the method of measuring the amount of beta phase precipitated on the grain boundaries was followed according to McMahon *et al* [3]. Forward scatter detected (FSD) and EBSD images were taken on a Helios UC G4 Dual Beam FIB-SEM, using

the same working conditions as stated above. EBSD grain maps were opened in ImageJ (an open source software) and binarized. The binarized EBSD grain map was then overlaid onto a FSD image, outlining total grain boundary area and discreet beta phase precipitation on the grain boundaries. These steps are outlined in Figure 2.2. Individual pixels of grain boundary beta are counted and divided by the total pixel count of grain boundary area, and multiplied by 100 to give a total percentage of beta phase on the grain boundaries.

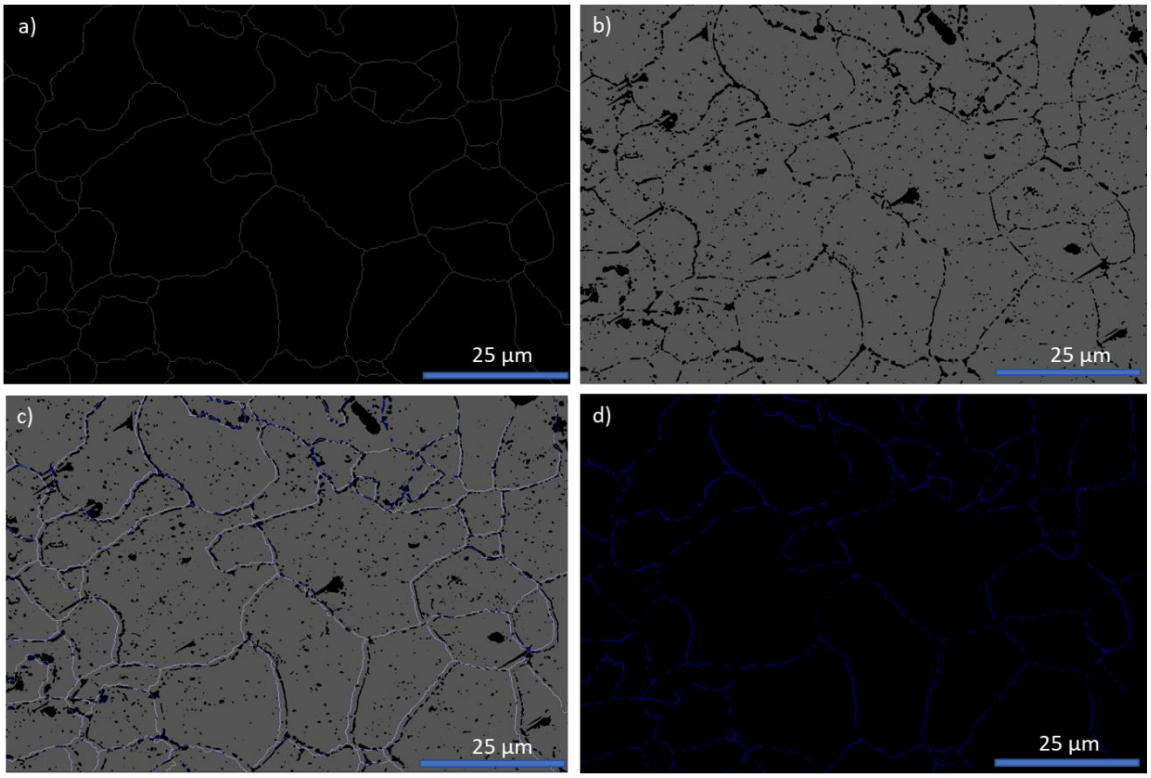

Figure 2.2**:** Linear grain boundary beta coverage procedure first starts with EBSD image. Using ImageJ, the EBSD image can be binarized (a), and the FSD image with beta phase etching (b) can be merged to show the total grain boundary area and regions of grain boundaries that are covered with beta (c). These areas can be traced and extracted (d) to show the amount of grain boundary covered by beta phase. The calculation of linear grain boundary beta coverage takes the number of colored pixels in d) divided by the number of colored pixels in a).

2.2.4 Sample Design for Mechanical Testing

Alloy 1 in the as received condition was machined into single edge notch tensile (SENT) specimens from the 3.5 mm sheet. Most of the experiments were oriented such that the tensile loading was parallel to the T direction (transverse, normal to rolling direction), and the Mode 1 cracking plane was along in the L direction (rolling direction), shortened as the T-L orientation. Some samples were also machined in the L-T orientation for the purpose of comparing the SCC susceptibility to the T-L oriented samples. To

illustrate the difference in loading orientation with respect to Alloy 1 sheet orientations, a figure adapted from ASTM E399-22 [25] is given in Figure 2.3. Note that because the as received material came from a thin sheet, samples could not be machined in the S-L orientation, so testing in this orientation is not possible and irrelevant. The average thickness of the specimen was 3.33 mm; the specimen width was 25.4 mm and had a total length of 177.8 mm. An electrical discharge machined (EDM) notch was placed at the center of specimen length, with a depth equaling 5.7 mm.

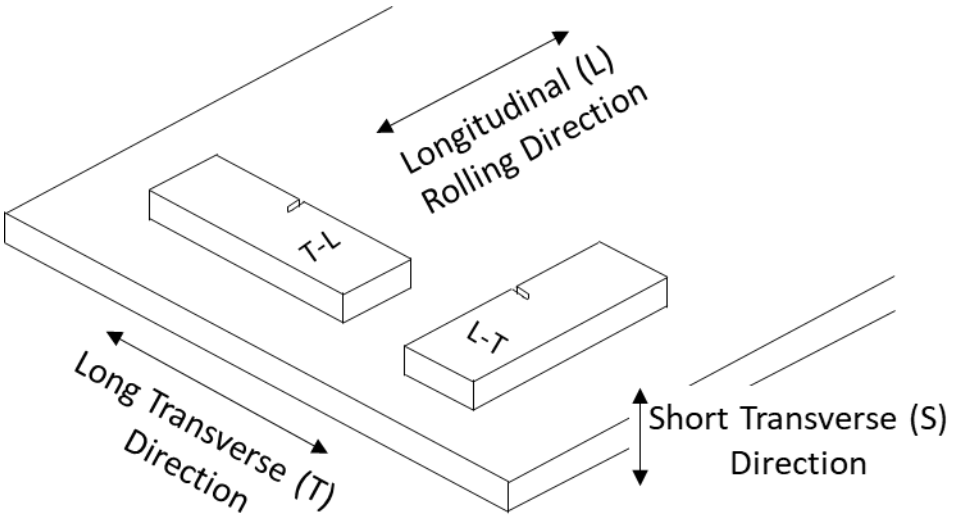

Figure 2.3**:** Single edge notch tension (SENT) specimen machined from sheet of Alloy 1 in the T-L and L-T loading orientation, adapted from ASTM E399-22 [25].

2.2.5 Linear Elastic Fracture Mechanics (LEFM) Testing

Stress corrosion susceptibility of Alloy 1 was probed using LEFM approach. The SENT specimen were fatigue precracked in lab air to 6.0 mm with a final stress intensity (K) of 4 MPa√m. Slow rising displacement experiments following the precrack were controlled via K and conducted at a rate of 1 MPa√m/hr. Direct current potential difference (dcPD) was used to monitor crack growth, and Johnson's equation was used to convert potential values to crack length. This system has a resolution limit of 0.5 um. The details of this method can be read elsewhere [26].

<u>The Effect of Sensitization</u>

Laboratory sensitization of SENT specimen was completed at 100°C for 7 or 14 days. Specimen were loaded in the T-L orientation, and fatigue pre-cracked following the procedure outlined earlier. An acrylic cell was placed around the sample and filled with 200 mL of 0.6 M NaCl solution before the K rise experiment. During the experiments, solution was flowed continuously from a 2 L reservoir at 100

mL/min. Details of the K rise experiment are also described earlier. An applied potential of -800 mV_{SCE} was held consistently during the experiments using a Biologic PG-581 handheld potentiostat. A copper wire welded to the SENT Alloy 1 specimen was the working electrode; saturated calomel electrode (SCE) reference electrode and Pt mesh as the counter electrode were used.

The Effect of Loading Orientation

SENT specimens of Alloy 1 were machined in the TL and LT orientations, with the same dimensions described in Figure 1. The fatigue precrack and K rise experimental procedures were detailed earlier. The environmental conditions for these experiments utilized an acrylic cell placed around the specimen, allowing for 200 mL of 0.6 M NaCl (pH 6.0) solution to flow continuously for the duration of the experiments at a rate of 100 mL/min. Potentiostatic control was ensured using a Biologic PG-581 handheld potentiostat, with an insulated copper wire welded to the Alloy 1 SENT specimen as the working electrode, a SCE as the reference electrode, and Pt wire welded to Pt mesh as the counter electrode. After the K rise experiments were completed, the samples were post-test fatigued until failure.

Fracture surface images were gathered on a FEG-Quanta 650 SEM using an Everhart Thornley detector (ETD) using secondary electron imaging mode. A spot size of 3.0 and an accelerating voltage of 10.0 kV were the parameters used for imaging.

Data Analysis of LEFM Results

Crack growth rates were calculated using the crack length values captured via dcPD and following the seven point incremental polynomial method akin to what is described for fatigue crack growth rates in ASTM E647 Appendix XI [27]. The dcPD method is sensitive to changes in the plastic zone size during loading for LEFM experiments. To account for these changes, one experiment was conducted in an inert environment – where Alloy 1 was exposed to dry N_2 and loaded in the same conditions as mentioned above and changes in crack length due to plasticity were recorded. After the experiment, the fracture surface was evaluated to ensure no SCC growth had occurred during exposure to the inert environment. After this verification, it was determined that any changes in dcPD recorded crack length during this experiment was purely due to plastic zone size extension. Crack growth rate versus stress intensity was plotted with an exponential fit. The equation of the fit is given as:

$$\frac{da}{dt} = 6.37 * 10^{-8} e^{0.194K}$$

This exponential fit will be used for the entirety of the Thesis work and is known as the resolution limit because it is the resolution limit for Alloy 1 plasticity related extension captured via dcPD. To accurately display and compare crack growth rates of Alloy 1 exposed to corrosive environments, and

therefore exhibiting IGSCC related crack growth, this resolution limit found for every experimental output, finding the resolution limit da/dt as a function of the applied stress intensity. These values were then subtracted from each calculated da/dt using the seven point polynomial method, and the resulting da/dt vs. K curves presented reflect only crack growth associated with IGSCC. Previous work has detailed these procedures and justified the so-called resolution limit correction [28].

Another issue in gathering da/dt from the dcPD method is when the crack surfaces come into electrical contact, indicating a decrease in crack growth. Since it is not possible for the crack length to physically decrease, the data is corrected in these occurrences by fitting a linear function to the log K vs log da/dt in the region where the da/dt was decreasing. This linear function was subtracted from the measured da/dt using raw dcPD measurements. Since each data set has different da/dt vs. K relationships, no singular equation was used. This procedure was outlined by Gangloff *et al.* and more details on the effect of the so-called "shorting" correction can be read elsewhere [29].

2.3 Results

2.3.1 Grain Size of As Received Alloy 1

An example of the TL microstructure from EBSD imaging is shown in Figure 2.4 (a). From visual inspection, it is evident that no obvious texture developed in this metallographic plane, and that the grain shape is mostly equiaxed in this orientation – meaning there are no elongated grains in a specific direction. The results of the grain size determination for the T direction, and the L direction are listed in Table 2.1. The average grain diameter in the L direction was 18.71 microns and 16.38 microns in the T direction. Additionally, the grain directionality ratio (L/T) was 1.14, which confirms the visual inspection that the grains are mostly equiaxed in the TL plane, since the grain directionality ratio is close to one.

The mid-thickness microstructure of the LS plane can be viewed in Figure 2.4 (b). There is no obvious texture observed, but there is evidence of grain directionality, meaning the grains are elongated in the L direction compared to the S direction. These "pancake" grains are likely a result of the sheet forming process and are typically observed for other AA5xxx series systems [7]. The average grain size of the L direction at the mid-thickness of the LS plane is 17.84 microns and 7.20 microns in the S direction using the line intersection method, given in Table 2.1. The average grain directionality ratio for the LS plane (L/S) is thus 2.48, meaning the grains are elongated in the L direction, which confirms the visual expectation in Figure 2.4 (b).

An example of the microstructure in the ST plane is visible in Figure 2.4 (c). The ST microstructure appears to be similar to the SL plane, 0.25 through the thickness, with a slight elongation in the T direction.

Grain size calculations in the S and T directions yield average grain diameters of 6.22 microns and 13.05 microns, respectively. Table 2.1 also shows the grain directionality ratio (T/S) of 2.05, verifying the initial observations in Figure 2.4 (c).

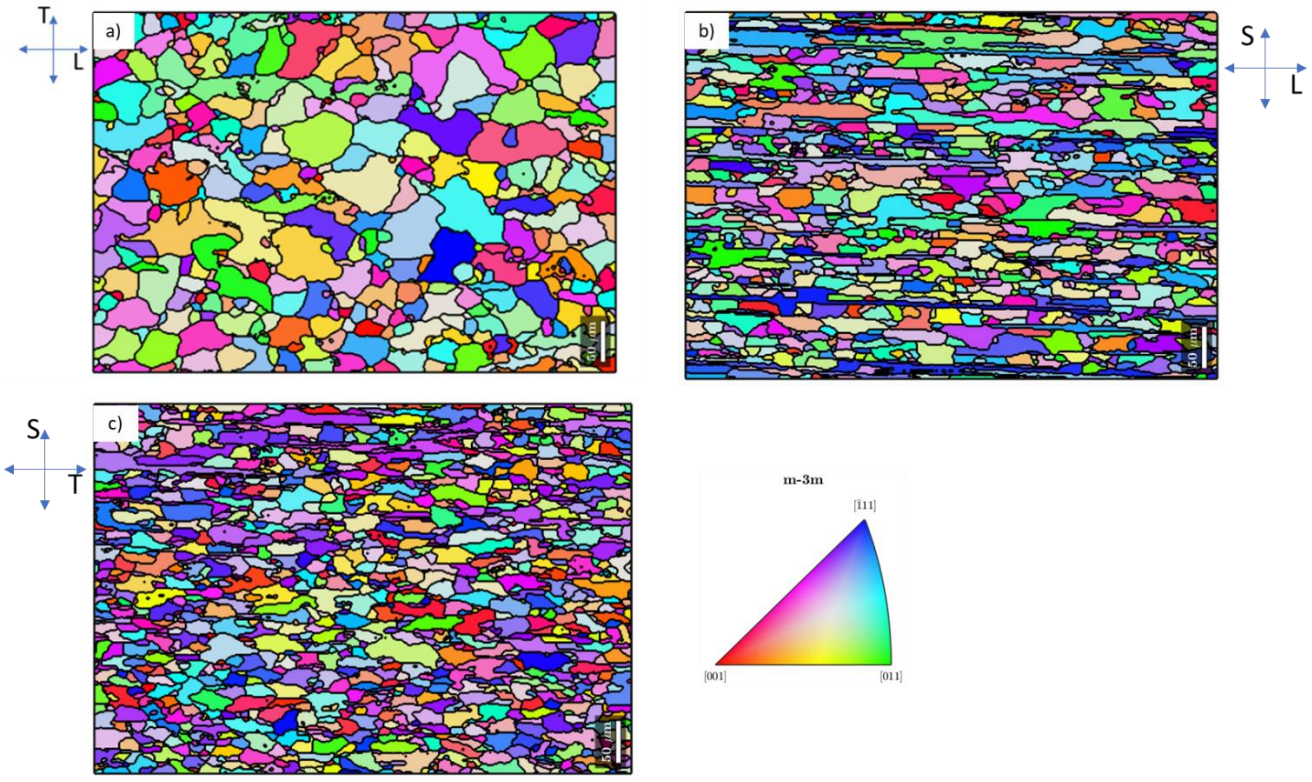

Figure 2.4: Inverse pole figure (IPF) maps via EBSD of Alloy 1 in the as received condition in the a) TL plane, b) LS plane, and c) ST plane. The longitudinal (L) direction is running horizontal in a) and b), with the long transverse (T) direction running vertical and the short transverse (S) direction running vertical in a) and b), respectively. The T direction is running horizontal and the S direction is running vertical in c). Inverse pole figure color key is given in the image on the lower right.

Table 2.1*:* Average grain diameter (in microns) in the TL, LS, and ST planes of the as received condition of Alloy 1: adopted from ASTM E112 [24] using MTEX, open source MATLAB toolbox. The grain directionality ratio shows the ratio of average grain diameter of L/T, L/S, and T/S.

	Average Grain Diameter (μm)			Grain Directionality Ratio
	L Direction	T Direction	S Direction	
TL Plane	18.71	16.38		1.14
LS Plane	17.84		7.2	2.48
ST Plane		13.05	6.22	2.10

The LS plane was imaged at several different locations throughout the thickness of the specimen to address the concern for variability in the though thickness microstructure, which is typical for AA5xxx that have been rolled. Figure 2.5 compares an example of the grain microstructure at the sample edge, 0.25 through thickness, 0.33 through thickness, and 0.5 through thickness. From each of the images, no obvious texture is observed, but there does appear to be some grain directionality, meaning there is a slight elongation of the grains in the L direction. Table 2.2 shows the average grain diameters in the S and L directions for each step through the thickness (sample edge, 0.25, 0.33, and 0.5). At every distance through the thickness (edge, 0.25, 0.33, and 0.5) of the sample, the grains were larger in the L direction than in the S direction. This indicates some level of grain directionality, as was witnessed in the EBSD images in Figure 2.4 (b). The average grain diameter in the S and L directions continually increased with increasing distance from the sample edge, with the one exception being the average grain diameter in the L direction at the 0.33 thickness was less than the grain diameter at the 0.25 thickness. These two average diameters were within 6% of one another, so there is reason to argue the grain diameter did not significantly change from 0.25 to 0.33 through the thickness in the L direction. Overall, the average grain diameter in the L direction was approximately 2-2.5 times larger than in the S direction, as shown as the grain directionality ratio in Table 2.2. The grain directionality ratio again confirms visual results of some grain elongation in the L direction.

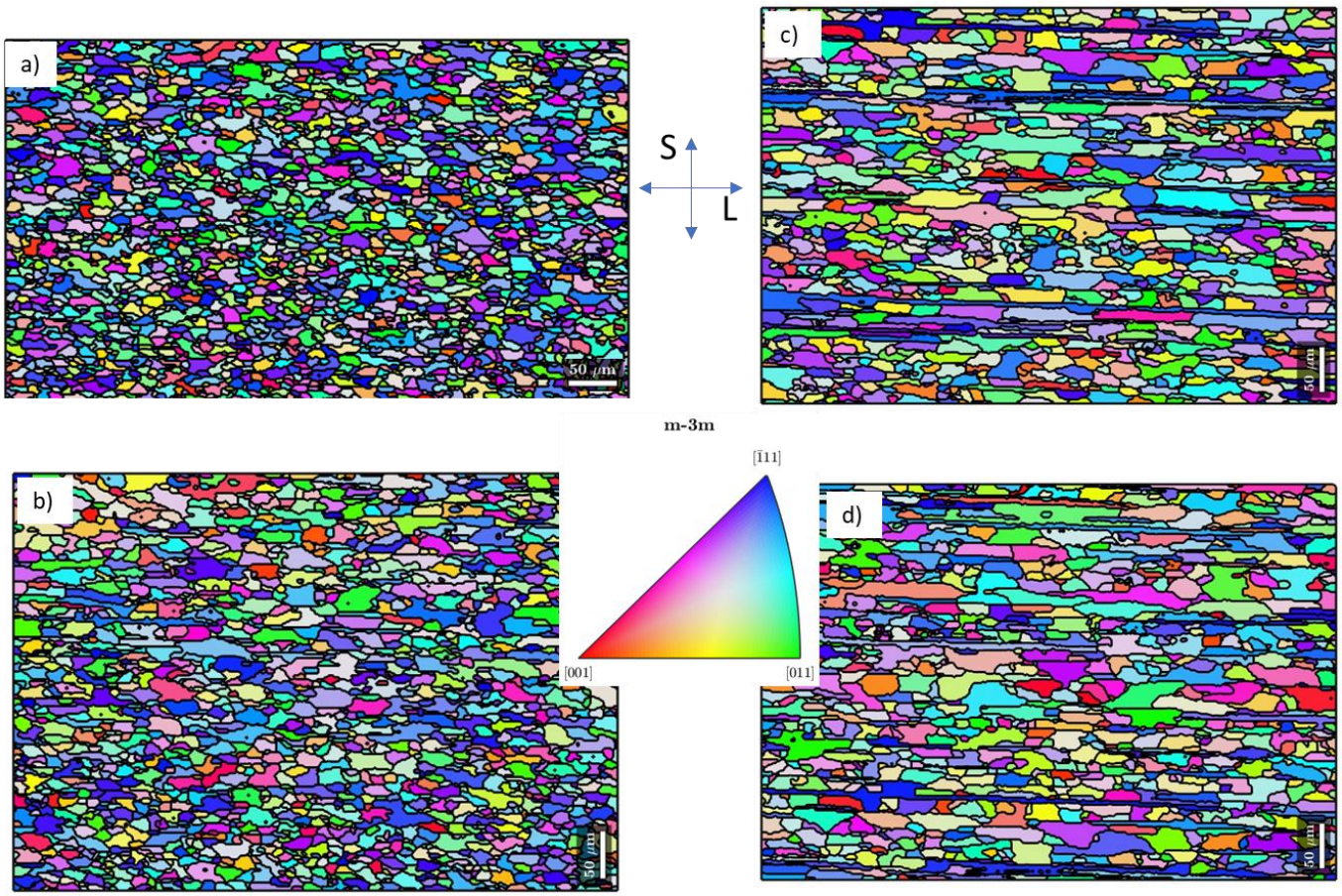

Figure 2.5: IPF maps of as received Alloy 1 in the SL plane at: a) sample edge, b) 0.25 through thickness, c) 0.33 through thickness, d) 0.5 through thickness. The L direction runs horizontal on each image (a-d), and the S direction runs vertical on each image (a-d). The IPF color map has been provided as the center image. Recall Figure 2.1 to understand where on the LS plane each of the images were taken.

Table 2.2: Average grain diameters and directionality ratios through the thickness of the as received Alloy 1 LS plane in the L and S directions.

LS Plane

Distance from Sample Edge	L Direction Average Grain Diameter (µm)	S Direction Average Grain Diameter (µm)	Directionality Ratio L/S
0	10.59	5.34	1.99
0.25	13.82	6.14	2.25
0.33	13.09	7.52	1.74
0.5	17.84	7.20	2.48

2.3.2 Grain Boundary Beta Coverage Analysis

The BSE images used for the 0 day and 14 day sensitization beta coverage analysis are shown in Figure 2.6 and Figure 2.7, respectively. These images reflect the microstructure of Alloy 1 after the ammonium persulfate etch. From the Figure *2.6*Figure *2.7*, it is clear that most of the grain boundaries had beta phase that had been etched as seen from the dark continuous lines outlining each grain. This indicates that even in the as received condition, Alloy 1 has a high amount of beta phase on the grain boundaries. In other words, it can be said that the "as received" condition had some level of sensitization before laboratory oven exposure. After completing the grain boundary beta phase coverage analysis, it was found that the as received (0 days sensitized) and the 14 day sensitized condition had almost equivalent amount of beta phase on the grain boundaries, average of approximately 83%, as shown in Figure *2.8*.

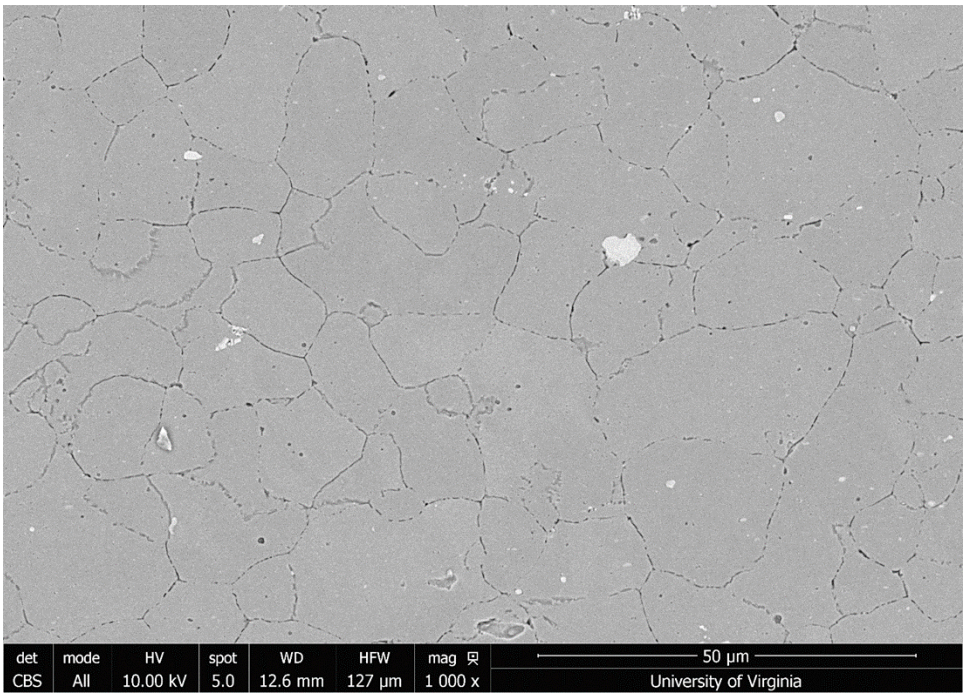

Figure 2.6: BSE image of 0 day sensitized (as received) Alloy 1 after ammonium persulfate etch. The dark lines on the grain boundaries indicate the beta phase which has been etched. Notice that the majority of the grain boundary is etched.

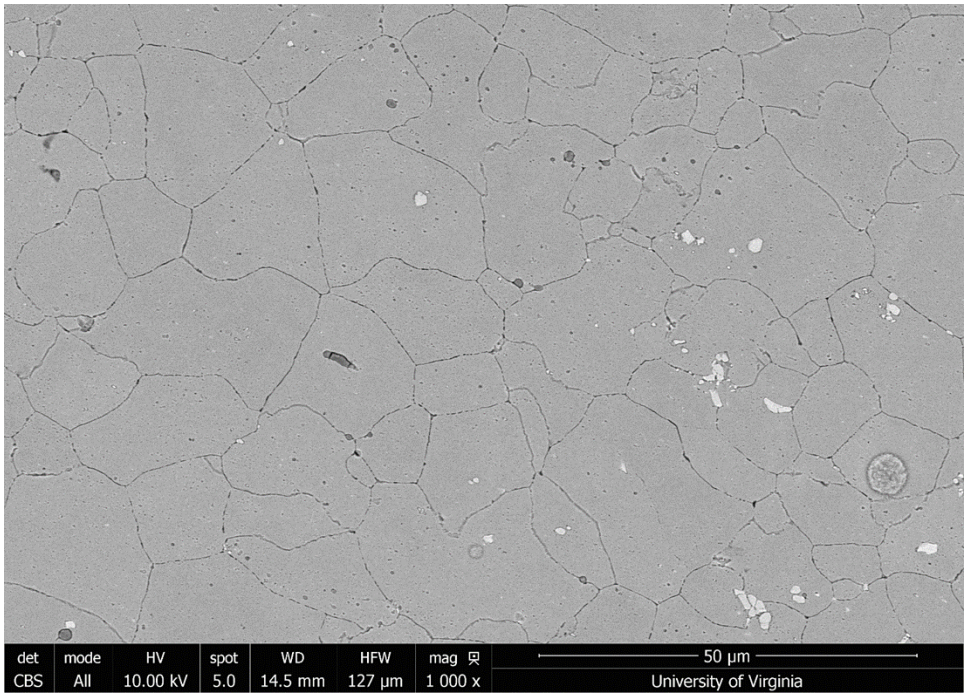

Figure 2.7: BSE image of 14 day sensitized Alloy 1 after ammonium persulfate etch. The dark lines on the grain boundaries indicate the beta phase which has been etched. Notice that the majority of the grain boundary is etched.

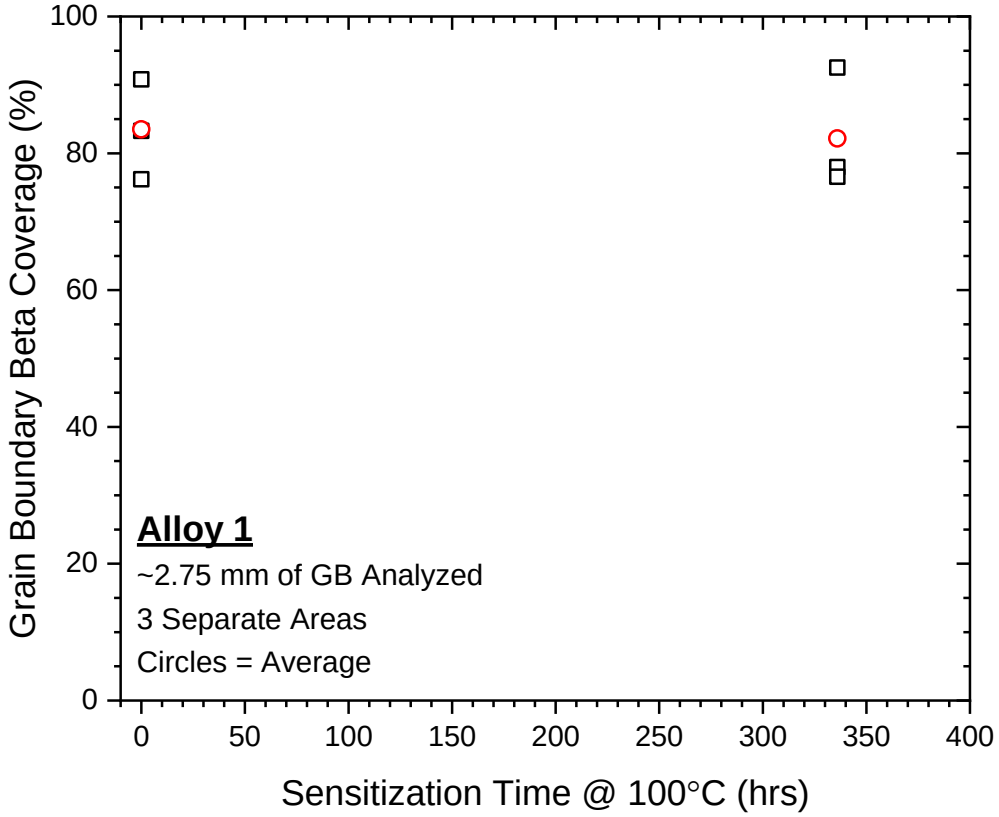

Figure 2.8: Grain boundary beta coverage as a function of sensitization time for Alloy 1. The black squares represent individual data points and the red circles are an average percent coverage for each sensitization time.

2.3.3 The Effect of Sensitization on EAC Kinetics

Crack growth kinetics from the slow rising displacement experiments are shown in Figure 2.9. The specimen with laboratory sensitization for 7 days had faster crack growth rates at stress intensities greater than 8 MPa√m as compared to the as received sample, while the specimen sensitized for 14 days had faster crack growth rates at all stress intensities tested compared to the as received. From stress intensities of 8-13 MPa√m, the sensitized specimen had equivalent crack growth kinetics. At the maximum stress intensities tested, the specimen sensitized for 14 days had crack growth rates an order of magnitude faster than the as received specimen, and the specimen sensitized for 7 days about 9x faster than the as received. The threshold stress intensity of the sample sensitized for 14 days was the lowest, followed by the as received specimen and lastly the sample sensitized for 7 days.

Figure 2.10 and Figure 2.11 show the fracture surfaces of the as received and specimen sensitized for 7 days, respectively. One noticeable feature is the IGC fracture morphology, highlighted in the inset of Figure 2.11, indicating that the samples fractured by an intergranular cracking mechanism. The fracture surfaces also show some level of crack front irregularity, meaning that the intergranular fracture occurred unevenly across the sample thickness. From the figures, it is noticeable that the edges of the sample thickness cracked faster than the middle of the sample. Although, this trend is less obvious in the as-received condition, compared to the sensitized samples (14 day sensitized sample also had this trend, but image not shown).

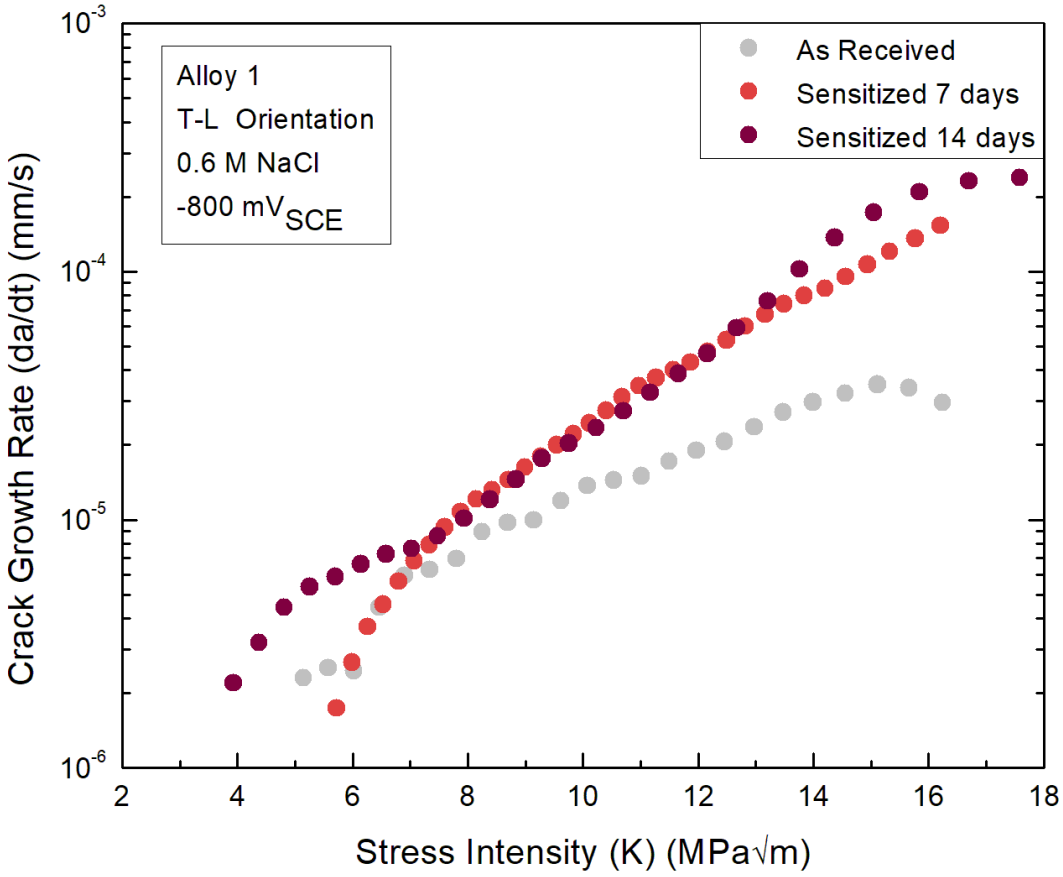

Figure 2.9: Crack growth rate versus stress intensity of Alloy 1 exposed to 0.6 M NaCl at a fixed applied potential of -800 mV_{SCE}, displaying the effect of sensitization on IGSCC susceptibility.

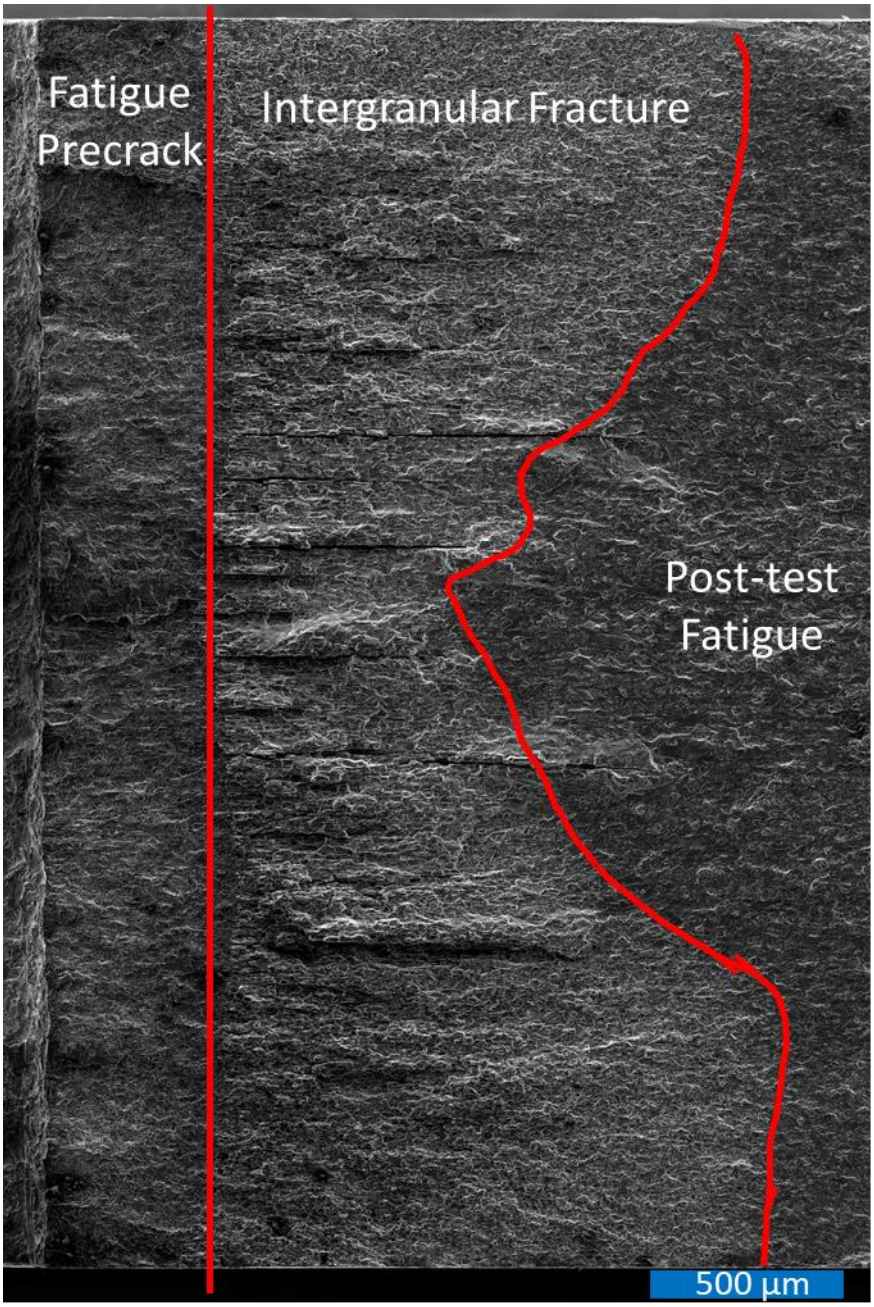

Figure 2.10: SEM fractography of the as received SENT specimen loaded in the T-L orientation after testing in 0.6 M NaCl and -800 mV_{SCE} applied potential. The straight red line indicates the end of the fatigue precracked region to the left of the line, and intergranular fracture region to the left. The second red line indicates the end of the intergranular fracture that occurred during the EAC experiment, and to the right of the line is the post-test fatigued region.

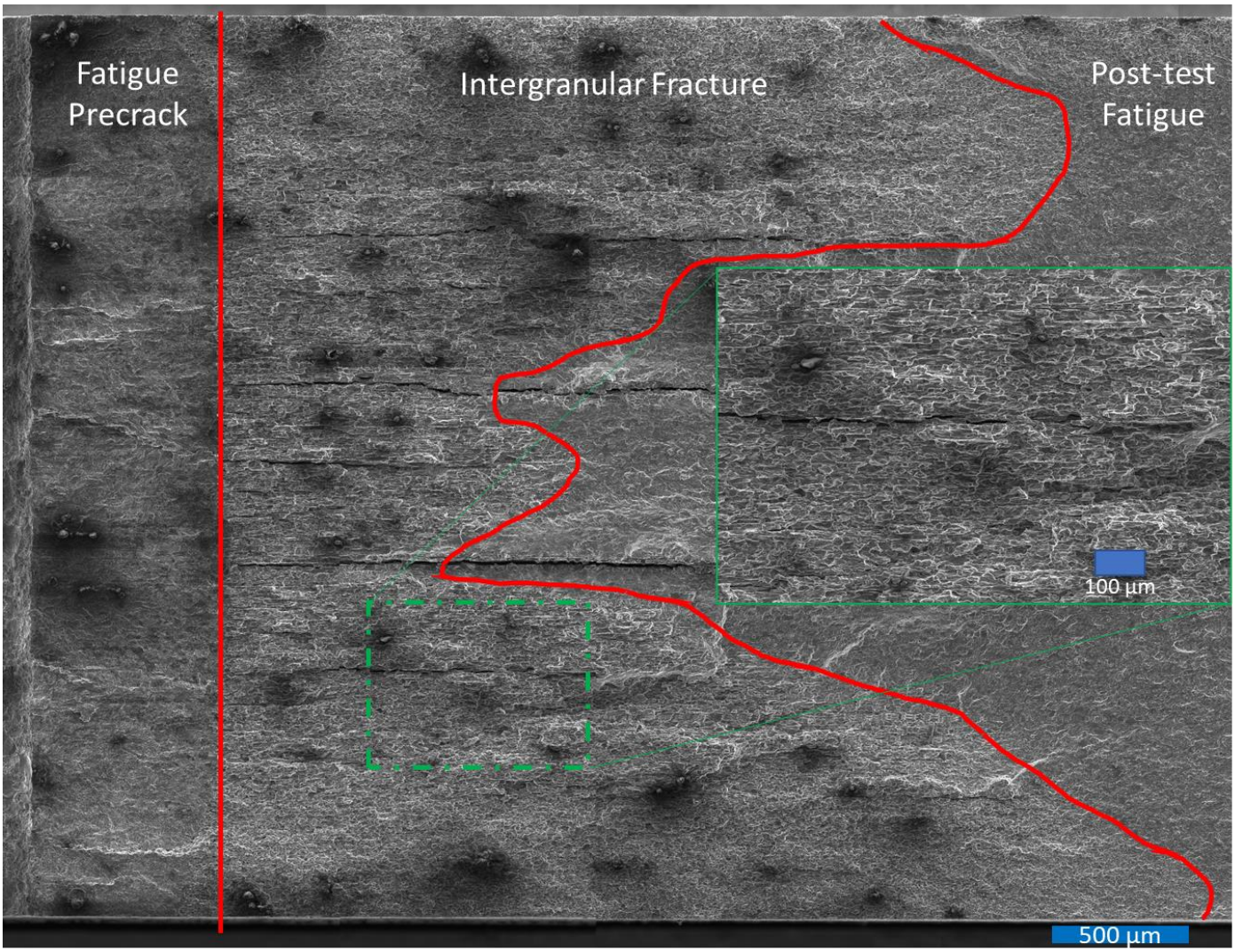

Figure 2.11: SEM fractography of the sensitized SENT specimen loaded in the T-L orientation for 7 days after testing in 0.6 M NaCl and -800 mV_{SCE} applied potential. The straight red line indicates the end of the fatigue precracked region to the left of the line, and intergranular fracture region to the left. The second red line indicates the end of the intergranular fracture that occurred during the EAC experiment, and to the right of the line is the post-test fatigued region. The inset image, outlined in green, reveals the typical intergranular fracture morphology.

2.3.4 The Effect of Loading Orientation on EAC Kinetics

The crack growth kinetics of Alloy 1 exposed to 0.6 M NaCl in the T-L and L-T orientation can be viewed in Figure 2.12. The results show similar crack growth rates for all applied K except near the threshold regime. Although the two orientations have nearly the same K_{TH}, the crack growth rate in the T-L orientation is higher than the L-T orientation until an applied stress intensity of 7 MPa√m. This is likely

within the typical scatter from testing, because after 7 MPa√m, the crack growth rates are similar with little variation. Therefore, it can be said there is no significant difference in the crack growth rates of Alloy 1 tested in the two relevant orientations.

The fracture surface of the sample loaded in the T-L orientation is provided in Figure 2.10, and the fracture surface of the sample loaded in the L-T orientation is provided in Figure 2.13. In both cases there is a modest amount of crack front irregularity that suggests slightly faster cracking towards the crack flanks.

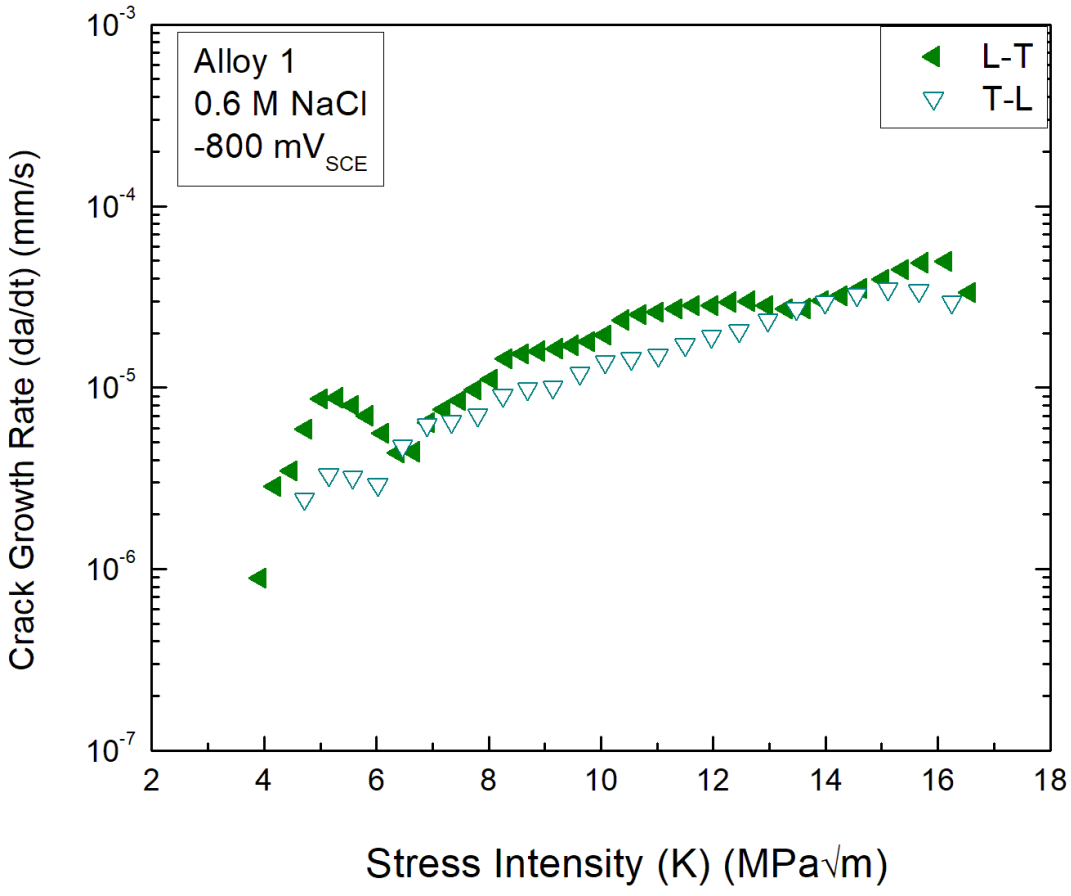

Figure 2.12: Crack growth rate versus stress intensity of Alloy 1 exposed to 0.6 M NaCl at a fixed potential of -800 mV_{SCE}, displaying the effect of loading orientation on IGSCC susceptibility.

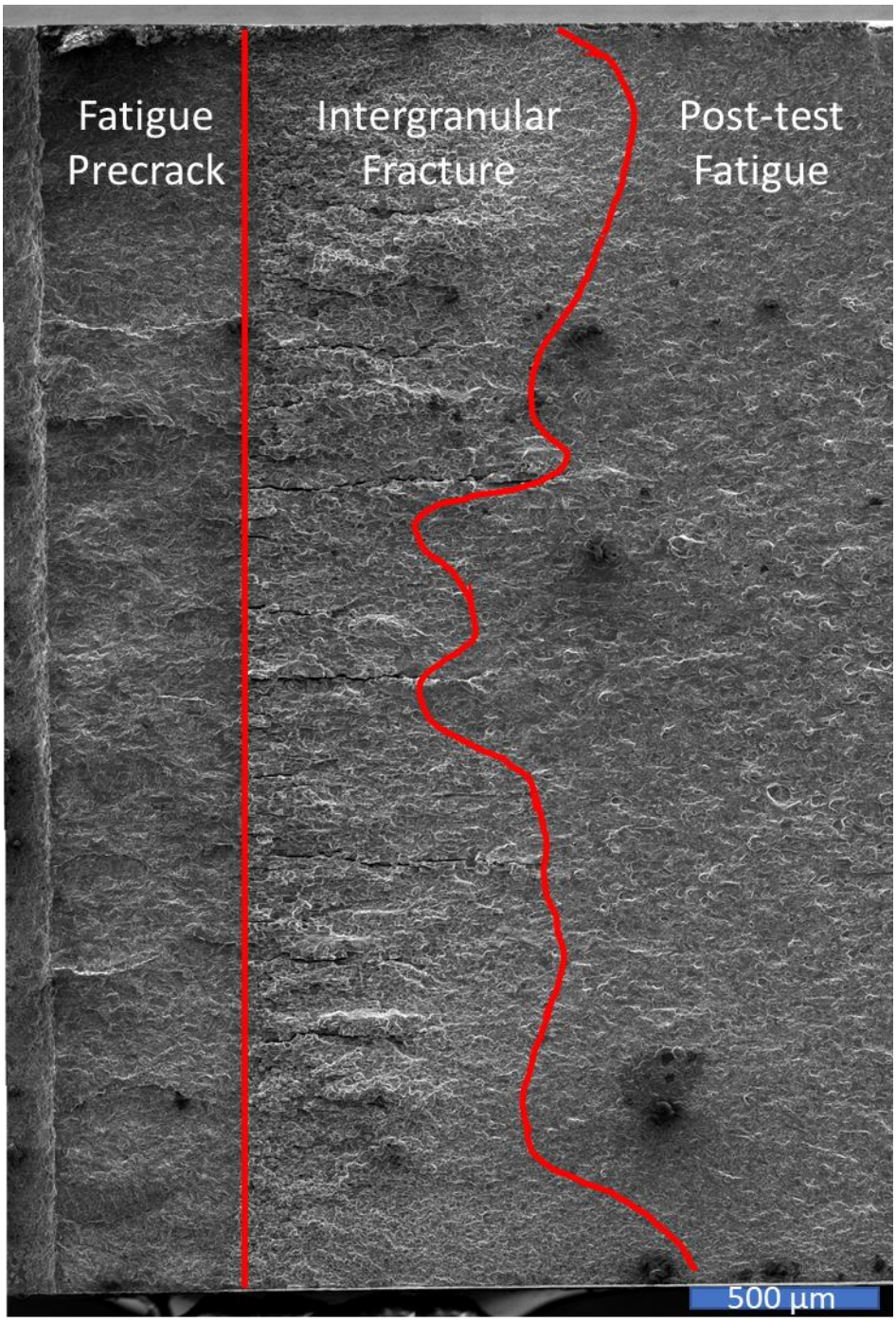

Figure 2.13: SEM fractography of the as received SENT specimen loaded in the LT orientation after testing in 0.6 M NaCl and -800 mV_{SCE} applied potential. The straight red line indicates the end of the fatigue precracked region to the left of the line, and intergranular fracture region to the left. The second red line indicates the end of the intergranular fracture that occurred during the EAC experiment, and to the right of the line is the post-test fatigued region.

2.4 Discussion

2.4.1 Grain Directionality and Orientation Dependence on Crack Growth Kinetics

The grain structure of Alloy 1 can be described as mostly equiaxed with some slight elongation in L and T directions in the LS plane and in the ST plane, respectively, as witnessed in Figure 2.4. There are a myriad of different post-processing approaches for 5xxx-series alloys which can result in a wide distribution of grain morphologies and extent of grain directionalities [30,31]. Outside of the fact that the material was rolled, the details of the thermo-mechanical processing for Alloy 1 is not known. Regardless, the observed grain structure is reasonable and within the bounds of grain structures reported for common 5xxx series materials.

McMahon *et al.* investigated the grain directionality of two different 5xxx series AA (5083 and 5456) in two different tempers, H131 and H116, which came from thick plates [7]. The resulting grain directionality ratios in the L/S plane were between 5.1 - 9.4, and 1.3 - 2.3 in the T/S plane. Additionally, the L/T ratio was found between 2.9 – 5.8. These ratios are much higher than the ones found for Alloy 1. This ratio is an important point of discussion for the reason that it can severely affect the crack propagation kinetics, as mentioned in the introduction. The authors showed the cracking kinetics changed significantly when the loading orientation was changed from the S-L to the T-L. The AA5083-H131 and -H116 loaded in the S-L orientation had three orders of magnitude faster crack growth rates than the T-L orientation for the same NAMLT value. It was also shown for AA5456-H116 that as the NAMLT value increased from 24 to 40 mg/cm^2, the difference between the crack growth rates in the S-L and T-L loading orientations was greater. These differences were attributed to the high level of grain directionality in the rolled AA5456 and AA5083. Specifically, for S-L oriented cracking there is an unabated crack path along the susceptible grain boundaries in the Mode I direction. Whereas in the T-L orientation, there is a very tortuous grain boundary path for the progression of a Mode I crack.

A study by Gao *et al.* [32] sought to also understand the effect of grain anisotropy on the IGSCC susceptibility of AA5083-H128 (unsensitized and sensitized) through slow strain rate tests (SSRT) experiments in humid air and 0.6 M NaCl. The grain directionality ratios were given as 2.3 in the LT plane, 8.7 in the LS plane, and 3.8 in the ST plane, all of which are much greater ratios than Alloy 1. It was observed that on sensitized tensile samples loaded in the S orientation had the greatest IGSCC susceptibility after SSRT conducted in 0.6 M NaCl, followed by the T and L oriented samples, owing to, in large part, the grain directionality differences observed. The authors also discuss the importance of the secondary phases and pre-existing intermetallic particles, since these constituents interact with dislocations during loading and can affect the overall mechanical behavior.

From these studies, it is useful to explore two aspects of the effect of grain directionality on the IGSCC behavior. First, for Alloy 1 that only has modest grain directionality what is the magnitude of the difference between cracking on the T-L versus the L-T orientations where there are only mild differences in the tortuosity of the grain boundary path for Mode I cracking. This is highlighted in on the EBSD images in Figure 2.14 where the Mode I crack path is shown relative to the loading orientation for both the T-L and the L-T loading orientations. Second, comparison of the Alloy 1 growth kinetics to kinetics from literature work on materials with very high levels of grain directionality. Specifically, since both the T-L and the L-T paths in Alloy 1 would have crack paths that would exhibit modest levels of tortuosity, as compared to literature alloys that have no tortuosity in the S-L and very high levels of tortuosity in the T-L. However, it should be noted that a direct comparison cannot be made from Alloy 1 to other Al-Mg alloys tested in the S-L orientation because Alloy 1 came from a thin sheet which could not produce specimen loaded in the S-L orientation. This lack of available data limits the comparison in cracking kinetics to only loading in the T-L orientation, shown in Figure 2. 15. It can be said that Alloy 1 displays faster crack growth and a higher level of IGSCC susceptibility in the T-L orientation than both AA5083 and AA5456 (data from [7]).

The findings of the loading orientation study revealed similar crack growth rates for the T-L and L-T orientations of Alloy 1 in 0.6 M NaCl with an applied potential of -800 mV_{SCE}. Using Figure 2.14, it can be reasoned that this result could be expected. If the grain structure of the LT plane is noted, the Mode I crack path appears to be similar, therefore making it reasonable that the L-T and T-L oriented samples have similar crack growth rates. This is because the crack path tortuosity does not vary significantly. The LS and ST planes must also be considered to make this argument. Figure 2.4 and Table 2.1 show that these two planes have similar microstructures, and similar grain directionality ratios. Since this is the plane that the crack progresses on (T-L orientation has crack propagation through the LS plane, and the L-T orientation has crack propagation through the ST plane), it is also reasonable to consider the results that were obtained. The driving force for IGSCC susceptibility is primarily β phase dissolution from continuous precipitation on the grain boundaries. Since the grain directionality of the ST and LT planes are similar, then there should theoretically be similar amount of β coverage on the grain boundaries. Therefore, it is unsurprising that the T-L and L-T loading orientations for mechanical testing had similar IGSCC susceptibility. Furthermore, in terms of in-plane anisotropy, Alloy 1 does not have high grain directionality nor severe crack path tortuosity which is reflected in the obtained crack growth kinetics. Therefore, it can be said that Alloy 1 does not exhibit more IGSCC susceptibility when the loading orientation of the specimen is changed in plane.

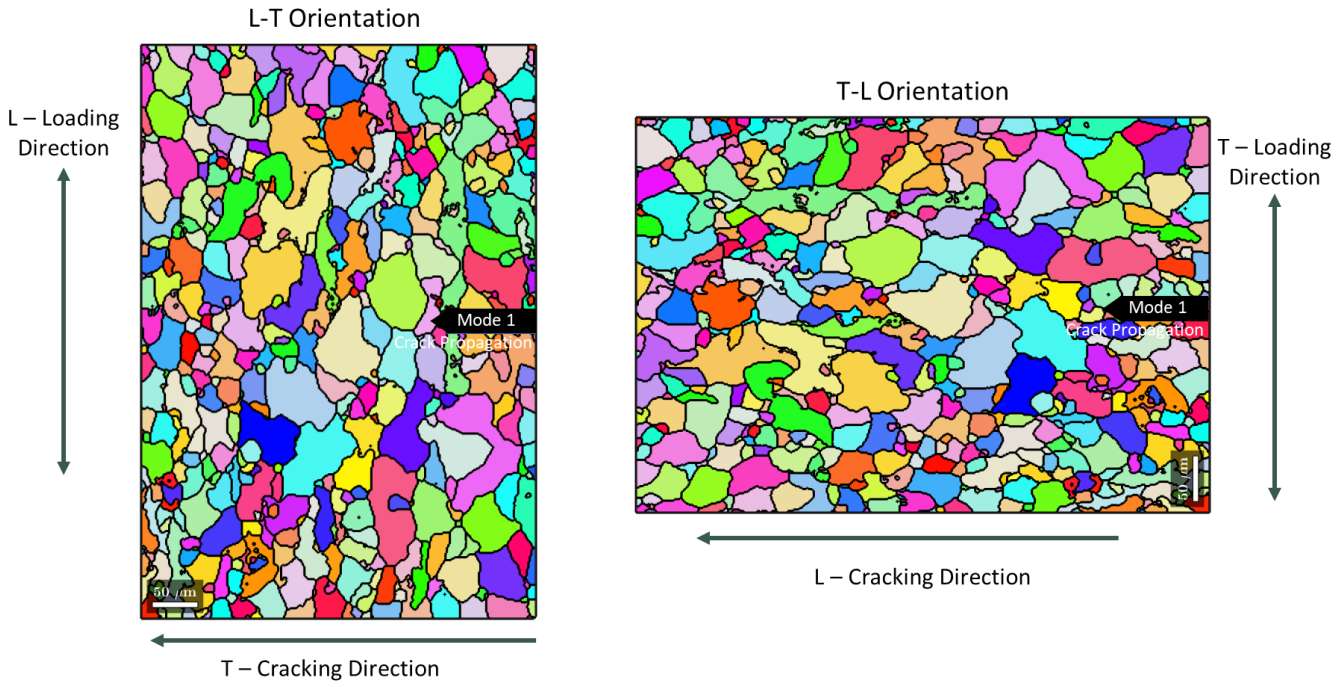

Figure 2.14: IPF maps highlighting the Mode I crack path in the L-T and T-L orientations. The LT plane image from Figure 2.4 a) was used to generate this schematic indicating the loading orientations and the cracking directions for the two different LEFM testing orientations. The black arrow acts as an imaginary notch, as would appear in a loaded SENT specimen.

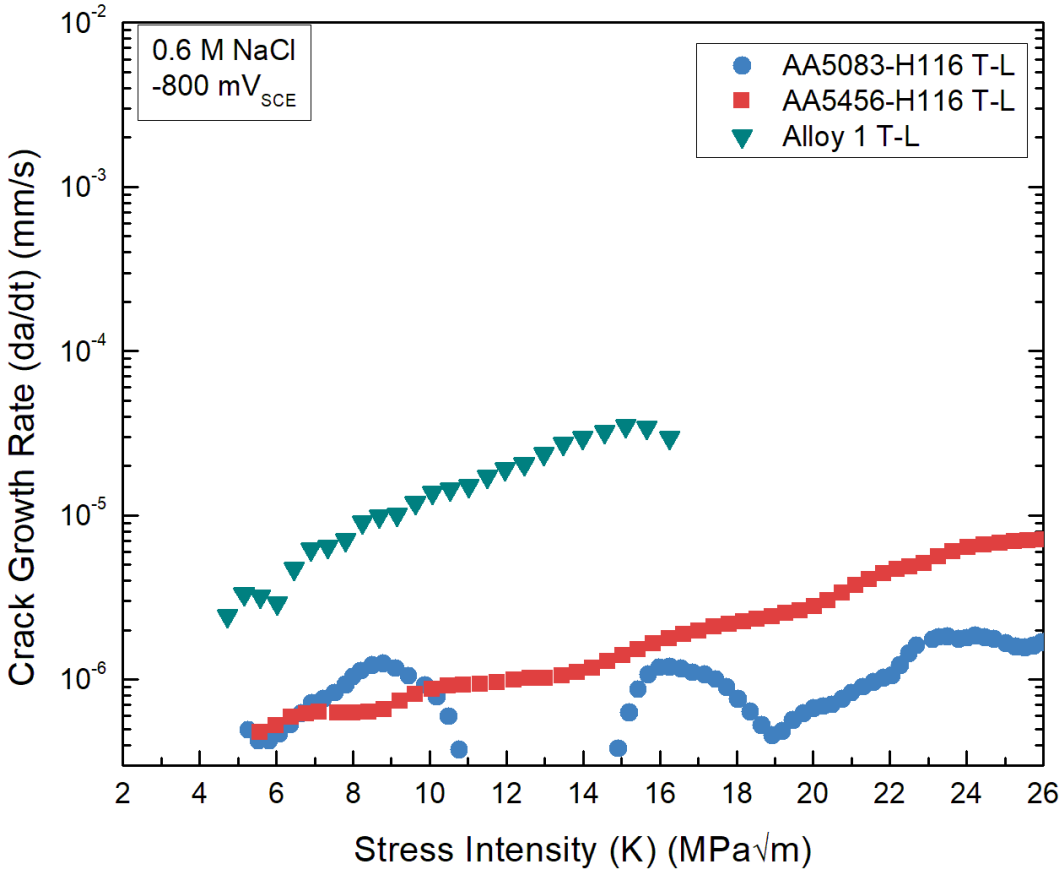

Figure 2. 15: Crack growth rate vs. stress intensity of AA5083-H116 (NAMLT 40), AA5456-H116 (NAMLT 40), and Alloy 1 (As received) in the T-L orientation.

2.4.2 Amount of Beta Phase on Grain Boundaries

The important findings from the linear grain boundary β coverage (LGBBC) analysis were: 1) the amount of β phase on the grain boundaries in the as received condition was high (approximately 82%) and 2) with increased sensitization, the amount of β phase on the grain boundaries did not significantly change. To address the high amount of β phase on the grain boundaries in the as received condition, it is important to note that no information on the thermal history of the material is available. However, it is useful to comment on factors that are known to impact the sensitization behavior. First, β phase precipitation is driven by exposure to elevated temperature, temperatures as low as 50°C [13,20,33]. Regarding the material specific features that impact sensitization, the Mg content is clearly going to play a dominant role as it governs the extent of supersaturation thus the driving force for sensitization.

Additionally, many have shown the dependence of β phase precipitation on grain boundary misorientation angle [13,14,16,17,23,34]. Additionally, the grain boundary plane has been shown to influence β phase precipitation [34]. D'Antuono *et al.* [13] showed the effect of cold rolling on the precipitation kinetics of β phase.

Alloy 1 had no significant changes in the LGBBC when subjected to laboratory oven sensitization at 100°C for 14 days. This is consistent with prior sensitization studies that show a saturation of the sensitization level for long exposures at elevated temperatures [35]. However, it is important to recognize the fidelity based limitations of the LGBBC metric. Critically, while this method does avoid accounting for intragranular beta as contributing to IGC and IGSCC susceptibility, it does not have the fidelity to account for subtle volume fraction changes that can occur. The metric used also does not account for the thickness of the β phase growing on the grain boundaries, which could have also differed between the as received and the sensitized material. Specifically, a value of 100% sensitization would mean that there is 100% coverage of grain boundaries with β phase. Further growth of the β phase (e.g. increasing the volume fraction) could occur beyond this point, however the LGBBC metric would not be able to accurately capture this growth.

The point above is consistent with a survey of sensitization in 5xxx series AA by Zhang *et al.* noted the increase in β phase thickness on grain boundaries at higher temperatures, for less time [36]. For example, the typical thickness of the β phase after 3000 hr at 70°C was approximately 10 nm, but was 15 nm after 100°C exposure for 1080 hr [36]. Furthermore, Crane *et al.* found similar results that increasing sensitization temperature increased beta precipitate thickness, but also noted that sensitization at 100°C for AA5083-H131 had constant spacing between beta particles on the grain boundaries at 144 hours and 720 hours, despite large changes in NAMLT (22 mg/cm^2 at 144 hours exposure to 100°C, vs. 50 mg/cm^2 at 720 hours exposure) [37]. Therefore, it is feasible to have β phase is size changes from the work cited, but also because of kinetics-based arguments which support growth of precipitates once the activation barrier for nucleation is overcome. These changes can only be captured in a linear-based grain boundary measurement if the growth observed is on the cross-sectional plane. Additional studies may look into cross-sectioning different metallographic changes and tracking the β phase growth as a function of sensitization time, as well as transmission electron microscopy studies on the preferred growth of β phase in certain orientations because of the inability to capture this information from the current study of Alloy 1. Even though the increase, or change, in β phase was not captured via LGBBC, it is still important to note the increased susceptibility of Alloy 1 with increased sensitization time, as could be expected from

previous literature. Additionally, Alloy 1 in the as received condition is predisposed to significant IGSCC susceptibility because of the high amount of β phase already present on the grain boundaries.

2.4.3 Sensitization Dependence on Crack Growth Kinetics

Environmental testing of the as received and sensitized SENT specimens in 0.6 M NaCl (polarized to -800 mV_{SCE}) showed an increase in crack growth kinetics in the samples that underwent an additional sensitization exposure (Figure 2.9). While researchers have shown increased IGSCC susceptibility for increased NAMLT values [3,37,38], the current data shows that the IGSCC susceptibility increases despite constant NAMLT and LGBBC values. This could potentially be due to either (1) the fact that the NAMLT and LGBBC metrics do not fully describe the volume fraction of beta on the grain boundary, and/or (2) the volume fraction of β is constant but there are other changes in the microstructure caused by the additional thermal treatment. The first would be straight forward and consistent with the governing mechanism. Specifically, Crane *et al.* explicitly defined β dissolution as the primary step in an anodic dissolution-hydrogen embrittlement mechanism for IGSCC through her work on AA5083-H131 [37], and others have also commented on the same trends in other alloys of differing temper, compositions, heat treatments, etc. all supporting this mechanism [3,7,38]. The main takeaway is that sensitization increases the amount of β phase precipitation and therefore increases the susceptibility to IGSCC. It is also possible that the volume fraction of the β on the grain boundary is not changing during the thermal treatment but there are other metallurgical modifications (e.g. Mg segregation, etc.) that are impacting the material resistance for a constant grain boundary volume fraction. A detailed analysis of the underlying cause for the increase in IGSCC susceptibility despite the constant LGBBC is outside the scope of this thesis. However, the first step in future work to analyze this behavior would be a higher resolution characterization (TEM) of the grain boundary beta coverage after the additional thermal treatment.

2.5 Conclusions

In summary, Alloy 1 was first investigated for basic material characteristics such as grain size and amount of beta phase on the grain boundaries. This information was used to inform environmentally-assisted cracking data performed on SENT specimen of Alloy 1. From the experiments conducted and the analysis thereafter, the following conclusions can be made:

1. Alloy 1 has a mostly equiaxed grain structure in the LT plane and some modest level of grain directionality in the ST and LS planes. The modest level of grain directionality does not contribute to changes in IGSCC susceptibility when the loading orientation is changed from the L-T to the T-L.
2. The linear grain boundary beta phase metric could not distinguish differences in IGSCC susceptibility because of increased susceptibility for sensitized specimen despite similar percentages of beta grain boundary coverage between the as received and sensitized conditions.
3. Despite unchanging amounts of beta coverage on the grain boundaries in the as received and sensitized conditions, the crack growth kinetics of the sensitized specimen was increased, meaning greater IGSCC susceptibility, over the as received specimen.

References

[1] G.M. Scamans, N.J.H. Holroyd, C.D.S. Tuck, THE ROLE OF MAGNESIUM SEGREGATION IN THE INTERGRANULAR STRESS CORROSION CRACKING OF ALUMINIUM ALLOYS, 1987.

[2] Standard Test Method for Determining the Susceptibility to Intergranular Corrosion of 5XXX Series Aluminum Alloys by Mass Loss After Exposure to Nitric Acid (NAMLT Test) 1, (n.d.). https://doi.org/10.1520/G0067-18.

[3] M.E. McMahon, R.L. Haines, P.J. Steiner, J.M. Schulte, S.E. Fakler, J.T. Burns, Beta phase distribution in Al-Mg alloys of varying composition and temper, Corros Sci 169 (2020). https://doi.org/10.1016/j.corsci.2020.108618.

[4] R.H. Jones, D.R. Baer, M.J. Danielson, J.S. Vetrano, Role of Mg in the Stress Corrosion Cracking of and Al-Mg Alloy, Metallurgical and Materials Transactions A 32A (2001) 1699–1711.

[5] M.E. McMahon, J.R. Scully, J.T. Burns, Mitigation of Intergranular Stress Corrosion Cracking in Al–Mg by Electrochemical Potential Control, JOM 69 (2017) 1389–1397. https://doi.org/10.1007/s11837-017-2362-2.

[6] P.J. Steiner, Z.D. Harris, C. Vicente Moraes, R.G. Kelly, J.T. Burns, Investigation of IG-SCC Growth Kinetics in Al-Mg Alloys in Thin Film Environments, Corrosion 77 (2021) 838–852. https://doi.org/10.5006/3833.

[7] M.E. McMahon, P.J. Steiner, A.B. Lass, J.T. Burns, The effect of loading orientation on the stress corrosion cracking of Al-Mg alloys, Corrosion 73 (2017) 713–723. https://doi.org/10.5006/2343.

[8] P.J. Steiner, Z.D. Harris, J.T. Burns, Effect of Chloride Concentration on the Environment-Assisted Cracking Behavior of an Al-Mg Alloy in Atmospheric Environments, Corrosion 79 (2023) 1223–1233. https://doi.org/10.5006/4279.

[9] P.J. Steiner, J.T. Burns, Mechanistic studies of intergranular stress corrosion cracking in Al-Mg alloys under atmospheric exposure conditions, Corrosion 74 (2018) 1117–1131. https://doi.org/10.5006/2853.

[10] M. Pourbaix, Atlas of Electrochemical Equilibria in-Aqueous Solutions, n.d.

[11] M.E. McMahon, Z.D. Harris, J.R. Scully, J.T. Burns, The effect of electrode potential on stress corrosion cracking in highly sensitized Al–Mg alloys, Materials Science and Engineering: A 767 (2019). https://doi.org/10.1016/j.msea.2019.138399.

[12] Standard Practice for Operating Salt Spray (Fog) Apparatus 1, (n.d.). https://doi.org/10.1520/B0117-19.

[13] D. Scotto D'Antuono, J. Gaies, W. Golumbfskie, M.L. Taheri, Direct measurement of the effect of cold rolling on β phase precipitation kinetics in 5xxx series aluminum alloys, Acta Mater 123 (2017) 264–271. https://doi.org/10.1016/j.actamat.2016.10.060.

[14] R. Zhang, R.K. Gupta, C.H.J. Davies, A.M. Hodge, M. Tort, K. Xia, N. Birbilis, The influence of grain size and grain orientation on sensitization in AA5083, in: Corrosion, 2016. https://doi.org/10.5006/1703.

[15] J.G. Kaufman, Stress-Corrosion Cracking of Aluminum Alloys, in: Properties and Selection of Aluminum Alloys, ASM International, 2019: pp. 79–95. https://doi.org/10.31399/asm.hb.v02b.a0006545.

[16] D. Scotto D'Antuono, J. Gaies, W. Golumbfskie, M.L. Taheri, Grain boundary misorientation dependence of β phase precipitation in an Al-Mg alloy, Scr Mater 76 (2014) 81–84. https://doi.org/10.1016/j.scriptamat.2014.01.003.

[17] Y. Zhao, M.N. Polyakov, M. Mecklenburg, M.E. Kassner, A.M. Hodge, The role of grain boundary plane orientation in the β phase precipitation of an Al-Mg alloy, Scr Mater 89 (2014) 49–52. https://doi.org/10.1016/j.scriptamat.2014.07.003.

[18] X. Sauvage, N. Enikeev, R. Valiev, Y. Nasedkina, M. Murashkin, Atomic-scale analysis of the segregation and precipitation mechanisms in a severely deformed Al-Mg alloy, Acta Mater 72 (2014) 125–136. https://doi.org/10.1016/j.actamat.2014.03.033.

[19] F. Qin, C. Yang, H. Qi, C. Liu, H. Qi, Grain Size, Precipitation Behavior, and Mechanical Properties through the Thickness of Al-Mg-Si Aluminum Alloy Rings Produced by Compact Cast-Rolling Compound Forming, J Mater Eng Perform 31 (2022) 2329–2340. https://doi.org/10.1007/s11665-021-06326-7.

[20] D.L. Foley, A.C. Leff, A.C. Lang, M.L. Taheri, Evolution of β-phase precipitates in an aluminum-magnesium alloy at the nanoscale, Acta Mater 185 (2020) 279–286. https://doi.org/10.1016/j.actamat.2019.10.024.

[21] M. Lyn, C. Lim, Intergranular Corrosion Propagation in Sensitized Al-Mg Alloys, 2016.

[22] J.H. Ai, M.L.C. Lim, J.R. Scully, Effective hydrogen diffusion in aluminum alloy 5083-H131 as a function of orientation and degree of sensitization, Corrosion 69 (2013) 1225–1239. https://doi.org/10.5006/0987.

[23] J. Desai Choundraj, J. Kacher, Influence of misorientation angle and local dislocation density on β-phase distribution in Al 5xxx alloys, Sci Rep 12 (2022). https://doi.org/10.1038/s41598-022-05948-8.

[24] Designation: E112 − 13 Standard Test Methods for Determining Average Grain Size 1, (n.d.). https://doi.org/10.1520/E0112-13R21.

[25] Standard Test Method for Linear-Elastic Plane-Strain Fracture Toughness of Metallic Materials 1, (n.d.). https://doi.org/10.1520/E0399-22.

[26] R.P. Gangloff, D.C. Slavik, R.S. Piascik, R.H. Van Stone, Direct Current Electrical Potential Measurement of the Growth of Small Cracks, American Society for Testing and Materials (1992) 116–168.

[27] Standard Test Method for Measurement of Fatigue Crack Growth Rates 1, (n.d.). https://doi.org/10.1520/E0647-23A.

[28] Z.D. Harris, J.T. Burns, On the loading rate dependence of environment-assisted cracking in sensitized AA5456-H116 exposed to marine environments, Corros Sci 201 (2022). https://doi.org/10.1016/j.corsci.2022.110267.

[29] R.P. Gangloff, H.M. Ha, J.T. Burns, J.R. Scully, Measurement and modeling of hydrogen environment-assisted cracking in monel K-500, Metall Mater Trans A Phys Metall Mater Sci 45 (2014) 3814–3834. https://doi.org/10.1007/s11661-014-2324-z.

[30] J.X. Zhang, M. Ma, W.C. Liu, Effect of initial grain size on the recrystallization and recrystallization texture of cold-rolled AA 5182 aluminum alloy, Materials Science and Engineering: A 690 (2017) 233–243. https://doi.org/10.1016/j.msea.2017.03.015.

[31] P. Ebenberger, P.J. Uggowitzer, B. Gerold, S. Pogatscher, Effect of compositional and processing variations in new 5182-type AlMgMn alloys on mechanical properties and deformation surface quality, Materials 12 (2019). https://doi.org/10.3390/ma12101645.

[32] W. Gao, D. Wang, M. Seifi, J.J. Lewandowski, Anisotropy of corrosion and environmental cracking in AA5083-H128 Al-Mg alloy, Materials Science and Engineering: A 730 (2018) 367–379. https://doi.org/10.1016/j.msea.2018.06.021.

[33] J.L. Searles, P.I. Gouma, R.G. Buchheit, Stress Corrosion Cracking of Sensitized AA5083 (Al-4.5Mg-1.0Mn), n.d.

[34] A.J. Davenport, Y. Yuan, R. Ambat, B.J. Connolly, M. Strangwood, A. Afseth, G.M. Scamans, Intergranular Corrosion and Stress Corrosion Cracking of Sensitised AA5182, Materials Science Forum 519–521 (2006) 641–646. https://doi.org/10.4028/www.scientific.net/msf.519-521.641.

[35] C.: Yuan, Yudie, Localised corrosion and stress cracking of aluminium-magnesium alloys, University of Birmingham, 2005.

[36] R. Zhang, S.P. Knight, R.L. Holtz, R. Goswami, C.H.J. Davies, N. Birbilis, A survey of sensitization in 5xxx series aluminum alloys, in: Corrosion, National Assoc. of Corrosion Engineers International, 2016: pp. 144–159. https://doi.org/10.5006/1787.

[37] C.B. Crane, R.P. Gangloff, Stress corrosion cracking of Al-Mg alloy 5083 sensitized at low temperature, in: Corrosion, National Assoc. of Corrosion Engineers International, 2016: pp. 221–241. https://doi.org/10.5006/1766.

[38] M.E. McMahon, P.J. Steiner, A.B. Lass, J.T. Burns, The effect of temper and composition on the stress corrosion cracking of Al-Mg alloys, Corrosion 73 (2017) 347–361. https://doi.org/10.5006/2317.

[39] Z.D. Harris, J.T. Burns, On the loading rate dependence of environment-assisted cracking in sensitized AA5456-H116 exposed to marine environments, Corros Sci 201 (2022). https://doi.org/10.1016/j.corsci.2022.110267.

[40] M.E. McMahon, J.R. Scully, J.T. Burns, Mitigation of Intergranular Cracking in Al-Mg Alloys via Zn-Based Electrode Potential Control in Sodium Chloride Solution, Corrosion 75 (2019) 911–928. https://doi.org/10.5006/3185.

[41] R. Sanders, J. Staley, A History of Wrought Aluminum Alloys and Applications, in: Properties and Selection of Aluminum Alloys, ASM International, 2019: pp. 157–201. https://doi.org/10.31399/asm.hb.v02b.a0006516.

[42] N. Brown, P. Kramer, F. Friedersdorf, M. Schindelholz, J. Siegel, Environmentally assisted cracking measurements in structural aluminum alloys under accelerated test conditions, Corrosion 72 (2016) 1351–1362. https://doi.org/10.5006/2085.

[43] C. Liu, J. Srinivasan, R.G. Kelly, Editors' Choice—Electrolyte Film Thickness Effects on the Cathodic Current Availability in a Galvanic Couple, J Electrochem Soc 164 (2017) C845–C855. https://doi.org/10.1149/2.1641713jes.

[44] F. Ge, L. Zhang, H. Tian, M. Yu, J. Liang, X. Wang, Stress Corrosion Cracking Behavior of 2024 and 7075 High-Strength Aluminum Alloys in a Simulated Marine Atmosphere Contaminated with SO2, J Mater Eng Perform 29 (2020) 410–422. https://doi.org/10.1007/s11665-019-04537-7.

[45] M. WANG, L. WANG, K. PANG, Y. LIU, Y. WANG, Z. CUI, Understanding stress corrosion cracking behavior of 7085-T7651 aluminum alloy in polluted atmosphere, Chinese Journal of Aeronautics 36 (2023) 408–421. https://doi.org/10.1016/j.cja.2023.06.011.

[46] E.M. Arnold, J.J. Schubbe, P.J. Moran, R.A. Bayles, Comparison of SCC thresholds and environmentally assisted cracking in 7050-T7451 aluminum plate, J Mater Eng Perform 21 (2012) 2480–2486. https://doi.org/10.1007/s11665-012-0204-5.

[47] PENAIR ® M5571, n.d.

[48] G.A. Truesdale, A.L. Downing, Solubility of Oxygen in Water, Nature 173 (1954) 1236.

[49] I.W. Huang, B.L. Hurley, F. Yang, R.G. Buchheit, Dependence on Temperature, pH, and Cl- in the Uniform Corrosion of Aluminum Alloys 2024-T3, 6061-T6, and 7075-T6, Electrochim Acta 199 (2016) 242–253. https://doi.org/10.1016/j.electacta.2016.03.125.

[50] C.N. Panagopoulos, E. Georgiou, K.I. Giannakopoulos, P.G. Orfanos, Effect of ph on stress corrosion cracking of 6082 al alloy, Metals (Basel) 8 (2018). https://doi.org/10.3390/met8080578.

[51] W.-T. Tsai, J.-B. Duh, J.-J. Yeh, J.-T. Lee, Y.-C. Chang"', Effect of pH on Stress Corrosion Cracking of 7050-T7451 Aluminum Alloy in 3.5 wt% NaCl Solution *, 1990. http://meridian.allenpress.com/corrosion/article-pdf/46/6/444/1530787/1_3585130.pdf.

[52] Z. Dan, I. Muto, N. Hara, Effects of environmental factors on atmospheric corrosion of aluminium and its alloys under constant dew point conditions, Corros Sci 57 (2012) 22–29. https://doi.org/10.1016/j.corsci.2011.12.038.

[53] T.F. Cui, D.X. Liu, P.A. Shi, J.J. Liu, Y.H. Yi, H.L. Zhou, Effect of NaCl concentration, pH value and tensile stress on the galvanic corrosion behavior of 5050 aluminum alloy, Materials and Corrosion 67 (2016) 72–83. https://doi.org/10.1002/maco.201408189.

[54] E. Bumiller, INTERGRANULAR CORROSION IN AA5XXX ALUMINUM ALLOYS WITH DISCONTINUOUS PRECIPITATION AT THE GRAIN BOUNDARIES A Dissertation Presented to, 2011.

[55] J.A. Lyndon, R.K. Gupta, M.A. Gibson, N. Birbilis, Electrochemical behaviour of the β-phase intermetallic (Mg2Al3) as a function of pH as relevant to corrosion of aluminium-magnesium alloys, Corros Sci 70 (2013) 290–293. https://doi.org/10.1016/j.corsci.2012.12.022.

[56] B. Zaid, D. Saidi, A. Benzaid, S. Hadji, Effects of pH and chloride concentration on pitting corrosion of AA6061 aluminum alloy, Corros Sci 50 (2008) 1841–1847. https://doi.org/10.1016/j.corsci.2008.03.006.

[57] C.B. Crane, R.G. Kelly, R.P. Gangloff, Crack chemistry control of intergranular stress corrosion cracking in sensitized Al-Mg, in: Corrosion, National Assoc. of Corrosion Engineers International, 2016: pp. 242–263. https://doi.org/10.5006/1852.

Chapter 3: The effect of applied potential on the crack growth kinetics of Alloy 1 in 0.6 M NaCl

3.1 Introduction

Al-Mg alloys (commonly referred to as AA5xxx series) are typically alloyed with greater than 3 wt% Mg creating a supersaturated solid solution which greatly improves the strength and allows them to be used as structural components in different industries. Exposure of these alloys to elevated temperatures for sufficient periods of time causes precipitation of beta phase on the grain boundaries. As such, these alloys become susceptible to intergranular corrosion (IGC) and intergranular stress corrosion cracking (IGSCC) because of the known electrochemical potential difference that exist between the alpha-Al matrix and the more anodic beta phase. Selective dissolution of the beta phase is extremely detrimental to the integrity of AA5xxx and can cause failures at times earlier than predicted.

Recent research efforts have shown the likely mechanism for this phenomenon to be a combined anodic dissolution-hydrogen embrittlement process [4,6–9,11,15,37,39]. As the name suggests, the mechanism depends on the anodic dissolution of the beta phase (and subsequently the α-Al matrix) and is the first step towards crack propagation. The increase in Al^{3+} ions from dissolution in the crack tip allow for combination with the surrounding water molecules, enabling hydrolysis where H^+ is formed as a product, effectively lowering the pH withing the crack tip. Low pH combined with increased [Cl^-] gives an aggressive crack chemistry promoting the generation of hydrogen. Atomic H is first adsorbed onto the surface of the material and then absorbed at the crack tip. Diffusion of hydrogen ahead of the crack tip enables local embrittlement of the material, furthering crack advance. The important first step in mitigating this mechanism is deterring anodic dissolution of the beta phase. Jones *et al.* applied cathodic overpotentials of -0.550 V_{SCE} (-1.39 V_{SCE}) to AA5083 compact tension specimen exposed to in 3.5% NaCl and showed there was no significant crack extension in the solution treat and quenched and aged 1 hr at 175°C conditions, stating there was no effect of cathodic polarization on the crack growth rate [4]. Results from this work also commented on the possibility for a combined anodic dissolution-H induced mechanism by the fact that anodic dissolution of the beta phase was occurring along with H reduction as corrosion of beta progressed [4]. McMahon *et al*. furthered this understanding by exposing AA5456-H116 to 0.6 M NaCl solutions and applied potentials ranging from -0.6 VSCE to -1.7 VSCE [11]. The authors made a clear connection between the applied potential dependency of AA5456-H116 to the H generation and absorption occurring at the crack tip – serving to confirm the involvement of hydrogen on the crack growth mechanism [11].

Each of these studies were conducted on Al-Mg alloys in 3.5% (0.6 M) NaCl solutions. Therefore, it was also important to capture the dependency of solution chemistry, specifically chloride concentration, on the studied dependence of IGSCC susceptibility on applied cathodic potential. A study by McMahon *et al.* directly linked the IGSCC susceptibility of AA5456-H116 to the beta pitting (breakdown) potential, showing that cathodic potentials below the open circuit potential of AA5456-H116 had decreased crack growth kinetics, but applied potentials at or below the beta breakdown potential had no IGSCC [5]. These key findings further informed the mechanism for crack growth in the AA5xxx series and has thus allowed for the development of mitigation strategies that effectively apply cathodic potentials lower than the beta breakdown potential. One example of this by McMahon *et al.* showed how the application of a Zn-rich primer and Zn anode mitigated IGSCC in AA5456-H116 via cathodic protection [40].

Altogether, studies on the applied cathodic potential of the AA5xxx series below the beta breakdown potential can retard crack growth based on the mechanistic understanding of crack growth for these alloys as anodic dissolution enabled hydrogen embrittlement [4,5,11,40]. The objective of this work is to determine whether Alloy 1 exhibits the same cathodic potential dependence as the other AA5xxx alloys. This study will inform the community of ways in which IGSCC can be retarded or potentially ceased with certain applied potentials. If Alloy 1 has the same trend as other AA5xxx then the anodic dissolution hydrogen embrittlement mechanism can be thought of as the mechanism for IGSCC, as has been shown previously [4,5,11,40].

3.2 Materials and Methods

3.2.1 Sample Design

Alloy 1 in the as received condition, as described in Chapter 2, was machined into single edge notch tensile (SENT) specimens. SENT specimen were oriented such that the tensile loading was parallel to the T direction (transverse, normal to rolling direction), and the Mode 1 cracking progress in the L direction (rolling direction), shorted as the TL orientation. The thickness of the specimens were 3.33 mm; the specimen width was 25.4 mm and had a total length of 177.8 mm. An electrical discharge machined (EDM) notch was placed at the center of specimen length, with a depth equaling 5.7 mm.

3.2.2 Linear Elastic Fracture Mechanics (LEFM) Testing

Stress corrosion susceptibility of Alloy 1 was probed using Linear Elastic Fracture Mechanics (LEFM) approach. The SENT specimens were fatigue precracked in lab air to 6.0 mm with a final stress intensity (K) of 4 MPa√m. Slow rising displacement experiments following the precrack were controlled

via K and conducted at a rate of 1 MPa√m/hr. Direct current potential difference (dcPD) was used to monitor crack growth, and has a resolution limit of 0.5 um. The details of this method can be read elsewhere [26].

An acrylic environmental cell was placed around the sample following the fatigue precrack and filled with 200 mL of 0.6 M NaCl (pH 6.0). A reservoir totaling 2 L of the same electrolyte was continuously flowed at a rate of 100 mL/min at ambient temperature. The sample was fully immersed, with 25.4 mm length of exposure around the EDM notch (with the notch being at the center). A three electrode system was utilized for potentiostatic control. An insulated copper wire welded to the SENT specimen was used as the working electrode, a saturated calomel electrode (SCE) as the reference electrode, and Pt mesh as the counter electrode. A Biologic PG-581 handheld potentiostat was used to measure open circuit potential (OCP) measurement before the start of the experiment, while the SENT specimen was loaded in tension (1 kN of force), and for potentiostatic holds. After establishing stable OCP after approximately 1 hour, samples were loaded at a dK/dt of 1 MPa√m/hr. Separate tests were conducted following this protocol with potentiostatic holds of –800 mV_{SCE}, -900 mV_{SCE}, -950 mV_{SCE}, -1000 mV_{SCE}, and -1100 mV_{SCE}. Note that an applied potential of -800 mV is meant to force a potential near the OCP for this alloy in 0.6 M NaCl, and therefore can be thought of as a fixed OCP.

Following the K rise experiment, solution was removed from the cell and the SENT specimen were post-test fatigued to failure. One half of the specimen was sonicated in methanol and the fracture surface was imaged using FEG Quanta 650 SEM. Secondary electron images were acquired using the Everhart-Thornley detector (ETD) at a spot size of 3.0 and an accelerating voltage of 10.0 kV.

Consistent with what was reported in Chapter 2, crack growth rates were calculated using the crack length values captured via dcPD and following the seven point incremental polynomial method akin to what is described for fatigue crack growth rates in ASTM E647 Appendix XI [27]. However, there are two sensitivities of the dcPD method that need to be addressed when reporting crack growth rates. The first is the sensitivity to plasticity related extension of the plastic zone size, which is denoted as a crack extension through dcPD data accumulation. Therefore, the resolution limit correction, as was outlined previously by [28], was performed and utilized the same correction function discussed in an earlier chapter. The second issue that must be addressed is the decrease in crack length that occurs with electrical contact between the two crack faces – known as shorting. To correct for this decrease in crack length, the shorting correction, described by Gangloff *et al.* [29] was performed, and details of which were discussed in Chapter 2.

3.2.3 Flat Cell Electrochemical Testing

Alloy 1 was used for electrochemical testing. Samples were cut, exposing at least 1 cm^2 area of the LT plane. Before electrochemical testing, the samples were polished to 1200 grit with deionized (DI) water. Pure β phase (Al_3Mg_2) was synthesized in prior work [5] and was mounted in epoxy and polished to 1200 grit with ethanol.

Shortly after polishing, the samples were placed in an electrochemical flat cell with a 1 cm^2 exposure area. A typical three electrode system was utilized for corrosion testing where the working electrode was either Alloy 1 or Al_3Mg_2, the counter electrode was Pt mesh, and the reference electrode was a saturated calomel electrode (SCE). Each of these electrodes were connected via alligator clips to a Biologic VMP3 Potentiostat. Prior to obtaining corrosion kinetics, samples were exposed to 0.6 M NaCl solution for 60 minutes (Alloy 1) or 30 minutes (beta alloy) to obtain stable open circuit potential (OCP) conditions. Following the OCP hold, anodic or cathodic potentiodynamic scans were run at a rate of 0.167 mV_{SCE}/s. Anodic scans were started at OCP and the potential was increased at the scan rate until reaching +0.5 V_{SCE}. Cathodic scans were run in a similar fashion, starting at OCP and decreasing the potential at 0.167 mV/s until reaching a potential of –2.0 V_{SCE}. Note, cathodic polarization scans were only obtained for Alloy 1 in the different solutions because of the expected nobility of Alloy 1 compared to Al_3Mg_2. During these experiments, the corrosion kinetics (i.e. corrosion current) were obtained as the potential was stepped. After the potentiodynamic scans were completed, samples were removed from the flat cell, rinsed with DI water and imaged using a Hirox RH-8800 optical microscope. Each anodic and cathodic polarization scan were run three times in each solution and the results show one representative curve of each.

3.3 Results

3.3.1 Corrosion Kinetics via Polarization Curves

The anodic and cathodic kinetics of Alloy 1 in 0.6 M NaCl presented in Figure 3.1 identify the OCP to be -865 mV_{SCE}. The pitting potential from the anodic curve of Alloy 1 is approximately -780 mV_{SCE}, which is near the OCP, indicating almost immediate breakdown of the passive film. Note that some of the anodic polarization curves of Alloy 1 in 0.6 M NaCl did not even have a pitting potential, and therefore it is expected that pitting, or localized corrosion would occur at potentials above the open circuit potential. The OCP of Al_3Mg_2 in 0.6 M NaCl is -1.48 mV_{SCE} approximately 780 mV_{SCE} below that of Alloy 1, as shown in **Error! Reference source not found.**, verifying that beta phase is anodic to the alpha-Al matrix when p recipitated on the grain boundaries and is the driving force for selective dissolution. The pitting potential

is observed to be -0.95 mV_{SCE}. The breakdown potential (i.e. pitting potential) is much larger than the OCP of Al_3Mg_2 in 0.6 M NaCl meaning there is a significant potential range of passivity.

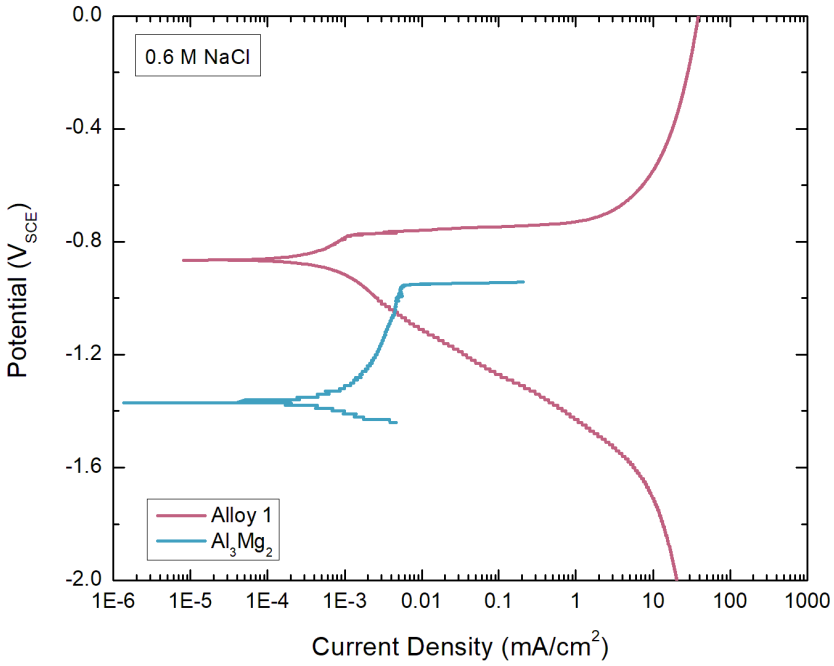

Figure 3.1: Anodic and cathodic polarization curves of Alloy 1 and anodic curve of beta phase in 0.6 M NaCl

3.3.2 Crack Growth Kinetics via da/dt vs. K curves

Crack growth rate (da/dt) vs K of each applied potential can be viewed in Figure 3.2. The threshold for cracking (K_{TH}) of the experiments with the applied potential of -800, -900, and -950 mV_{SCE} are all approximately 4-5 MPa√m. However, the K_{TH} for the test at -1000 mV_{SCE} is significantly increased to almost 7 MPa√m. Additionally, as expected there is a decrease in crack growth rates with increasing applied cathodic potential (i.e. more negative). The crack growth rates of the -800 and -900 mV_{SCE} applied potentials have similar results, with the stage II regime of the -900 mV_{SCE} applied potential test being slightly lower than the test at -800 mV_{SCE}. Note that the most negative cathodic potential tested (-1100 mV_{SCE}) showed no crack growth, evident from the fracture surface in Figure 3.3 since there is no change in fracture morphology from the fatigue precrack region to the post test fatigue region. These results were expected for Alloy 1 (an Al-Mg alloy) based on the prior work of McMahon *et al.* [5] who showed the influence of cathodic polarization as a mitigation technique for AA5xxx series whose mechanism of crack growth is anodic dissolution enabled hydrogen embrittlement. This work directly linked the decrease in

IGSCC susceptibility with the β breakdown potential, because of the cessation of anodic dissolution of the beta phase (which is the first step in the operative crack growth mechanism).

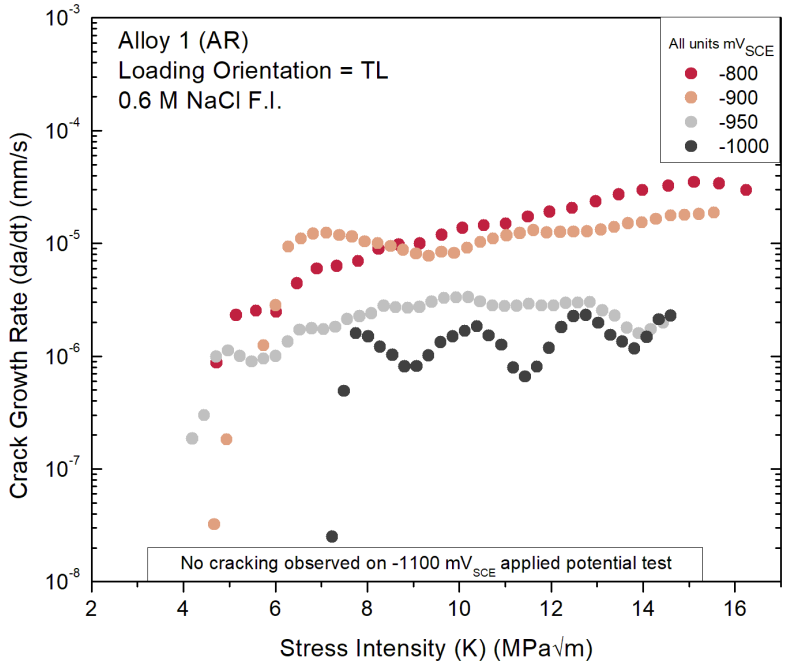

Figure 3.2: Crack growth rate versus stress intensity of Alloy 1 exposed to 0.6 M NaCl, displaying the IGSCC dependence on applied potential.

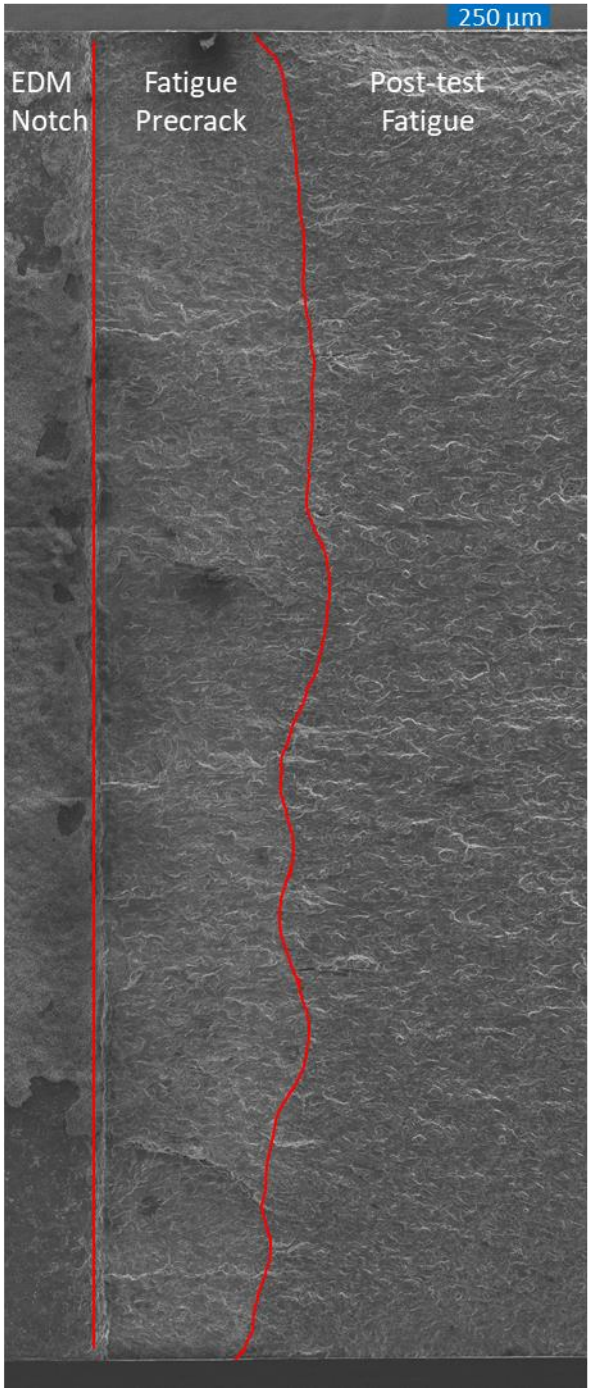

Figure 3.3: SEM fractography of Alloy 1 exposed to 0.6 M NaCl with an applied potential of -1100 $mV_{SCE,}$ The straight red line indicates the end of the EDM notch (to the left of the line), and fatigue precrack region to the left. The second red line indicates the end of the precracked region, and to the right of the line is the post-test fatigued region, indicating that no intergranular fracture occurred during the SCC experiment.

3.4 Discussion

The major finding from the experiments conducted is the ability to stop crack growth at a critical cathodic applied potential of -1100 mV_{SCE} to Alloy 1 in 0.6 M NaCl solution. This is consistent with the proposed anodic dissolution-hydrogen embrittlement based mechanism, but it is worth a discussion to explore the subtleties associated with Alloy 1 EAC behavior. First, it was recognized that the beta pitting (breakdown) potential was -950 mV_{SCE} in 0.6 M NaCl. If beta dissolution is the first process in this mechanism, then it could be reasoned that the crack growth would cease at applied potentials of -950 mV_{SCE}, since there should be no theoretical dissolution at applied potentials below this critical value. However, there are several points to consider. The bulk applied potential is not the same as the crack tip potential. It has been reported that the alpha breakdown potential at the crack tip can vary up to 100 mV_{SCE} difference than the bulk breakdown potential because of the local crack tip chemistry that has elevated concentrations of cations (Al^{3+} and Mg^{2+}) (and subsequently Cl- for charge neutrality) [21]. This is significant relative to the proposed mechanism which suggests cathodic applied potentials of -900 mV_{SCE} are applied potentials in which alpha breakdown is suppressed, which is reasonable when looking at **Error! R eference source not found.** because of the modest decrease in crack growth rates at -900 mV_{SCE} applied potential, and significant decreases in crack growth kinetics at applied potentials below -900 mV_{SCE}. While not explicitly studied, it is also fair to assume that this sort of potential shift could be possible for the beta breakdown potential at the crack tip, shifting to values of approximately -1050 mV_{SCE}. Therefore, it is reasonable that complete cessation of crack growth occurred for applied potentials of -1100 mV_{SCE}.

A similar study, was completed on AA5456-H116 in 0.6 M NaCl with a high NAMLT value (65 mg/cm^2). The results showed no crack growth at applied potentials of -1000 mV_{SCE} [5]. The question then remains why this occurred in a similar material system but not for Alloy 1 (with similar amounts of beta phase coverage on the grain boundaries). One important difference to note between the two studies is the loading rate at which the experiments were conducted. In the study by McMahon *et al.,* the loading rate (dK/dt) of each experiment was 0.25 MPa√m/hr, while dK/dt for this study was 1.0 MPa√m/hr. It has been shown by Harris *et al.* that the loading rate AA5456-H116 can significantly impact the crack growth rate at applied potentials below -830 mV_{SCE} [39]. The authors found a 10 fold increase in crack growth rate when increasing the dK/dt from 0 to 2.0 MPa√m/hr for AA5456-H116 in 0.6 M NaCl with an applied potential of -900 mV_{SCE}. The argument Harris makes is the transition from stress-controlled fracture to strain-controlled fracture process at less severe environmental conditions, noting that there is a direct link between crack propagation and the loading rate in a strain-controlled fracture process. Therefore, it

can be reasoned in this instance that crack growth rate increases for increased dK/dt despite other environmental conditions that can allow for crack growth retardation.

The objective of this chapter was to observe the applied cathodic potential dependence of Alloy 1 in 0.6 M NaCl, as has been studied previously for other Al-Mg systems [5]. Following the logic of this work, it was discovered that Alloy 1 has the same applied potential dependence of the studied AA5xxx series. Specifically, at potentials cathodic to the alpha matrix, IGSCC susceptibility is decreased. In the previous work, applied potentials at or below the β breakdown potential, the Al-Mg alloys do not exhibit IGSCC behavior. Since this is not the case with Alloy 1, a possible explanation could be the role of the loading rate on the observed IGSCC susceptibility. Although, it is noted that Alloy 1 does have significant decreases in IGSCC susceptibility at applied potentials at and below the β breakdown potential, with eventual cessation of crack growth at an applied potential of -1100 mV_{SCE}. This work highlights the operative mechanism of crack growth to be consistent with other Al-Mg alloys as anodic dissolution enabled hydrogen embrittlement. This realization for Alloy 1 is crucial from an engineering standpoint for the development of mitigation strategies, such as metal rich coatings that have been shown to decrease IGSCC susceptibility of other Al-Mg alloys [40].

3.5 Conclusions

From the work presented some notable conclusions are obtained:

1. Crack growth rates of Alloy 1 exposed to 0.6 M NaCl are decreased with increasing applied cathodic potential (i.e. more negative) because of the decrease in an aggressive crack tip environment at potentials below the alpha and beta breakdown potentials.
2. Crack propagation of Alloy 1 is stopped entirely at an applied potential of -1100 mV_{SCE} in 0.6 M NaCl because of the cessation of anodic dissolution of beta phase which is the first step in the crack propagation mechanism for Al-Mg alloys.

Future work should include a loading rate study on the effectiveness of cathodic applied potentials to determine if there is a sensitivity that exists for this alloy. It would also be worth conducting experiments at static loading conditions to verify the crack growth condition for in-service materials and the efficacy of cathodic applied potential to stop crack growth.

References

[1] G.M. Scamans, N.J.H. Holroyd, C.D.S. Tuck, THE ROLE OF MAGNESIUM SEGREGATION IN THE INTERGRANULAR STRESS CORROSION CRACKING OF ALUMINIUM ALLOYS, 1987.

[2] Standard Test Method for Determining the Susceptibility to Intergranular Corrosion of 5XXX Series Aluminum Alloys by Mass Loss After Exposure to Nitric Acid (NAMLT Test) 1, (n.d.). https://doi.org/10.1520/G0067-18.

[3] M.E. McMahon, R.L. Haines, P.J. Steiner, J.M. Schulte, S.E. Fakler, J.T. Burns, Beta phase distribution in Al-Mg alloys of varying composition and temper, Corros Sci 169 (2020). https://doi.org/10.1016/j.corsci.2020.108618.

[4] R.H. Jones, D.R. Baer, M.J. Danielson, J.S. Vetrano, Role of Mg in the Stress Corrosion Cracking of and Al-Mg Alloy, Metallurgical and Materials Transactions A 32A (2001) 1699–1711.

[5] M.E. McMahon, J.R. Scully, J.T. Burns, Mitigation of Intergranular Stress Corrosion Cracking in Al–Mg by Electrochemical Potential Control, JOM 69 (2017) 1389–1397. https://doi.org/10.1007/s11837-017-2362-2.

[6] P.J. Steiner, Z.D. Harris, C. Vicente Moraes, R.G. Kelly, J.T. Burns, Investigation of IG-SCC Growth Kinetics in Al-Mg Alloys in Thin Film Environments, Corrosion 77 (2021) 838–852. https://doi.org/10.5006/3833.

[7] M.E. McMahon, P.J. Steiner, A.B. Lass, J.T. Burns, The effect of loading orientation on the stress corrosion cracking of Al-Mg alloys, Corrosion 73 (2017) 713–723. https://doi.org/10.5006/2343.

[8] P.J. Steiner, Z.D. Harris, J.T. Burns, Effect of Chloride Concentration on the Environment-Assisted Cracking Behavior of an Al-Mg Alloy in Atmospheric Environments, Corrosion 79 (2023) 1223–1233. https://doi.org/10.5006/4279.

[9] P.J. Steiner, J.T. Burns, Mechanistic studies of intergranular stress corrosion cracking in Al-Mg alloys under atmospheric exposure conditions, Corrosion 74 (2018) 1117–1131. https://doi.org/10.5006/2853.

[10] M. Pourbaix, Atlas of Electrochemical Equilibria in-Aqueous Solutions, n.d.

[11] M.E. McMahon, Z.D. Harris, J.R. Scully, J.T. Burns, The effect of electrode potential on stress corrosion cracking in highly sensitized Al–Mg alloys, Materials Science and Engineering: A 767 (2019). https://doi.org/10.1016/j.msea.2019.138399.

[12] Standard Practice for Operating Salt Spray (Fog) Apparatus 1, (n.d.). https://doi.org/10.1520/B0117-19.

[13] D. Scotto D'Antuono, J. Gaies, W. Golumbfskie, M.L. Taheri, Direct measurement of the effect of cold rolling on β phase precipitation kinetics in 5xxx series aluminum alloys, Acta Mater 123 (2017) 264–271. https://doi.org/10.1016/j.actamat.2016.10.060.

[14] R. Zhang, R.K. Gupta, C.H.J. Davies, A.M. Hodge, M. Tort, K. Xia, N. Birbilis, The influence of grain size and grain orientation on sensitization in AA5083, in: Corrosion, 2016. https://doi.org/10.5006/1703.

[15] J.G. Kaufman, Stress-Corrosion Cracking of Aluminum Alloys, in: Properties and Selection of Aluminum Alloys, ASM International, 2019: pp. 79–95. https://doi.org/10.31399/asm.hb.v02b.a0006545.

[16] D. Scotto D'Antuono, J. Gaies, W. Golumbfskie, M.L. Taheri, Grain boundary misorientation dependence of β phase precipitation in an Al-Mg alloy, Scr Mater 76 (2014) 81–84. https://doi.org/10.1016/j.scriptamat.2014.01.003.

[17] Y. Zhao, M.N. Polyakov, M. Mecklenburg, M.E. Kassner, A.M. Hodge, The role of grain boundary plane orientation in the β phase precipitation of an Al-Mg alloy, Scr Mater 89 (2014) 49–52. https://doi.org/10.1016/j.scriptamat.2014.07.003.

[18] X. Sauvage, N. Enikeev, R. Valiev, Y. Nasedkina, M. Murashkin, Atomic-scale analysis of the segregation and precipitation mechanisms in a severely deformed Al-Mg alloy, Acta Mater 72 (2014) 125–136. https://doi.org/10.1016/j.actamat.2014.03.033.

[19] F. Qin, C. Yang, H. Qi, C. Liu, H. Qi, Grain Size, Precipitation Behavior, and Mechanical Properties through the Thickness of Al-Mg-Si Aluminum Alloy Rings Produced by Compact Cast-Rolling Compound Forming, J Mater Eng Perform 31 (2022) 2329–2340. https://doi.org/10.1007/s11665-021-06326-7.

[20] D.L. Foley, A.C. Leff, A.C. Lang, M.L. Taheri, Evolution of β-phase precipitates in an aluminum-magnesium alloy at the nanoscale, Acta Mater 185 (2020) 279–286. https://doi.org/10.1016/j.actamat.2019.10.024.

[21] M. Lyn, C. Lim, Intergranular Corrosion Propagation in Sensitized Al-Mg Alloys, 2016.

[22] J.H. Ai, M.L.C. Lim, J.R. Scully, Effective hydrogen diffusion in aluminum alloy 5083-H131 as a function of orientation and degree of sensitization, Corrosion 69 (2013) 1225–1239. https://doi.org/10.5006/0987.

[23] J. Desai Choundraj, J. Kacher, Influence of misorientation angle and local dislocation density on β-phase distribution in Al 5xxx alloys, Sci Rep 12 (2022). https://doi.org/10.1038/s41598-022-05948-8.

[24] Designation: E112 − 13 Standard Test Methods for Determining Average Grain Size 1, (n.d.). https://doi.org/10.1520/E0112-13R21.

[25] Standard Test Method for Linear-Elastic Plane-Strain Fracture Toughness of Metallic Materials 1, (n.d.). https://doi.org/10.1520/E0399-22.

[26] R.P. Gangloff, D.C. Slavik, R.S. Piascik, R.H. Van Stone, Direct Current Electrical Potential Measurement of the Growth of Small Cracks, American Society for Testing and Materials (1992) 116–168.

[27] Standard Test Method for Measurement of Fatigue Crack Growth Rates 1, (n.d.). https://doi.org/10.1520/E0647-23A.

[28] Z.D. Harris, J.T. Burns, On the loading rate dependence of environment-assisted cracking in sensitized AA5456-H116 exposed to marine environments, Corros Sci 201 (2022). https://doi.org/10.1016/j.corsci.2022.110267.

[29] R.P. Gangloff, H.M. Ha, J.T. Burns, J.R. Scully, Measurement and modeling of hydrogen environment-assisted cracking in monel K-500, Metall Mater Trans A Phys Metall Mater Sci 45 (2014) 3814–3834. https://doi.org/10.1007/s11661-014-2324-z.

[30] J.X. Zhang, M. Ma, W.C. Liu, Effect of initial grain size on the recrystallization and recrystallization texture of cold-rolled AA 5182 aluminum alloy, Materials Science and Engineering: A 690 (2017) 233–243. https://doi.org/10.1016/j.msea.2017.03.015.

[31] P. Ebenberger, P.J. Uggowitzer, B. Gerold, S. Pogatscher, Effect of compositional and processing variations in new 5182-type AlMgMn alloys on mechanical properties and deformation surface quality, Materials 12 (2019). https://doi.org/10.3390/ma12101645.

[32] W. Gao, D. Wang, M. Seifi, J.J. Lewandowski, Anisotropy of corrosion and environmental cracking in AA5083-H128 Al-Mg alloy, Materials Science and Engineering: A 730 (2018) 367–379. https://doi.org/10.1016/j.msea.2018.06.021.

[33] J.L. Searles, P.I. Gouma, R.G. Buchheit, Stress Corrosion Cracking of Sensitized AA5083 (Al-4.5Mg-1.0Mn), n.d.

[34] A.J. Davenport, Y. Yuan, R. Ambat, B.J. Connolly, M. Strangwood, A. Afseth, G.M. Scamans, Intergranular Corrosion and Stress Corrosion Cracking of Sensitised AA5182, Materials Science Forum 519–521 (2006) 641–646. https://doi.org/10.4028/www.scientific.net/msf.519-521.641.

[35] C.: Yuan, Yudie, Localised corrosion and stress cracking of aluminium-magnesium alloys, University of Birmingham, 2005.

[36] R. Zhang, S.P. Knight, R.L. Holtz, R. Goswami, C.H.J. Davies, N. Birbilis, A survey of sensitization in 5xxx series aluminum alloys, in: Corrosion, National Assoc. of Corrosion Engineers International, 2016: pp. 144–159. https://doi.org/10.5006/1787.

[37] C.B. Crane, R.P. Gangloff, Stress corrosion cracking of Al-Mg alloy 5083 sensitized at low temperature, in: Corrosion, National Assoc. of Corrosion Engineers International, 2016: pp. 221–241. https://doi.org/10.5006/1766.

[38] M.E. McMahon, P.J. Steiner, A.B. Lass, J.T. Burns, The effect of temper and composition on the stress corrosion cracking of Al-Mg alloys, Corrosion 73 (2017) 347–361. https://doi.org/10.5006/2317.

[39] Z.D. Harris, J.T. Burns, On the loading rate dependence of environment-assisted cracking in sensitized AA5456-H116 exposed to marine environments, Corros Sci 201 (2022). https://doi.org/10.1016/j.corsci.2022.110267.

[40] M.E. McMahon, J.R. Scully, J.T. Burns, Mitigation of Intergranular Cracking in Al-Mg Alloys via Zn-Based Electrode Potential Control in Sodium Chloride Solution, Corrosion 75 (2019) 911–928. https://doi.org/10.5006/3185.

[41] R. Sanders, J. Staley, A History of Wrought Aluminum Alloys and Applications, in: Properties and Selection of Aluminum Alloys, ASM International, 2019: pp. 157–201. https://doi.org/10.31399/asm.hb.v02b.a0006516.

[42] N. Brown, P. Kramer, F. Friedersdorf, M. Schindelholz, J. Siegel, Environmentally assisted cracking measurements in structural aluminum alloys under accelerated test conditions, Corrosion 72 (2016) 1351–1362. https://doi.org/10.5006/2085.

[43] C. Liu, J. Srinivasan, R.G. Kelly, Editors' Choice—Electrolyte Film Thickness Effects on the Cathodic Current Availability in a Galvanic Couple, J Electrochem Soc 164 (2017) C845–C855. https://doi.org/10.1149/2.1641713jes.

[44] F. Ge, L. Zhang, H. Tian, M. Yu, J. Liang, X. Wang, Stress Corrosion Cracking Behavior of 2024 and 7075 High-Strength Aluminum Alloys in a Simulated Marine Atmosphere Contaminated with SO2, J Mater Eng Perform 29 (2020) 410–422. https://doi.org/10.1007/s11665-019-04537-7.

[45] M. WANG, L. WANG, K. PANG, Y. LIU, Y. WANG, Z. CUI, Understanding stress corrosion cracking behavior of 7085-T7651 aluminum alloy in polluted atmosphere, Chinese Journal of Aeronautics 36 (2023) 408–421. https://doi.org/10.1016/j.cja.2023.06.011.

[46] E.M. Arnold, J.J. Schubbe, P.J. Moran, R.A. Bayles, Comparison of SCC thresholds and environmentally assisted cracking in 7050-T7451 aluminum plate, J Mater Eng Perform 21 (2012) 2480–2486. https://doi.org/10.1007/s11665-012-0204-5.

[47] PENAIR ® M5571, n.d.

[48] G.A. Truesdale, A.L. Downing, Solubility of Oxygen in Water, Nature 173 (1954) 1236.

[49] I.W. Huang, B.L. Hurley, F. Yang, R.G. Buchheit, Dependence on Temperature, pH, and Cl- in the Uniform Corrosion of Aluminum Alloys 2024-T3, 6061-T6, and 7075-T6, Electrochim Acta 199 (2016) 242–253. https://doi.org/10.1016/j.electacta.2016.03.125.

[50] C.N. Panagopoulos, E. Georgiou, K.I. Giannakopoulos, P.G. Orfanos, Effect of ph on stress corrosion cracking of 6082 al alloy, Metals (Basel) 8 (2018). https://doi.org/10.3390/met8080578.

[51] W.-T. Tsai, J.-B. Duh, J.-J. Yeh, J.-T. Lee, Y.-C. Chang"', Effect of pH on Stress Corrosion Cracking of 7050-T7451 Aluminum Alloy in 3.5 wt% NaCl Solution *, 1990. http://meridian.allenpress.com/corrosion/article-pdf/46/6/444/1530787/1_3585130.pdf.

[52] Z. Dan, I. Muto, N. Hara, Effects of environmental factors on atmospheric corrosion of aluminium and its alloys under constant dew point conditions, Corros Sci 57 (2012) 22–29. https://doi.org/10.1016/j.corsci.2011.12.038.

[53] T.F. Cui, D.X. Liu, P.A. Shi, J.J. Liu, Y.H. Yi, H.L. Zhou, Effect of NaCl concentration, pH value and tensile stress on the galvanic corrosion behavior of 5050 aluminum alloy, Materials and Corrosion 67 (2016) 72–83. https://doi.org/10.1002/maco.201408189.

[54] E. Bumiller, INTERGRANULAR CORROSION IN AA5XXX ALUMINUM ALLOYS WITH DISCONTINUOUS PRECIPITATION AT THE GRAIN BOUNDARIES A Dissertation Presented to, 2011.

[55] J.A. Lyndon, R.K. Gupta, M.A. Gibson, N. Birbilis, Electrochemical behaviour of the β-phase intermetallic (Mg2Al3) as a function of pH as relevant to corrosion of aluminium-magnesium alloys, Corros Sci 70 (2013) 290–293. https://doi.org/10.1016/j.corsci.2012.12.022.

[56] B. Zaid, D. Saidi, A. Benzaid, S. Hadji, Effects of pH and chloride concentration on pitting corrosion of AA6061 aluminum alloy, Corros Sci 50 (2008) 1841–1847. https://doi.org/10.1016/j.corsci.2008.03.006.

[57] C.B. Crane, R.G. Kelly, R.P. Gangloff, Crack chemistry control of intergranular stress corrosion cracking in sensitized Al-Mg, in: Corrosion, National Assoc. of Corrosion Engineers International, 2016: pp. 242–263. https://doi.org/10.5006/1852.

Chapter 4: Effect of Atmospheric Environments on the Crack Growth Kinetics of Alloy 1

4.1 Introduction

The 5xxx series aluminum alloys (AA) are used in a wide variety of industries including automobile, naval, aerospace, and military [41]. All of these applications leave AA5xxx vulnerable to atmospheric environments which can allow for deposition of aqueous-chloride containing solutions. This type of environment has been known to cause intergranular corrosion (IGC) and, in some cases, intergranular stress corrosion cracking (IGSCC) [42]. The majority of environment-assisted cracking (EAC) experiments to test the IGSCC susceptibility have been in full immersion conditions, where the sample is fully submersed in solution. Although, this condition may not accurately represent environmental conditions pertinent to in-service engineering applications, where atmospheric environments will result in limited solution geometries/volumes. Therefore, it has been of growing interest to study the effect of a more realistic atmospheric environmental condition on the IGSCC susceptibility of AA5xxx series [6,8,9,42].

The most obvious difference in full immersion testing and atmospheric testing is the amount of solution exposed to the material, which is referred to as the electrolyte geometry. In a full immersion setting, the entire surface and at least 1 mm above the surface is covered with electrolyte. In atmospheric conditions, there are many difference situations that can arise in terms of the continuity and thickness of the water layer deposited on the material that depend on the specific exposure conditions, such as temperature and humidity. The difference in electrolyte geometry is paramount for corrosion of the material because of the effect of water layer thickness on the available cathodic current necessary to drive corrosion processes [6,43]. It has been shown that going from full immersion to thin film electrolytes increases the ohmic drop and therefore limits the available cathodic current [6,43]. In the context of IGSCC related crack growth of AA5xxx series, it was further studied that thin film electrolyte exposure increased the ohmic drop of the cathodic area which in turn limited the available cathodic current and subsequently decreased overall IGSCC susceptibility [6,9]. This argument was analyzed in the framework of the proposed mechanism, anodic dissolution enabled hydrogen embrittlement, for IGSCC crack growth in AA5xxx series, which relies on the anodic dissolution of the beta phase. In the case where the cathodic current is limited by ohmic drop within the thin film electrolyte, the anodic dissolution is also limited. In line with the mechanistic understanding, this will also limit the following hydrolysis and chloride ingress, therefore creating a less aggressive crack tip chemistry, with less H production and embrittlement processes to effectively reduce overall crack growth rates. The conclusion of these studies was that

decreasing water layer thickness gave decreasing IGSCC susceptibility and the available cathodic current was affected most by the solution ohmic resistance [6,9], however, changing the water layer thickness can also affect the oxygen diffusion kinetics, which would have an adverse effect on the IGSCC susceptibility. These affects have not been observed in the available literature of the AA5xxx series. It is therefore necessary to capture and quantify this behavior to inform engineering component lifetime predictions and/or inspection intervals for in-service components.

Not only is the electrolyte geometry of significance, but the electrolyte composition is also important to consider because of the specific crack tip chemistry that develops. There are a wide variety of solutions that can be exposed to in-service aluminum alloys and not all of them have high chloride concentrations (0.6 M NaCl) with slightly acidic/near neutral pH (~6), as was used in the studies mentioned previously [6,8,9,43]. Ge *et al.* studied the effect of atmospheric environments on the SCC susceptibility of AA2024-T351 and AA7075-T651 with increasing HSO_3^- using slow strain rate tests (SSRT), and found increasing susceptibility of both alloys with increasing acid concentration [44]. In a similar study, Wang *et al.* observed the same trend for SSRT of AA7085-T7651 after exposure to a simulated polluted atmospheric environment in the form of a thin film electrolyte [45]. In both studies, the solutions with added HSO_3^- had greater SCC susceptibility than the 3.5% NaCl exposure, showing the importance of solution pH and increasing susceptibilities for more acidic solutions. On the other hand, Amold *et al*. sought to determine the SCC susceptibility of AA7050-T7451 to a more basic cleaning solution and used a wicking based approach – exposing the notch to only one drop of solution periodically [46]. The pH of the cleaning solution was approximately 9 [47], but the results still showed SCC susceptibility to this solution in the absence of chloride and slightly basic solution, but was less susceptible than exposure to 3.5% NaCl [46]. These studies were conducted on other aluminum alloy systems, but it is relevant to study the behavior of the AA5xxx series in the same way because of their wide use in different engineering applications [41]. The solution pH and the chloride concentration are pertinent to the relevant chemistries that develop at the crack tip and a wide variety of solutions need to be assessed in light of the recent advancements on the anodic dissolution enabled hydrogen embrittlement mechanism.

The number of studies investigating the effect of atmospheric environments on AA5xxx are limited, and focus on slightly acidic, high chloride containing solutions [6,8,9]. It is known that low chloride containing, slightly basic solutions can also show SCC susceptibility and so, this study aims to determine the distinct IGSCC susceptibility of Alloy 1 (an Al-Mg alloy) exposed to a low-chloride containing, slightly basic atmospheric environments. Moreover, changing the amount of solution exposure to the bulk surfaces of these alloys is tested using linear elastic fracture mechanics (LEFM) based approach. The

objective of this chapter is to capture the IGSCC behavior of Alloy 1 exposed to a basic pH, low chloride containing solution (Solution 1) in atmospheric environments. Specifically, crack growth kinetics of Alloy 1 are obtained for a misting and wicking condition of Solution 1, and are compared to the crack growth kinetics obtained in full immersion of Solution 1. These results are analyzed in the context of the anodic dissolution-hydrogen embrittlement mechanism.

4.2 Materials and Methods

4.2.1 Sample Design

Single edge notch samples are machined from the Alloy 1 sheet in the as received condition. The samples were oriented such that the tensile loading was parallel to the T direction (transverse, normal to rolling direction), and the Mode 1 cracking plane was along in the L direction (rolling direction), shorted as the T-L orientation. The average thickness of the specimens were 3.33 mm; the specimen width was 25.4 mm and had a total length of 177.8 mm. An electrical discharge machined (EDM) notch was placed at the center of specimen length, with a depth equaling 5.7 mm.

4.2.2 Linear Elastic Fracture Mechanics (LEFM) testing

Stress corrosion susceptibility of Alloy 1 was probed using Linear Elastic Fracture Mechanics (LEFM) approach. The SENT specimens were fatigue precracked in lab air to 6.0 mm with a final stress intensity (K) of 2 MPa√m. Slow rising displacement experiments following the precrack were controlled via K and conducted at a rate of 1 MPa√m/hr. Direct current potential difference (dcPD) was used to monitor crack growth, and has a resolution limit of 0.5 um. The details of this method can be read elsewhere [26].

Full immersion testing involved an acrylic environmental cell placed around the sample following the fatigue precrack and filled with 200 mL of Solution 1. The exact constituents of Solution 1 are proprietary, however the chloride content is 10 mg/L and has a pH of 7.9. A reservoir totaling 2 L of the same electrolyte was continuously flowed at a rate of 100 mL/min at ambient temperature. The sample was fully immersed, with 25.4 mm length of exposure around the EDM notch (with the notch being at the center). A three electrode system was utilized for potentiostatic control. An insulated copper wire welded to the SENT specimen was used as the working electrode, a saturated calomel electrode (SCE) as the reference electrode, and Pt mesh as the counter electrode. The environmental setup is shown in Figure 4.1 for clarity. A Biologic PG-581 handheld potentiostat was used to measure open circuit potential (OCP) measurement before the start of the experiment, while the SENT specimen was loaded in tension (1 kN

of force), and for potentiostatic hold of -700 mV_{SCE}. After establishing stable OCP after approximately 1 hour, samples were loaded at a loading rate (dK/dt) of 1 MPa√m/hr.

The **misting condition** utilized two 80° conical fine-spray misting nozzles, which had an inner diameter of 0.35 mm, directed at the SENT specimen. An acrylic cell was placed around the sample and the nozzles were able to continuously mist onto the sample unobstructed. Solution 1 was able to mist at a flow rate of approximately 40 mL/min. The solution was able to drain from the acrylic cell and circulate in a 2 L reservoir of the same solution. To probe the influence of oxygen availability to the crack tip on the cracking kinetics, a second type of misting experiment was conducted using the same parameters outlined above, but the environmental cell was purged with nitrogen throughout the experiment. Before the misting of Solution 1 into the cell, nitrogen filled the chamber and the humidity inside the chamber was ensured to be below 7%, to ensure that the ambient air was purged from the chamber. In both cases the sample was lacquered into the cell with the same amount of exposure as the full immersion condition. To gather electrochemical data, a thin Ag/AgCl reference electrode was placed close to the specimen, but placed in such a way where the electrode was not touching the specimen but was able to encounter the same solution exposed to the working electrode. A copper wire welded to Alloy 1 was used as the working electrode and a Biologic PG-581 handheld potentiostat was able to gather OCP measurements throughout the K rise experiment (dK/dt = 1 MPa√m/hr). The environmental setup can be viewed in Figure 4.2.

The environmental condition with the least amount of solution volume exposure to the specimen is known as the **wicking condition**. This is achieved by running a wetted fiberglass string "wicking" solution directly into the crack. The fiberglass wick was saturated in Solution 1 and placed into the EDM notch prior to mechanical testing from a 100 mL reservoir. The flow rate was not explicitly measured, but was suggested to be 1 mL/hr [9]. Verification by physical inspection of the wick as being wet on both sides of the notch was completed every 2 hours for the first 8 hours of the experiment, and then every 5 hours for the remainder of the test. The same mechanical loading protocol as outlined above was also completed for this experiment. The wicking experimental condition can be seen in Figure 4.3.

Following all of the K rise experiment, solution was removed from the cell and the SENT specimen were post-test fatigued to failure. One half of the specimen was sonicated in methanol and the fracture surface was imaged using FEG Quanta 650 SEM. Secondary electron images were acquired using the Everhart-Thornley detector (ETD) at a spot size of 3.0 and an accelerating voltage of 10.0 kV.

As has been reported in Chapters 2 and 3 previously, the data analysis of the LEFM results followed best practices for correcting the raw dcPD collected data and obtaining crack growth kinetics. The crack growth rates were calculated using steps similar to what is described in ASTM E647 [27].

Additionally, the resolution limit correction and shorting correction, which are known issues with dcPD data collection, were performed, as completed by [39] and [29].

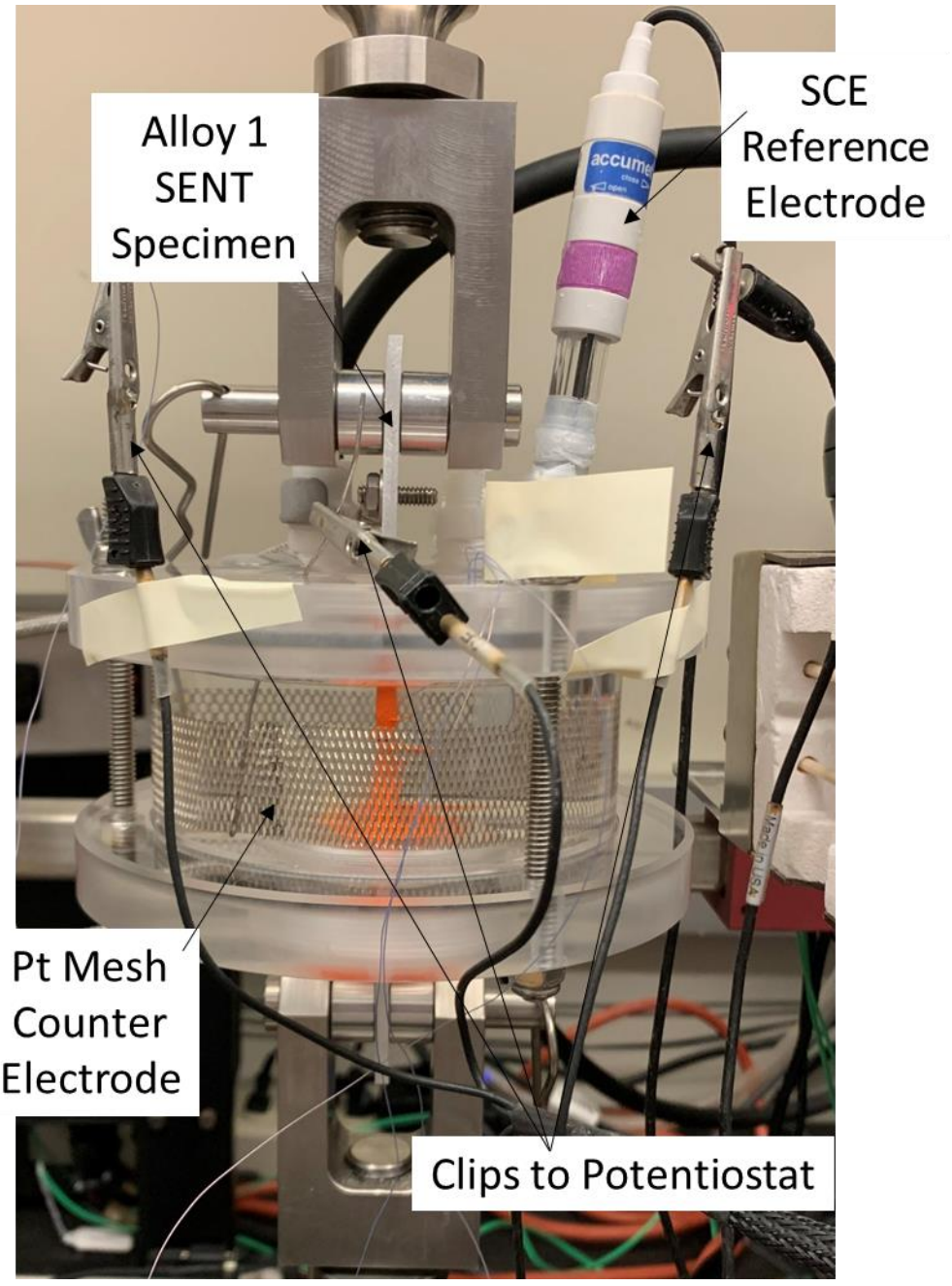

Figure 4.1: Full immersion environmental setup, showing the SENT specimen of Alloy 1 pulled in tension between two clevis grips on the MTS 810 servohydraulic load frame. The Pt mesh (counter electrode) is encased in the solution, as is the frit of the SCE electrode (not visible inside the cell, but the top is coming out of the cell, as indicated on the figure). The alligator clips connect the working electrode, RE, and CE to the potentiostat (as labeled on the figure).

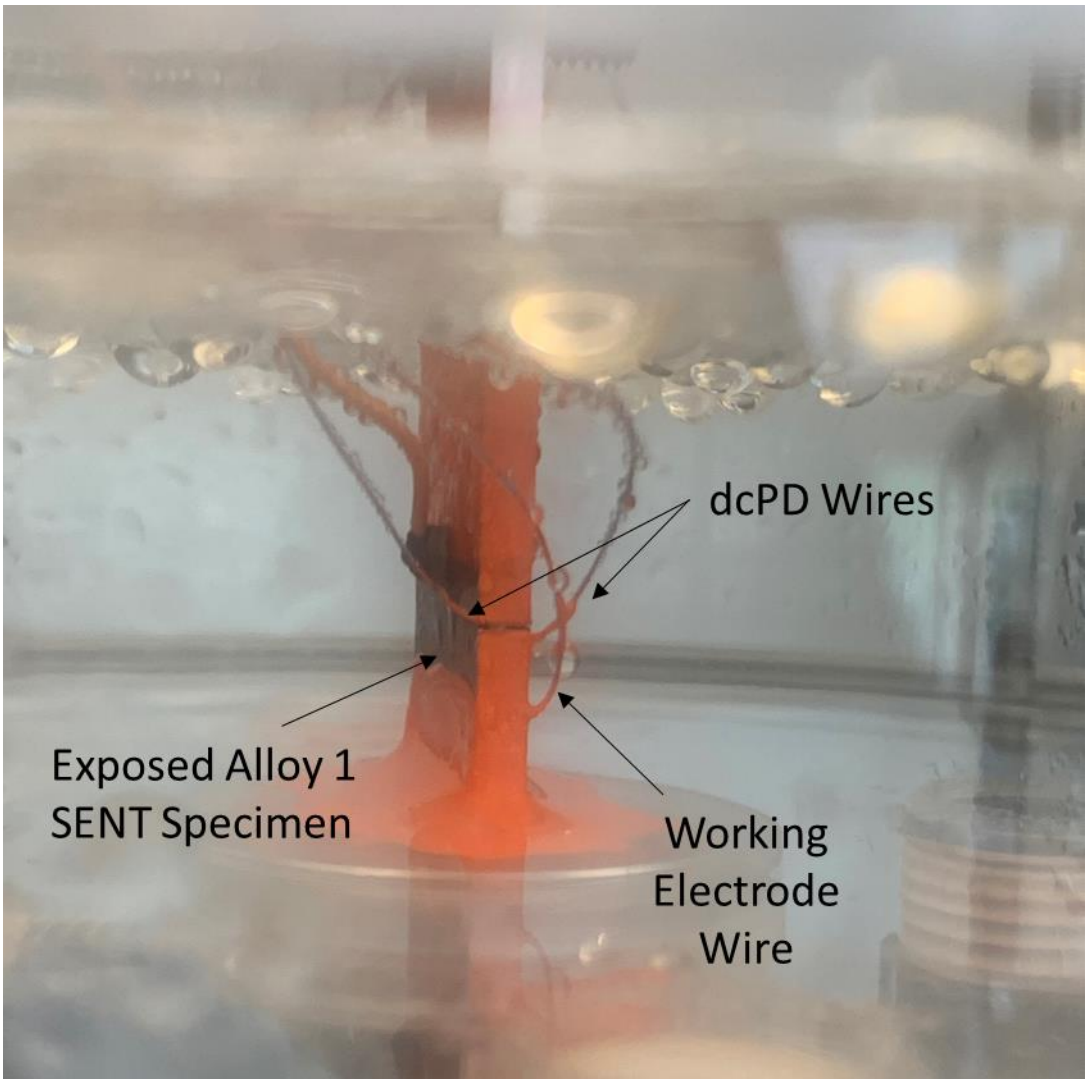

Figure 4.2: Alloy 1 SENT specimen exposed to the misting condition. This image was captured at the beginning of the misting experiment, and a continuous thin film has not yet developed. However, this image is meant to show the distinction of the misting condition from the other exposure conditions. Not imaged is the misting nozzles.

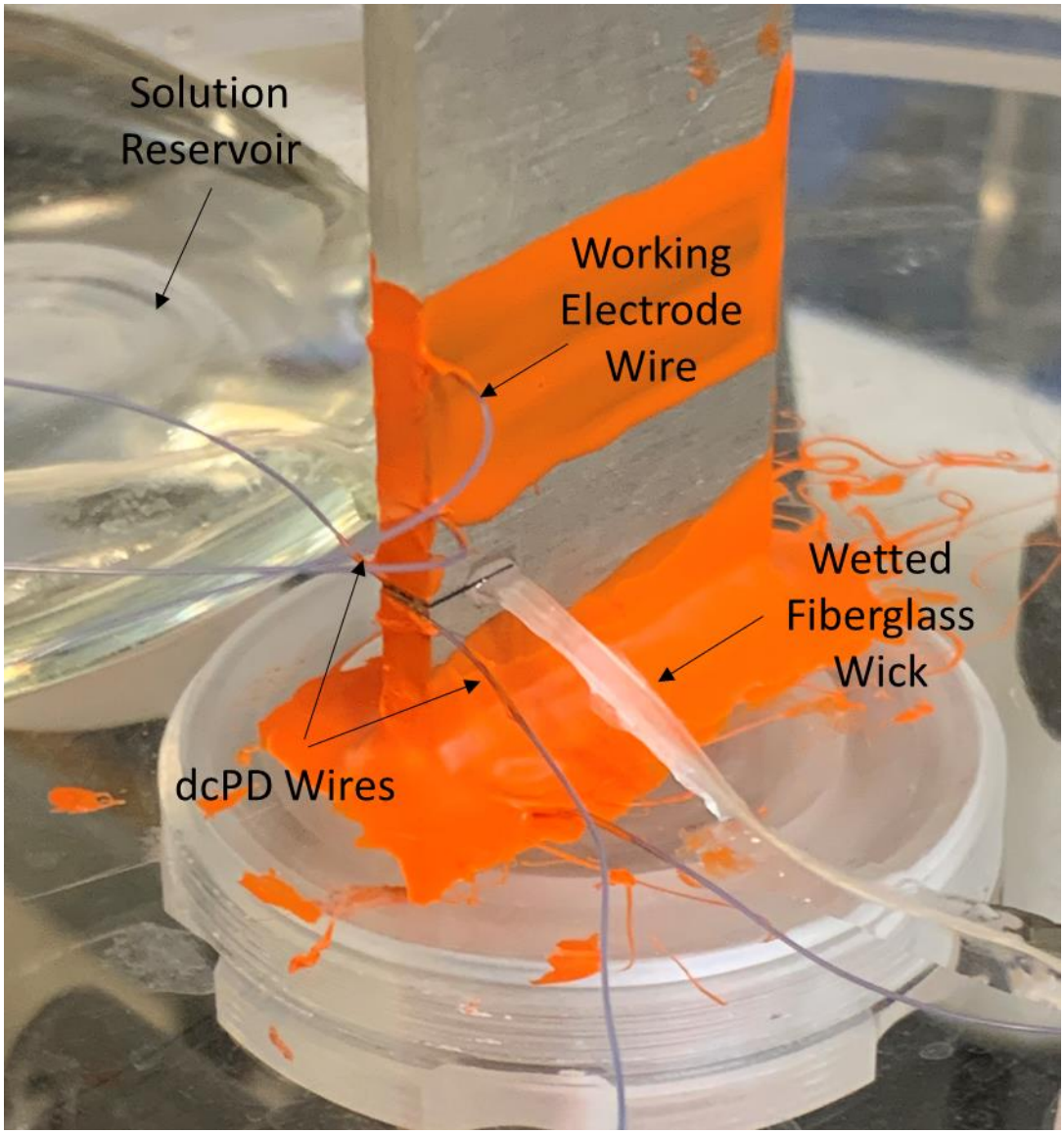

Figure 4.3: Alloy 1 SENT specimen in the wicking experimental condition. The fiberglass wick is wetted from the solution reservoir and fed through the EDM notch to simulate instances where solution is directly wicked into the crack tip.

4.2.3 Electrochemical Flat Cell Testing

Alloy 1 was used for electrochemical testing. Samples were cut, exposing at least 1 cm^2 area of the LT plane. Before electrochemical testing, the samples were polished to 1200 grit with deionized (DI) water. Pure beta phase (Al_3Mg_2) (the same material as was used in [5]) was mounted in epoxy and polished to 1200 grit with ethanol.

Shortly after polishing, the samples were placed in an electrochemical flat cell with a 1 cm^2 exposure area. A typical three electrode system was utilized for corrosion testing where the working

electrode was either Alloy 1 or Al_3Mg_2, the counter electrode was Pt mesh, and the reference electrode was a saturated calomel electrode (SCE). Each of these electrodes were connected via alligator clips to a Biologic VMP3 Potentiostat. Prior to obtaining corrosion kinetics, samples were exposed to Solution 1 for 60 minutes (Alloy 1) or 30 minutes (beta alloy) to obtain stable open circuit potential (OCP) conditions. Following the OCP hold, anodic or cathodic potentiodynamic scans were run at a rate of 0.167 mV_{SCE}/s. Anodic scans were started at OCP and the potential was increased at the scan rate until reaching +0.5 V_{SCE}. Cathodic scans were run in a similar fashion, starting at OCP and decreasing the potential at 0.167 mV/s until reaching a potential of –2.0 V_{SCE}. Note, cathodic polarization scans were only obtained for Alloy 1 in the different solutions because of the expected nobility of Alloy 1 compared to beta (add reference). During these experiments, the corrosion kinetics (i.e. corrosion current) were obtained as the potential was stepped. After the potentiodynamic scans were completed, samples were removed from the flat cell, rinsed with DI water and imaged using a Hirox RH-8800 optical microscope. Each anodic and cathodic polarization scan were run three times in each solution and the results show one representative curve of each.

4.3 Results

4.3.1 Polarization Curves of Alloy 1 and Al_3Mg_2

Polarization curves of Alloy 1 and Al_3Mg_2 in Solution 1 are shown in Figure 4.4. The OCP of Alloy 1 is approximately -0.70 V_{SCE}. There is a significant window of passivity compared to Alloy 1 exposed to 0.6 M NaCl (see chapter 3), with a breakdown potential of -0.34 V_{SCE}. Also observable from the figure is the OCP of Al_3Mg_2 nearing -1.0 V_{SCE}, and a breakdown potential of -0.45 V_{SCE}, which is also significantly higher than the breakdown potential of Al_3Mg_2 in 0.6 M NaCl (see chapter 3). It is important to note that the breakdown potential of alpha-Al matrix (Alloy 1) and Al_3Mg_2 are more positive than in chloride containing solutions, keeping in mind that Solution 1 has negligible chloride concentration (10 mg/L) compared to 0.6 M NaCl (36065 mg/L). Additionally, the pH differences are also noted: Solution 1 has a pH of 7.9, while 0.6 M NaCl has a pH of 6.0.

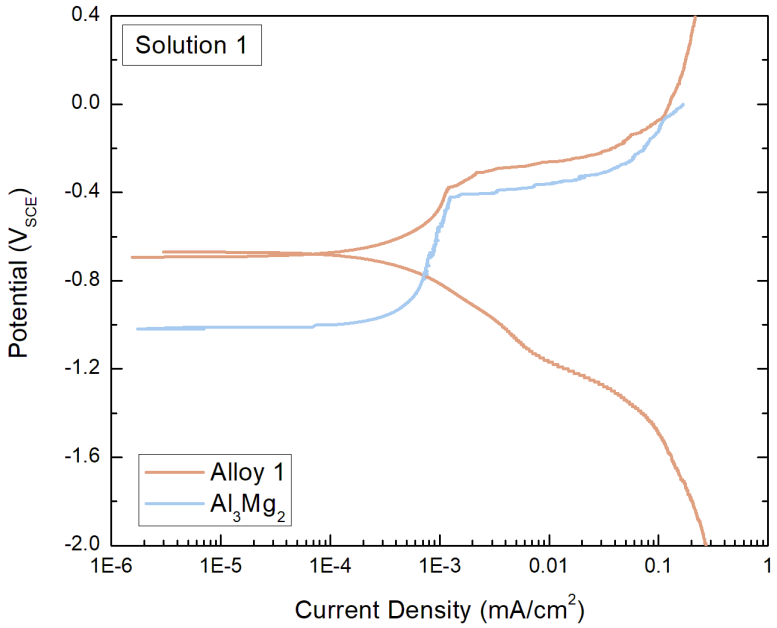

Figure 4.4: Anodic and cathodic polarization curves of Alloy 1 and anodic curve of beta phase in Solution 1 after 60 minutes (alloy 1) or 30 minutes (Al_3Mg_2) of exposure for OCP stabilization.

4.3.2 Crack Growth Kinetics of Alloy 1 with Different Environmental Exposures

LEFM test results of Alloy 1 exposed to Solution 1 in the full immersion condition revealed no intergranular crack growth, as verified by the SEM fractography in Figure 4.5. It should be noted that the applied potential at -700 mV_{SCE} for this experiment represent freely corroding conditions for Alloy 1 in Solution 1, but both Alloy 1 and Al_3Mg_2 are passive at this potential. Therefore, it would not be expected that crack growth could occur at this applied potential, as has been discussed in Chapter 3 (The effect of applied potential on the crack growth kinetics of Alloy 1).

However, when testing in the atmospheric conditions (misting and wicking), crack growth was observed in Solution 1, as seen in Figure 4.6. The K_{TH} of the wicking experiment was lower than the misting environment, suggesting greater IGSCC susceptibility in this condition, however there was a decreased crack growth rates below K=8 MPa√m for the wicking condition). After 8 MPa√m, the two atmospheric conditions have crack growth kinetics that are similar, most likely within the typical scatter associated with sample to sample variability). Interestingly, when the ambient air was removed in the misting

experiment by purging with nitrogen throughout the entirety of the experiment, there was again no IGSCC crack growth observed.

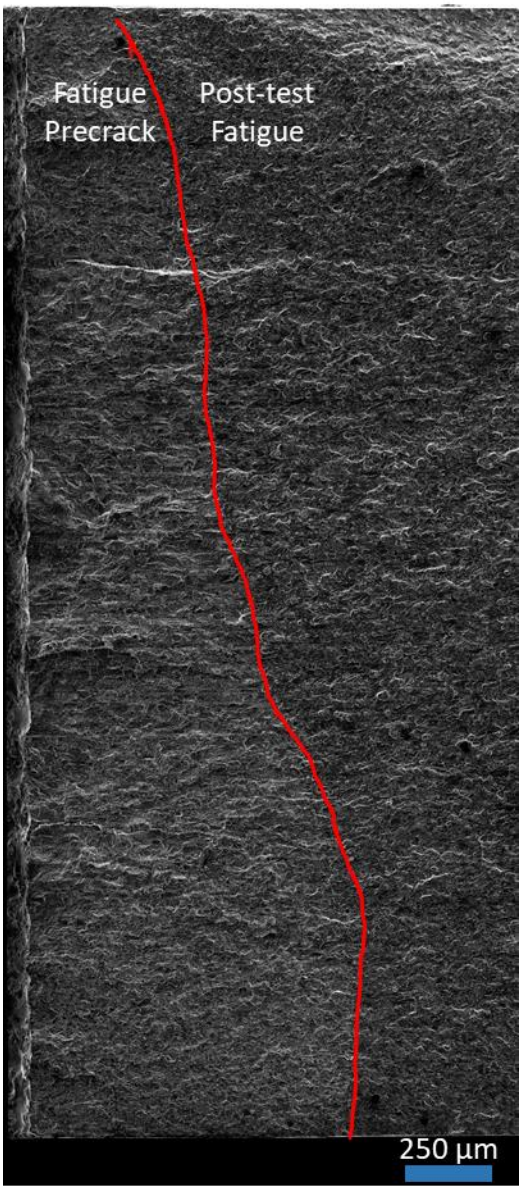

Figure 4.5: SEM fractography of Alloy 1 exposed to Solution 1 in full immersion with an applied potential of -700 mV_SCE. The red line separates the fatigue precracked region (to the left) and the post-test fatigue region (to the right), indicating that no intergranular fracture occurred during the EAC experiment.

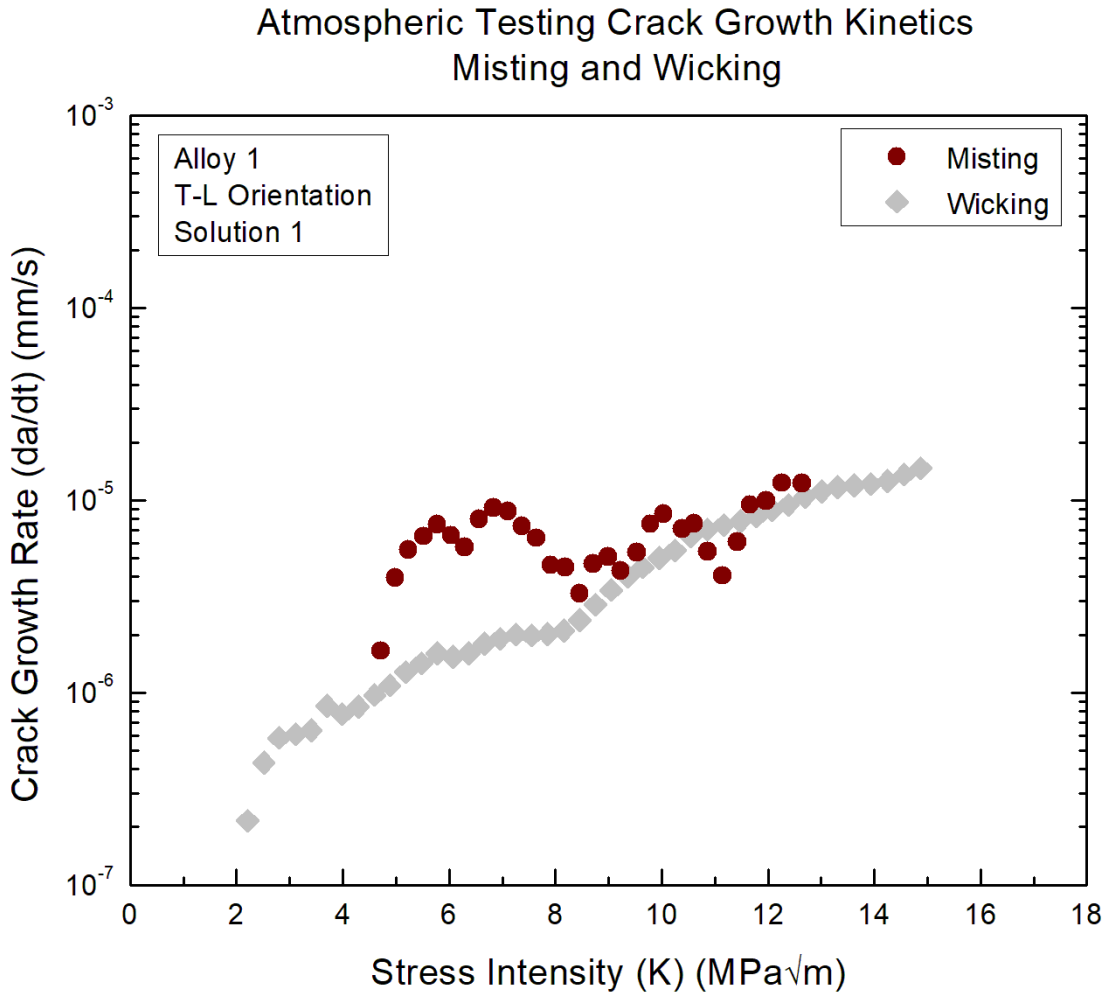

Figure 4.6: Crack growth rate vs. stress intensity of Alloy 1 exposed to misting and wicking of Solution 1.

4.4 Discussion

The key result that warrants discussion is that for exposure of Solution 1 (e.g. basic pH, low chloride environment) to Alloy 1, the atmospheric environments exhibit susceptibility whereas no cracking was observed in full immersion environment. Since the solution chemistry was constant the only variable was the electrolyte geometry. When the electrolyte geometry is reduced, the cathodic current necessary to facilitate anodic dissolution can be affected by the ohmic resistance or the oxygen diffusion kinetics. AA5xxx series exposed to atmospheric environments containing high chloride concentrated solutions (0.6 M NaCl and above) had increased solution resistance, or increased ohmic drop, as the water layer decreased effectively decreased the available cathodic current [6,8,9]. This decrease in cathodic

current decreased the IGSCC susceptibility because of the limitation of anodic dissolution of the beta phase, which has been discussed at the primary step in the mechanism for crack growth in AA5xxx series. Conversely, the results shown for Alloy 1 exposed to Solution 1 have increased IGSCC susceptibility for atmospheric environments compared to full immersion. As was mentioned, the available cathodic current could also be affected by the oxygen diffusion kinetics. In this scenario, we must recognize the dominating cathodic reaction as the oxygen reduction reaction (ORR), which is limited by the diffusion of oxygen in the electrolyte. In this diffusion limited regime, the diffusion limited-cathodic current density is given by

$$i = \frac{nFDC_b}{\delta}$$

Where i is the diffusion limited-cathodic current density, n is the number of electrons accepted in the cathodic reaction, F is Faraday's constant, D is the diffusion coefficient of oxygen in water, C_b is the solubility of oxygen in water, and δ is the diffusion distance. Changing the electrolyte geometry from full immersion to the atmospheric condition only decreases the diffusion layer distance, and all of the other variables in the above equation remain the same. Therefore, if the diffusion layer distance is decreased, the diffusion limited-cathodic current density must increase, by the equation above.

Alloy 1 operates under the same mechanism of crack growth as the other Al-Mg systems, as was found in Chapter 3, and thus will have IGSCC crack growth when exposed to a corrosive electrolyte (and sufficient stress) that will invoke anodic dissolution of the beta phase. Regardless of the amount of chloride present in the solution, it is clear from the results that the cathodic current is increased by enhancement of the oxygen transport through a decreased water layer thickness, as discussed above. As a result of cathodic current increases, the anodic dissolution is enhanced, promoting a more aggressive crack tip chemistry, more H production and subsequent embrittlement of the material ahead of the crack tip, all of which contribute to faster crack growth kinetics by the anodic dissolution enabled hydrogen embrittlement mechanism of Alloy 1. This argument can support the results of faster crack growth kinetics of Alloy 1 in atmospheric environments compared to the full immersion condition.

To confirm the hypothesis that the available cathodic current is controlled by the oxygen diffusion kinetics, the misting experiment purged with nitrogen was performed. The results showed that there was no crack growth during this experiment. Since the oxygen availability in the ambient environment was low, the only source of oxygen to support the cathodic reaction was that which was in the electrolyte, however, water has a low solubility of oxygen (about 8 ppm at room temperature) [48]. Therefore, all of the available oxygen to support the ORR would be used rather quickly, and cathodic reactions would cease, as would the anodic reactions, and all of the other mechanistic processes. This is confirmation that

oxygen availability is likely the reason that susceptibility was observed in the misting/wicking environments but was not observed in the full immersion environment.

In comparing the wicking and misting of Solution 1 to Alloy 1, the results did show a decrease in threshold stress intensity for the wicking condition compared to the wicking condition. However, after a stress intensity of 9 MPaVm, the stage two crack growth rates begin to converge. It is not known why these differences exist, and future work could include determining the root cause of these changes in crack growth rate. Another unanswered question that remains for this chapter is the why the available cathodic current is affected most by the oxygen transport and not the ohmic drop as was found in other Al-Mg systems [6,8,9]. Future work could look into whether the conductivity of Solution 1 would allow for enhanced solubility and diffusivity of oxygen, as the conductivity will give insights to the ability of electrons to flow through the solution.

Overall, the objective of gathering crack growth kinetics of Alloy 1 exposed to Solution 1 in atmospheric environments compared to full immersion was completed. It should be noted that for this specific solution chemistry, the crack growth kinetics of Alloy 1 were increased in atmospheric environments because of increased oxygen transport due to a thinner diffusion distance. These results were discussed in light of the anodic dissolution enabled hydrogen embrittlement mechanism which was found to be working in Alloy 1. More work is needed to identify why different solutions would change the operative mechanism for controlling the available cathodic current.

4.5 Conclusions

From the study, the effect of atmospheric environments on EAC crack growth kinetics of Alloy 1 exposed to a low chloride containing, basic pH solution was investigated. The following conclusions can be made from the results and discussions above:

1. Full immersion exposure of Alloy 1 to Solution 1 showed the least EAC susceptibility, with no crack growth.
2. Atmospheric conditions (misting and wicking) had increased EAC susceptibility than the full immersion condition, which was attributed to the increased diffusion limited-cathodic current density from increased oxygen transport which occurred by decreased diffusion distance through the electrolyte.

3. The misting condition had slightly lower threshold stress intensity than the wicking condition, but the two atmospheric conditions had similar stage II crack growth rates which could be an indication of the importance of the low stress intensity loading range for this alloy.

References

[1] G.M. Scamans, N.J.H. Holroyd, C.D.S. Tuck, THE ROLE OF MAGNESIUM SEGREGATION IN THE INTERGRANULAR STRESS CORROSION CRACKING OF ALUMINIUM ALLOYS, 1987.

[2] Standard Test Method for Determining the Susceptibility to Intergranular Corrosion of 5XXX Series Aluminum Alloys by Mass Loss After Exposure to Nitric Acid (NAMLT Test) 1, (n.d.). https://doi.org/10.1520/G0067-18.

[3] M.E. McMahon, R.L. Haines, P.J. Steiner, J.M. Schulte, S.E. Fakler, J.T. Burns, Beta phase distribution in Al-Mg alloys of varying composition and temper, Corros Sci 169 (2020). https://doi.org/10.1016/j.corsci.2020.108618.

[4] R.H. Jones, D.R. Baer, M.J. Danielson, J.S. Vetrano, Role of Mg in the Stress Corrosion Cracking of and Al-Mg Alloy, Metallurgical and Materials Transactions A 32A (2001) 1699–1711.

[5] M.E. McMahon, J.R. Scully, J.T. Burns, Mitigation of Intergranular Stress Corrosion Cracking in Al–Mg by Electrochemical Potential Control, JOM 69 (2017) 1389–1397. https://doi.org/10.1007/s11837-017-2362-2.

[6] P.J. Steiner, Z.D. Harris, C. Vicente Moraes, R.G. Kelly, J.T. Burns, Investigation of IG-SCC Growth Kinetics in Al-Mg Alloys in Thin Film Environments, Corrosion 77 (2021) 838–852. https://doi.org/10.5006/3833.

[7] M.E. McMahon, P.J. Steiner, A.B. Lass, J.T. Burns, The effect of loading orientation on the stress corrosion cracking of Al-Mg alloys, Corrosion 73 (2017) 713–723. https://doi.org/10.5006/2343.

[8] P.J. Steiner, Z.D. Harris, J.T. Burns, Effect of Chloride Concentration on the Environment-Assisted Cracking Behavior of an Al-Mg Alloy in Atmospheric Environments, Corrosion 79 (2023) 1223–1233. https://doi.org/10.5006/4279.

[9] P.J. Steiner, J.T. Burns, Mechanistic studies of intergranular stress corrosion cracking in Al-Mg alloys under atmospheric exposure conditions, Corrosion 74 (2018) 1117–1131. https://doi.org/10.5006/2853.

[10] M. Pourbaix, Atlas of Electrochemical Equilibria in-Aqueous Solutions, n.d.

[11] M.E. McMahon, Z.D. Harris, J.R. Scully, J.T. Burns, The effect of electrode potential on stress corrosion cracking in highly sensitized Al–Mg alloys, Materials Science and Engineering: A 767 (2019). https://doi.org/10.1016/j.msea.2019.138399.

[12] Standard Practice for Operating Salt Spray (Fog) Apparatus 1, (n.d.). https://doi.org/10.1520/B0117-19.

[13] D. Scotto D'Antuono, J. Gaies, W. Golumbfskie, M.L. Taheri, Direct measurement of the effect of cold rolling on β phase precipitation kinetics in 5xxx series aluminum alloys, Acta Mater 123 (2017) 264–271. https://doi.org/10.1016/j.actamat.2016.10.060.

[14] R. Zhang, R.K. Gupta, C.H.J. Davies, A.M. Hodge, M. Tort, K. Xia, N. Birbilis, The influence of grain size and grain orientation on sensitization in AA5083, in: Corrosion, 2016. https://doi.org/10.5006/1703.

[15] J.G. Kaufman, Stress-Corrosion Cracking of Aluminum Alloys, in: Properties and Selection of Aluminum Alloys, ASM International, 2019: pp. 79–95. https://doi.org/10.31399/asm.hb.v02b.a0006545.

[16] D. Scotto D'Antuono, J. Gaies, W. Golumbfskie, M.L. Taheri, Grain boundary misorientation dependence of β phase precipitation in an Al-Mg alloy, Scr Mater 76 (2014) 81–84. https://doi.org/10.1016/j.scriptamat.2014.01.003.

[17] Y. Zhao, M.N. Polyakov, M. Mecklenburg, M.E. Kassner, A.M. Hodge, The role of grain boundary plane orientation in the β phase precipitation of an Al-Mg alloy, Scr Mater 89 (2014) 49–52. https://doi.org/10.1016/j.scriptamat.2014.07.003.

[18] X. Sauvage, N. Enikeev, R. Valiev, Y. Nasedkina, M. Murashkin, Atomic-scale analysis of the segregation and precipitation mechanisms in a severely deformed Al-Mg alloy, Acta Mater 72 (2014) 125–136. https://doi.org/10.1016/j.actamat.2014.03.033.

[19] F. Qin, C. Yang, H. Qi, C. Liu, H. Qi, Grain Size, Precipitation Behavior, and Mechanical Properties through the Thickness of Al-Mg-Si Aluminum Alloy Rings Produced by Compact Cast-Rolling Compound Forming, J Mater Eng Perform 31 (2022) 2329–2340. https://doi.org/10.1007/s11665-021-06326-7.

[20] D.L. Foley, A.C. Leff, A.C. Lang, M.L. Taheri, Evolution of β-phase precipitates in an aluminum-magnesium alloy at the nanoscale, Acta Mater 185 (2020) 279–286. https://doi.org/10.1016/j.actamat.2019.10.024.

[21] M. Lyn, C. Lim, Intergranular Corrosion Propagation in Sensitized Al-Mg Alloys, 2016.

[22] J.H. Ai, M.L.C. Lim, J.R. Scully, Effective hydrogen diffusion in aluminum alloy 5083-H131 as a function of orientation and degree of sensitization, Corrosion 69 (2013) 1225–1239. https://doi.org/10.5006/0987.

[23] J. Desai Choundraj, J. Kacher, Influence of misorientation angle and local dislocation density on β-phase distribution in Al 5xxx alloys, Sci Rep 12 (2022). https://doi.org/10.1038/s41598-022-05948-8.

[24] Designation: E112 − 13 Standard Test Methods for Determining Average Grain Size 1, (n.d.). https://doi.org/10.1520/E0112-13R21.

[25] Standard Test Method for Linear-Elastic Plane-Strain Fracture Toughness of Metallic Materials 1, (n.d.). https://doi.org/10.1520/E0399-22.

[26] R.P. Gangloff, D.C. Slavik, R.S. Piascik, R.H. Van Stone, Direct Current Electrical Potential Measurement of the Growth of Small Cracks, American Society for Testing and Materials (1992) 116–168.

[27] Standard Test Method for Measurement of Fatigue Crack Growth Rates 1, (n.d.). https://doi.org/10.1520/E0647-23A.

[28] Z.D. Harris, J.T. Burns, On the loading rate dependence of environment-assisted cracking in sensitized AA5456-H116 exposed to marine environments, Corros Sci 201 (2022). https://doi.org/10.1016/j.corsci.2022.110267.

[29] R.P. Gangloff, H.M. Ha, J.T. Burns, J.R. Scully, Measurement and modeling of hydrogen environment-assisted cracking in monel K-500, Metall Mater Trans A Phys Metall Mater Sci 45 (2014) 3814–3834. https://doi.org/10.1007/s11661-014-2324-z.

[30] J.X. Zhang, M. Ma, W.C. Liu, Effect of initial grain size on the recrystallization and recrystallization texture of cold-rolled AA 5182 aluminum alloy, Materials Science and Engineering: A 690 (2017) 233–243. https://doi.org/10.1016/j.msea.2017.03.015.

[31] P. Ebenberger, P.J. Uggowitzer, B. Gerold, S. Pogatscher, Effect of compositional and processing variations in new 5182-type AlMgMn alloys on mechanical properties and deformation surface quality, Materials 12 (2019). https://doi.org/10.3390/ma12101645.

[32] W. Gao, D. Wang, M. Seifi, J.J. Lewandowski, Anisotropy of corrosion and environmental cracking in AA5083-H128 Al-Mg alloy, Materials Science and Engineering: A 730 (2018) 367–379. https://doi.org/10.1016/j.msea.2018.06.021.

[33] J.L. Searles, P.I. Gouma, R.G. Buchheit, Stress Corrosion Cracking of Sensitized AA5083 (Al-4.5Mg-1.0Mn), n.d.

[34] A.J. Davenport, Y. Yuan, R. Ambat, B.J. Connolly, M. Strangwood, A. Afseth, G.M. Scamans, Intergranular Corrosion and Stress Corrosion Cracking of Sensitised AA5182, Materials Science Forum 519–521 (2006) 641–646. https://doi.org/10.4028/www.scientific.net/msf.519-521.641.

[35] C.: Yuan, Yudie, Localised corrosion and stress cracking of aluminium-magnesium alloys, University of Birmingham, 2005.

[36] R. Zhang, S.P. Knight, R.L. Holtz, R. Goswami, C.H.J. Davies, N. Birbilis, A survey of sensitization in 5xxx series aluminum alloys, in: Corrosion, National Assoc. of Corrosion Engineers International, 2016: pp. 144–159. https://doi.org/10.5006/1787.

[37] C.B. Crane, R.P. Gangloff, Stress corrosion cracking of Al-Mg alloy 5083 sensitized at low temperature, in: Corrosion, National Assoc. of Corrosion Engineers International, 2016: pp. 221–241. https://doi.org/10.5006/1766.

[38] M.E. McMahon, P.J. Steiner, A.B. Lass, J.T. Burns, The effect of temper and composition on the stress corrosion cracking of Al-Mg alloys, Corrosion 73 (2017) 347–361. https://doi.org/10.5006/2317.

[39] Z.D. Harris, J.T. Burns, On the loading rate dependence of environment-assisted cracking in sensitized AA5456-H116 exposed to marine environments, Corros Sci 201 (2022). https://doi.org/10.1016/j.corsci.2022.110267.

[40] M.E. McMahon, J.R. Scully, J.T. Burns, Mitigation of Intergranular Cracking in Al-Mg Alloys via Zn-Based Electrode Potential Control in Sodium Chloride Solution, Corrosion 75 (2019) 911–928. https://doi.org/10.5006/3185.

[41] R. Sanders, J. Staley, A History of Wrought Aluminum Alloys and Applications, in: Properties and Selection of Aluminum Alloys, ASM International, 2019: pp. 157–201. https://doi.org/10.31399/asm.hb.v02b.a0006516.

[42] N. Brown, P. Kramer, F. Friedersdorf, M. Schindelholz, J. Siegel, Environmentally assisted cracking measurements in structural aluminum alloys under accelerated test conditions, Corrosion 72 (2016) 1351–1362. https://doi.org/10.5006/2085.

[43] C. Liu, J. Srinivasan, R.G. Kelly, Editors' Choice—Electrolyte Film Thickness Effects on the Cathodic Current Availability in a Galvanic Couple, J Electrochem Soc 164 (2017) C845–C855. https://doi.org/10.1149/2.1641713jes.

[44] F. Ge, L. Zhang, H. Tian, M. Yu, J. Liang, X. Wang, Stress Corrosion Cracking Behavior of 2024 and 7075 High-Strength Aluminum Alloys in a Simulated Marine Atmosphere Contaminated with SO2, J Mater Eng Perform 29 (2020) 410–422. https://doi.org/10.1007/s11665-019-04537-7.

[45] M. WANG, L. WANG, K. PANG, Y. LIU, Y. WANG, Z. CUI, Understanding stress corrosion cracking behavior of 7085-T7651 aluminum alloy in polluted atmosphere, Chinese Journal of Aeronautics 36 (2023) 408–421. https://doi.org/10.1016/j.cja.2023.06.011.

[46] E.M. Arnold, J.J. Schubbe, P.J. Moran, R.A. Bayles, Comparison of SCC thresholds and environmentally assisted cracking in 7050-T7451 aluminum plate, J Mater Eng Perform 21 (2012) 2480–2486. https://doi.org/10.1007/s11665-012-0204-5.

[47] PENAIR ® M5571, n.d.

[48] G.A. Truesdale, A.L. Downing, Solubility of Oxygen in Water, Nature 173 (1954) 1236.

[49] I.W. Huang, B.L. Hurley, F. Yang, R.G. Buchheit, Dependence on Temperature, pH, and Cl- in the Uniform Corrosion of Aluminum Alloys 2024-T3, 6061-T6, and 7075-T6, Electrochim Acta 199 (2016) 242–253. https://doi.org/10.1016/j.electacta.2016.03.125.

[50] C.N. Panagopoulos, E. Georgiou, K.I. Giannakopoulos, P.G. Orfanos, Effect of ph on stress corrosion cracking of 6082 al alloy, Metals (Basel) 8 (2018). https://doi.org/10.3390/met8080578.

[51] W.-T. Tsai, J.-B. Duh, J.-J. Yeh, J.-T. Lee, Y.-C. Chang"', Effect of pH on Stress Corrosion Cracking of 7050-T7451 Aluminum Alloy in 3.5 wt% NaCI Solution *, 1990. http://meridian.allenpress.com/corrosion/article-pdf/46/6/444/1530787/1_3585130.pdf.

[52] Z. Dan, I. Muto, N. Hara, Effects of environmental factors on atmospheric corrosion of aluminium and its alloys under constant dew point conditions, Corros Sci 57 (2012) 22–29. https://doi.org/10.1016/j.corsci.2011.12.038.

[53] T.F. Cui, D.X. Liu, P.A. Shi, J.J. Liu, Y.H. Yi, H.L. Zhou, Effect of NaCl concentration, pH value and tensile stress on the galvanic corrosion behavior of 5050 aluminum alloy, Materials and Corrosion 67 (2016) 72–83. https://doi.org/10.1002/maco.201408189.

[54] E. Bumiller, INTERGRANULAR CORROSION IN AA5XXX ALUMINUM ALLOYS WITH DISCONTINUOUS PRECIPITATION AT THE GRAIN BOUNDARIES A Dissertation Presented to, 2011.

[55] J.A. Lyndon, R.K. Gupta, M.A. Gibson, N. Birbilis, Electrochemical behaviour of the β-phase intermetallic (Mg2Al3) as a function of pH as relevant to corrosion of aluminium-magnesium alloys, Corros Sci 70 (2013) 290–293. https://doi.org/10.1016/j.corsci.2012.12.022.

[56] B. Zaid, D. Saidi, A. Benzaid, S. Hadji, Effects of pH and chloride concentration on pitting corrosion of AA6061 aluminum alloy, Corros Sci 50 (2008) 1841–1847. https://doi.org/10.1016/j.corsci.2008.03.006.

[57] C.B. Crane, R.G. Kelly, R.P. Gangloff, Crack chemistry control of intergranular stress corrosion cracking in sensitized Al-Mg, in: Corrosion, National Assoc. of Corrosion Engineers International, 2016: pp. 242–263. https://doi.org/10.5006/1852.

Chapter 5: Testing the Effect of Chloride Concentration and Solution pH on the Crack Growth Kinetics of Alloy 1 Exposed to Atmospheric Environments

5.1 Introduction

Aluminum alloy (AA) corrosion is highly dependent on the electrolyte exposure. Of these dependencies, the effect of pH, chloride concentration, and temperature have been widely studied [49–52]. The 5xxx series AA are susceptible to corrosion and changes in electrolyte characteristics because of the precipitation of the anodic beta phase on the grain boundaries leaving these alloys prone to intergranular corrosion (IGC) and intergranular stress corrosion cracking (IGSCC). Again, these alloys are not immune to changes in corrosion behavior based on fluctuations in pH and chloride concentration. For example, Cui *et al.* showed the corrosion of AA5050 was highly dependent on the Cl- concentration, with more negative open circuit potentials and increased current densities as the chloride concentration increased (from distilled water, to 3.5% NaCl, to 5% NaCl) [53]. Bumiller also showed a similar trend for AA5456-H116, resulting in decreasing OCP with exposure to increasing pH buffer solutions (pH buffer 3, pH buffer 8, and pH buffer 11 – all chloride free) [54].

In the context of IGC and IGSCC, characterization of the anodic beta phase is also important to understand alongside the electrochemical behavior of the bulk alloy, because of the electrochemical driving force for corrosion based on the known potential difference between the two phases. McMahon *et al.* studied the increase in chloride concentration exposure to pure beta phase resulted in decreased OCP and decreased pitting potential, leading to increased IGSCC susceptibility of the bulk alloy (AA5456-H116) because of increased anodic dissolution and more aggressive crack tip chemistry [5]. Lyndon *et al.* studied the effect of pH on the beta phase corrosion, and determined that there is a pH dependency, with more active corrosion in acidic solutions [55].

It is useful to examine these alloys in atmospheric environments because of increasing usage in industries where full immersion testing does not necessarily replicate in-service conditions. These environments have been shown to change the corrosion susceptibility of AA5xxx, which is not accounted for in full immersion electrochemical testing [6,8,9]. Steiner *et al.* showed that there is decreased IGSCC susceptibility of AA5456-H116 and AA5083-H131 in atmospheric environments compared to full immersion tests because of a change in available cathodic area necessary for corrosion reactions to occur [9]. Furthermore, in a follow up study, Steiner *et al.* also showed the increased SCC susceptibility of these same alloys to atmospheric environments when the chloride concentration was increased because of

increased dissolution and thus higher IGSCC susceptibility [8]. Past work on Alloy 1 showed the decreased SCC resistance when testing in full immersion to atmospheric environments in very benign solutions (low chloride concentration and slightly basic solution), which was explained to be caused by the less aggressive environment and increased oxygen availability in the atmospheric exposure (Chapter 4). However, given the known effects of increasing chloride concentration giving increased susceptibility in atmospheric environments needs to be studied for Alloy 1 in the event that there is exposure to solutions of this type. Furthermore, it is necessary to understand and evaluate the IGSCC susceptibility of Alloy 1 in solutions with varied pH. As such, it is the aim of this study to test the IGSCC resistance of Alloy 1 exposed to atmospheric environments with varied electrolytes, specifically targeting a range of pH and chloride concentrations exposures because of the studied dependence of other AA5xxx to these environmental factors.

5.2 Materials and Methods

5.2.1 Electrochemical Testing

A small specimen of Alloy 1 was prepared for electrochemical testing in a flat cell by polishing to 1200 grit with deionized (DI) water. Pure beta alloy (Al_3Mg_2) was also prepared in a similar fashion, but ethanol was used as the solvent during polishing. After polishing, the sample was placed in the electrochemical flat cell, exposing 1 cm^2. A typical three electrode setup was utilized with a copper wire attached to the metallographic sample (Alloy 1 or Al_3Mg_2) as the working electrode, a saturated calomel electrode (SCE) as the reference electrode, and Pt mesh as the counter electrode. A Biologic Potentiostat was used to monitor open circuit potential (OCP) measurements 60 or 30 minutes (for Alloy 1 and Al_3Mg_2 respectively), as well as apply set potential and record current measurements. Anodic scans of Alloy 1 and Al_3Mg_2 were gathered after OCP stabilization, starting at the OCP, stopping at +0.5 VSCE at a step rate of 0.167 mV/s. Cathodic scans of Alloy 1 were run at OCP until -2.0 VSCE at the same rate as the anodic scans. Three replicate tests were completed of the anodic and cathodic kinetics and the curves presented in the results are a representative result of the three repeat experiments. After the potentiodynamic scan, the sample was removed from the flat cell, rinsed with DI water, and imaged using a Hirox RH-8800 microscope to confirm the exposed area during the experiment.

Different electrolytes were exposed to the specimen to obtain electrochemical measurements, and are characterized by their chloride content and pH. This summary is provided in Table 5.1. Solution 1 is the same Solution 1 from Chapter 4 and has low chloride concentration and slightly basic pH. Solution 2 is 0.6 M NaCl, and has significantly more chloride than Solution 1 and also has a slightly acidic pH.

Solution 3 is a combination of Solutions 1 and 2, and has the most chloride concentration (but not much more than Solution 2), and also has a slightly acidic/near neutral pH. Solution 4 is the most acidic solution and has moderate chloride concentration (less than Solutions 2 and 3, but much more than Solution 1).

Table 5.1: The pH and chloride concentration of Solutions 1-4 used in this study

Electrolyte	pH	$[Cl^-]$ (mg/L)
Solution 1	7.9	10
Solution 2 (= 0.6 M NaCl)	6	35060
Solution 3 (= Solution 1+ 0.6 M NaCl)	7.69	35070
Solution 4	2.05	2022

5.2.2 Linear Elastic Fracture Mechanics Testing (LEFM) in Atmospheric Environments

Single edge notch tension (SENT) specimen were fabricated from 3.5 mm sheets of Alloy 1 in the T-L orientation. The total length of the specimen was 177.8 mm, a width of 25.4 mm and an average thickness of 3.33 mm. An electrical discharge machined (EDM) notch was placed at the center of the specimen length, with a depth equaling 5.7 mm.

These SENT specimen were subjected to tensile loading in the form of linear elastic fracture mechanics (LEFM) testing approach, in a stress intensity (K) controlled loading protocol. First, a fatigue precrack protocol was performed in lab air to a final crack length of 6.0 mm and a maximum K of 2 or 4 MPa√m. Stress corrosion cracking (SCC) experiments followed fatigue precrack via slow rising displacement tests in an atmospheric environment at a rate of 1 MPa√m/hr. The atmospheric environment was simulated using two conical fine spray misting nozzles which continuously sprayed electrolyte onto the SENT specimen – to be known as the misting condition. An acrylic cell was placed around the samples and Solutions 1-4 were misted at a rate of 40 mL/min. Each solution was collected and circulated in a 2 L reservoir of the same solution. Each specimen was lacquered such that approximately one inch surrounding the notch (½ inch above and ½ inch below) and the entire specimen width was exposed to solution (such that crack growth was unobstructed) and the remaining areas were unexposed. Open circuit potential (OCP) measurements were gathered using a Biologic PG-581 handheld potentiostat, with the SENT specimen as the working electrode and Ag/AgCl as the reference electrode.

5.3 Results

5.3.1 Electrochemical Results of Alloy 1 and Al_3Mg_2 in Solutions 1-4

Representative polarization curves of Alloy 1 exposed to Solutions 1-4 are presented in Figure 5.1. Most notably from these results is the increased anodic current density of Alloy 1 exposed to Solution 4, which had the lowest pH, indicating increased rates of anodic dissolution. The OCP values are in the range of -700 mVSCE and -900 mVSCE, but average OCP measurements as a function of chloride concentration are presented in Figure 5.2. It is obvious from Figure 5.2 that the increasing chloride concentration decreases the OCP. This is expected because of the known dependence of aluminum OCP with increased chloride concentration [56]. From Figure 5.2 it is noticeable that the solutions with significant increases in chloride concentration (Solutions 2-4) make Alloy 1 more susceptible to corrosion because of the decreased OCP. On the other hand, increased corrosion current density of Alloy 1 exposed to Solution 4 (Figure 5.1) also showed enhanced susceptibility.

The anodic polarization curves of Al_3Mg_2 exposed to Solutions 1-4 (Figure 5.3) show wide spreading of the OCP values, ranging from -1.0 VSCE to -1.4 VSCE. Figure 4 highlights the average OCP and pitting potential values of Al_3Mg_2 as a function of chloride concentration. A similar trend in OCP as Alloy 1 is observed for Al_3Mg_2, with the exception that the OCP of Al_3Mg_2 in Solution 3 (-0.9 V_{SCE}) is significantly higher than in Solution 2 (-1.5 V_{SCE}) despite nearly the same chloride concentration (~35070 mg/L). In addition, there is a related trend in pitting potentials of Al_3Mg_2 that increasing chloride concentration decreases the breakdown (pitting) potential. Note that the breakdown potential of Al_3Mg_2 in Solutions 2 and 3 are almost equivalent (as shown in Figure 5.3 and Figure *5.4*). The anodic kinetics of beta phase in Solution 4 (pH ≈ 2) shows high anodic corrosion current density, which is indicative of high dissolution rates. This is not observed for the other chloride containing, higher pH solutions, and a similar result was found for Alloy 1 in the same solution (Figure 5.1). Additionally, the passive current density of Al_3Mg_2 exposed to Solution 4 is much greater than the other passive current densities (Figure 5.3), approximately three orders of magnitude greater than that of Solution 1, and between 2-2.5 orders of magnitude greater than Solutions 2 and 3. This again indicates high rates of dissolution of Al_3Mg_2 in Solution 4.

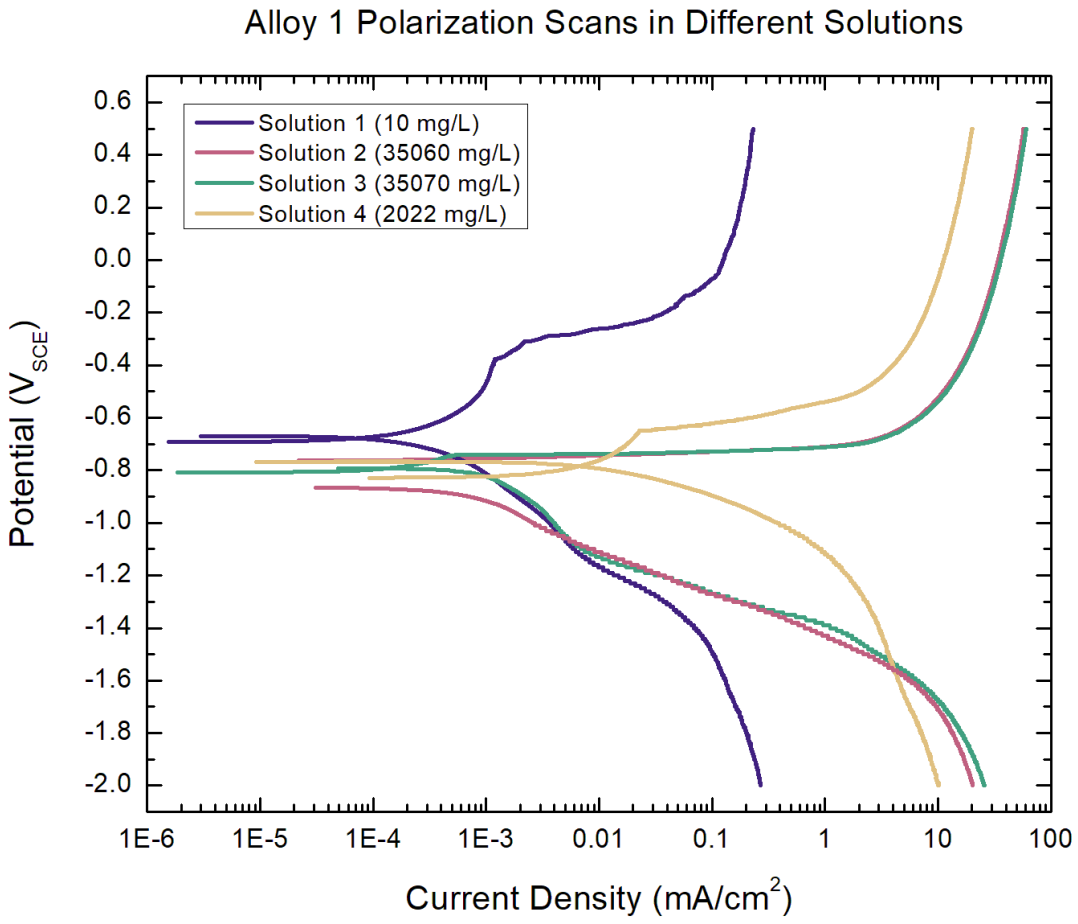

Figure 5.1: Anodic and cathodic polarization curves of Alloy 1 in Solutions 1-4 (the legend also contains the chloride concentration of each solution for reference). Note these scans were run after 60 minutes of OCP hold.

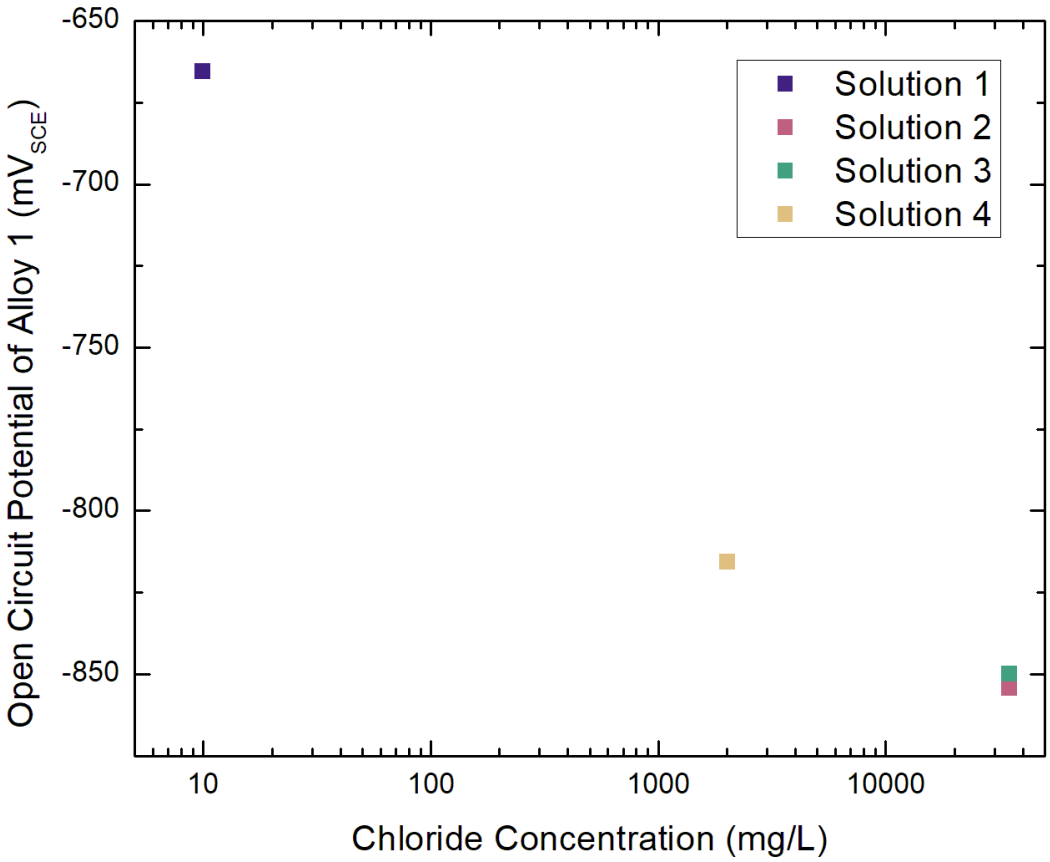

Figure 5.2: OCP of Alloy 1 in Solutions 1-4 as a function of chloride concentration

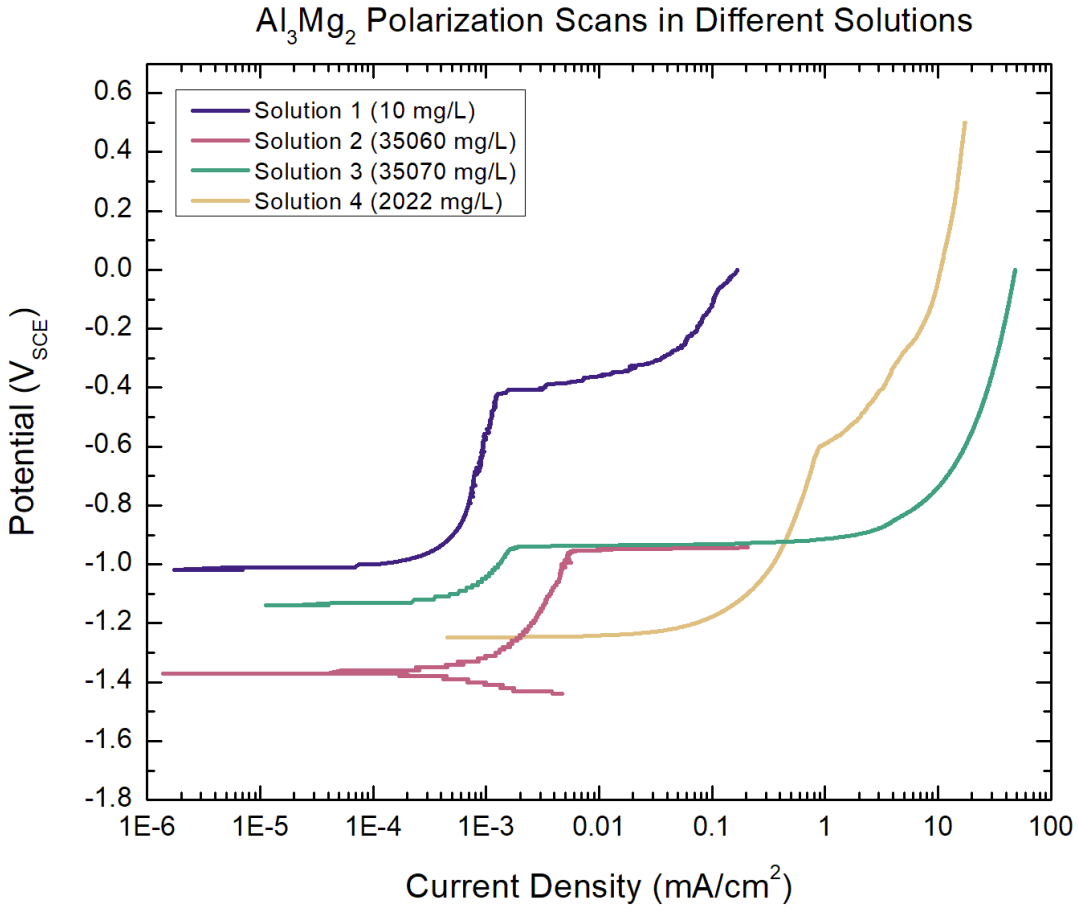

Figure 5.3: Anodic polarization curves of Al_3Mg_2 in Solutions 1-4 (the chloride concentration of each solution is added to the legend for reference). Note the scans were run after 30 minute OCP hold.

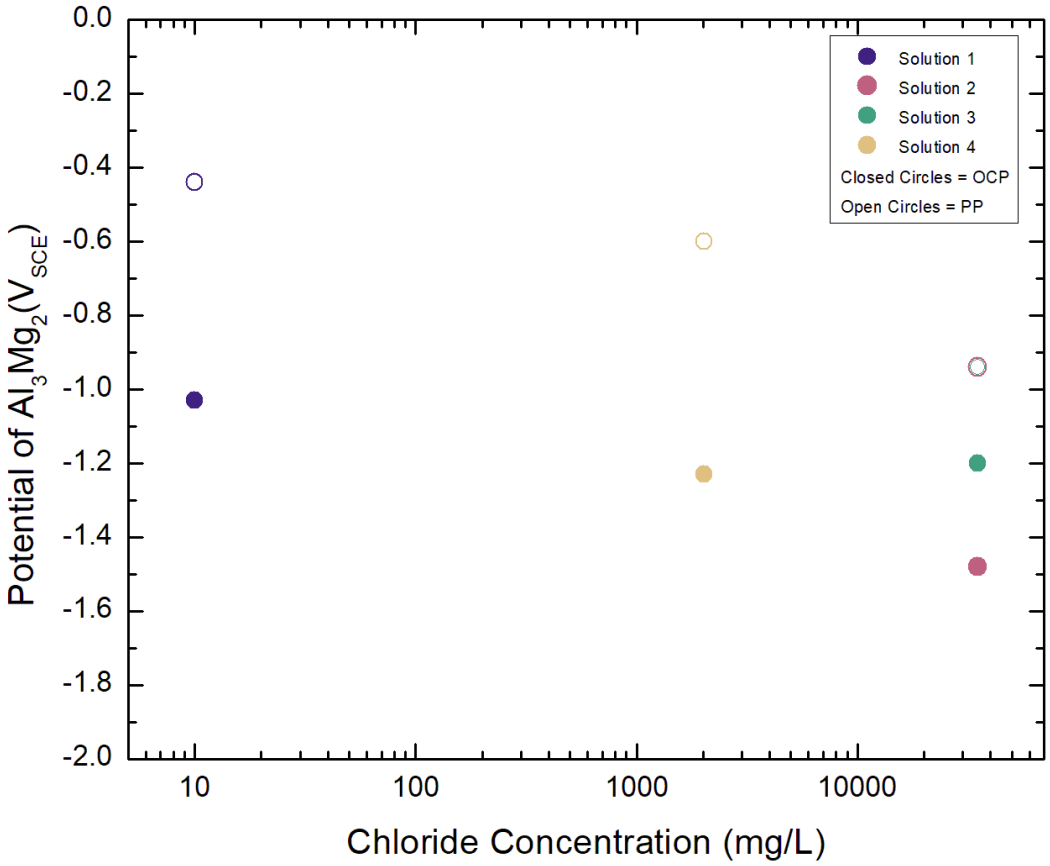

Figure 5.4: Open circuit potential (OCP) and pitting potential (PP) of Al_3Mg_2 in Solutions 1-4 as a function of chloride concentration.

5.3.2 Crack Growth Kinetics of Alloy 1 in Solutions 1-4 Tested in Atmospheric Environments

Stress corrosion cracking kinetics of Alloy 1 exposed to atmospheric environments (misting exposure) with varying solution chemistries (Solutions 1-4) are presented in Figure 5. *5*. There are a few noticeable trends: 1. Exposure of Alloy 1 to the least chloride containing solution (Solution 1) showed the slowest cracking kinetics, 2. Exposure to Solutions 2 and 3 had similar crack growth at low K values, and 3. Exposure to the most acidic solution (Solution 4) had the fast crack growth rates. Stated more simply: crack growth rates increased with exposure of Alloy 1 to (in order from slowest to fastest) Solution 1, Solution 2, Solution 3, and Solution 4. Crack growth kinetics increase with increased chloride concentration, but the most acidic solution has the fastest crack growth rates as seen from Figure 5. *5*. This could have been expected from the decrease in OCP of Alloy 1 exposed to Solutions 1-3, and increased anodic kinetics of Al_3Mg_2 from exposure to Solution 4. The pH becomes an important and dominating factor in SCC compared to chloride concentration because of the fastest crack growth kinetics with exposure to the most acidic solution (but not the most chloride concentrated solution) (Solution 4).

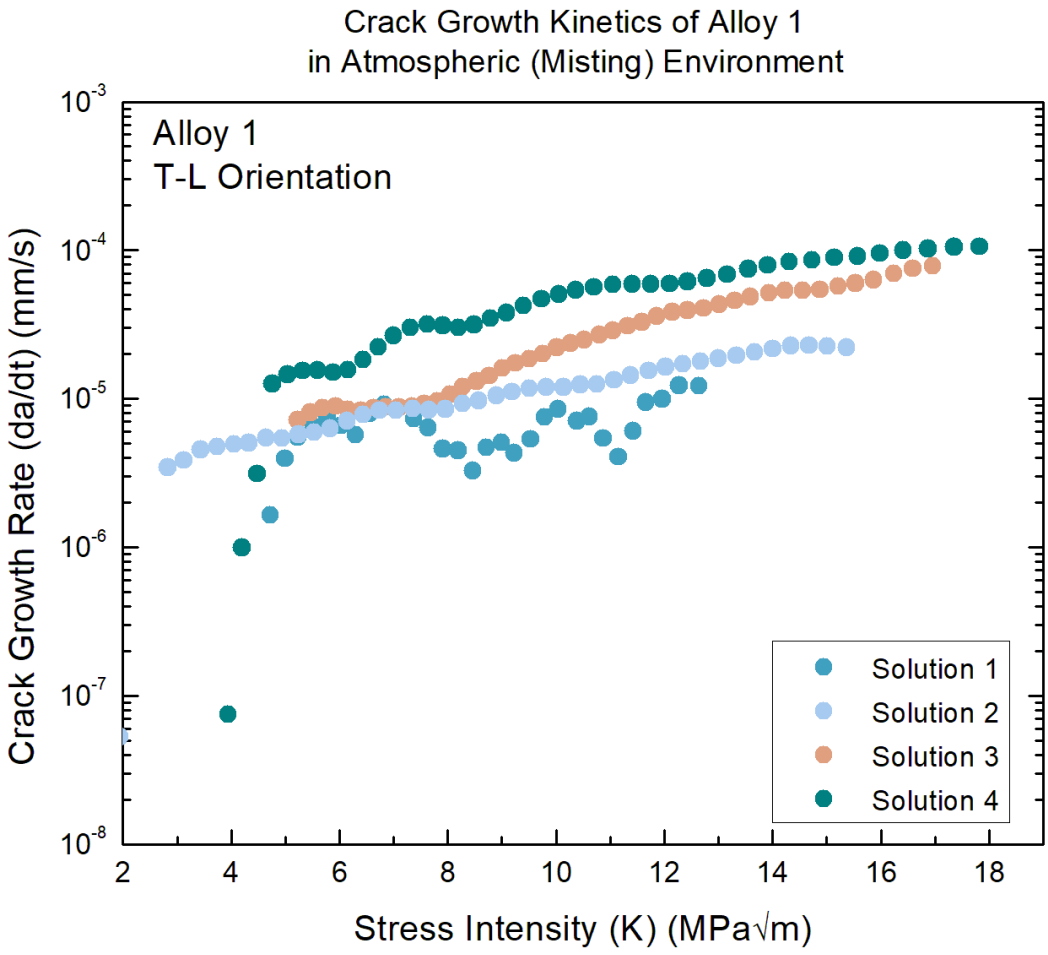

Figure 5. 5: Crack growth rate vs. stress intensity of Alloy 1 exposed to Solutions 1-4 in the misting condition.

5.4 Discussion

The key finding to comment on is the increasing crack growth kinetics of Alloy 1 exposed to atmospheric environments with elevated chloride concentrations and decreased pH. Specifically in this study, Alloy 1 is most susceptible to Solution 4, which has the lowest pH. The polarization curves in Figure 5.1 and Figure *5.3* can be leveraged to reason through the SCC results. Both Alloy 1 and Al_3Mg_2 had increased anodic kinetics, meaning there is more dissolution of Alloy 1 and β phase when exposed to Solution 4. The proposed mechanism for IGSCC for Alloy 1 follows that of other Al-Mg systems, as studied in previous chapters. The anodic dissolution hydrogen embrittlement mechanism first begins with anodic dissolution of the β (and subsequently α-Al matrix) phase(s). If the solution exposed to Alloy 1 is already

at a predisposition for increased dissolution rates, then it is reasonable to follow that there are increased cracking kinetics in this solution because of the increased rate of anodic dissolution. It is important to note that the polarization curve of beta phase in Solution 4 (Figure 5.3) has a higher breakdown potential than in the more chloride containing solutions (Solutions 2 and 3), but the results are ruled by the anodic kinetics, not the potential.

Furthermore, the increased pH allows for an even more aggressive crack chemistry because pH of the crack tip is modelled to be much lower than the bulk solution [21,57]. This more aggressive crack chemistry allows for increased hydrogen production, hydrogen uptake, and embrittlement of the material ahead of the crack tip, causing more crack growth overall.

As the solutions become less acidic and more near-neutral pH, the crack growth kinetics are controlled by the chloride concentration. This is observed in **Error! Reference source not found.** and can b e explained from the results of the polarization curves. Increasing the chloride concentration is known to increase the crack growth kinetics and the corrosion susceptibility [5,8]. The increased chloride concentration decreases the OCP of both the α and β phases (Figure 5.2 andFigure *5.4*) and decreases the β pitting potential (Figure 5.4). McMahon *et al.* showed that for chloride concentrations of 0.6 M NaCl and above, the increased chloride concentration effectively increased the IGSCC susceptibility because of a more aggressive crack chemistry, which gives a lower pH [5].

The interesting point to notice is that Alloy 1 exposed to an atmospheric environment is susceptible to IGSCC. No matter the solution type, Alloy 1 can experience some level of crack growth. There are other relevant atmospheric solution geometries (e.g. wicking) that could be relevant to this test matrix, but the point of this study was solely to compare the performance of Alloy 1 when exposed to these specific solutions in a misting environment. Bringing in some of the discussion from Chapter 4, it is relevant to identify the factor which is controlling the available cathodic current in this atmospheric environment. It was discussed previously that exposure to Solution 1 caused the available cathodic current to be controlled by the oxygen transport, whereas it has been studied in the past that the ohmic resistance was controlling the available cathodic current in for exposure to 0.6 M NaCl [6,9]. Future work should include comparing the observed crack growth kinetics of Alloy 1 in atmospheric environments and comparing them to the full immersion crack growth rates, similar to what was completed in Chapter 4.

5.5 Conclusions

Atmospheric testing via LEFM of Alloy 1 with different solution exposures resulted in a dependency of solution chemistry based on chloride concentration and solution pH. These dependencies were:

1. Solutions with near neutral pH (pH range from 6-8) showed increased crack growth kinetics for increasing chloride concentration
2. More acidic solutions (pH = 2) had the fastest crack growth kinetics, despite moderate chloride concentration
3. A solution with negligible chloride concentration and slightly basic pH had the slowest crack growth kinetics

References

[1] G.M. Scamans, N.J.H. Holroyd, C.D.S. Tuck, THE ROLE OF MAGNESIUM SEGREGATION IN THE INTERGRANULAR STRESS CORROSION CRACKING OF ALUMINIUM ALLOYS, 1987.

[2] Standard Test Method for Determining the Susceptibility to Intergranular Corrosion of 5XXX Series Aluminum Alloys by Mass Loss After Exposure to Nitric Acid (NAMLT Test) 1, (n.d.). https://doi.org/10.1520/G0067-18.

[3] M.E. McMahon, R.L. Haines, P.J. Steiner, J.M. Schulte, S.E. Fakler, J.T. Burns, Beta phase distribution in Al-Mg alloys of varying composition and temper, Corros Sci 169 (2020). https://doi.org/10.1016/j.corsci.2020.108618.

[4] R.H. Jones, D.R. Baer, M.J. Danielson, J.S. Vetrano, Role of Mg in the Stress Corrosion Cracking of and Al-Mg Alloy, Metallurgical and Materials Transactions A 32A (2001) 1699–1711.

[5] M.E. McMahon, J.R. Scully, J.T. Burns, Mitigation of Intergranular Stress Corrosion Cracking in Al–Mg by Electrochemical Potential Control, JOM 69 (2017) 1389–1397. https://doi.org/10.1007/s11837-017-2362-2.

[6] P.J. Steiner, Z.D. Harris, C. Vicente Moraes, R.G. Kelly, J.T. Burns, Investigation of IG-SCC Growth Kinetics in Al-Mg Alloys in Thin Film Environments, Corrosion 77 (2021) 838–852. https://doi.org/10.5006/3833.

[7] M.E. McMahon, P.J. Steiner, A.B. Lass, J.T. Burns, The effect of loading orientation on the stress corrosion cracking of Al-Mg alloys, Corrosion 73 (2017) 713–723. https://doi.org/10.5006/2343.

[8] P.J. Steiner, Z.D. Harris, J.T. Burns, Effect of Chloride Concentration on the Environment-Assisted Cracking Behavior of an Al-Mg Alloy in Atmospheric Environments, Corrosion 79 (2023) 1223–1233. https://doi.org/10.5006/4279.

[9] P.J. Steiner, J.T. Burns, Mechanistic studies of intergranular stress corrosion cracking in Al-Mg alloys under atmospheric exposure conditions, Corrosion 74 (2018) 1117–1131. https://doi.org/10.5006/2853.

[10] M. Pourbaix, Atlas of Electrochemical Equilibria in-Aqueous Solutions, n.d.

[11] M.E. McMahon, Z.D. Harris, J.R. Scully, J.T. Burns, The effect of electrode potential on stress corrosion cracking in highly sensitized Al–Mg alloys, Materials Science and Engineering: A 767 (2019). https://doi.org/10.1016/j.msea.2019.138399.

[12] Standard Practice for Operating Salt Spray (Fog) Apparatus 1, (n.d.). https://doi.org/10.1520/B0117-19.

[13] D. Scotto D'Antuono, J. Gaies, W. Golumbfskie, M.L. Taheri, Direct measurement of the effect of cold rolling on β phase precipitation kinetics in 5xxx series aluminum alloys, Acta Mater 123 (2017) 264–271. https://doi.org/10.1016/j.actamat.2016.10.060.

[14] R. Zhang, R.K. Gupta, C.H.J. Davies, A.M. Hodge, M. Tort, K. Xia, N. Birbilis, The influence of grain size and grain orientation on sensitization in AA5083, in: Corrosion, 2016. https://doi.org/10.5006/1703.

[15] J.G. Kaufman, Stress-Corrosion Cracking of Aluminum Alloys, in: Properties and Selection of Aluminum Alloys, ASM International, 2019: pp. 79–95. https://doi.org/10.31399/asm.hb.v02b.a0006545.

[16] D. Scotto D'Antuono, J. Gaies, W. Golumbfskie, M.L. Taheri, Grain boundary misorientation dependence of β phase precipitation in an Al-Mg alloy, Scr Mater 76 (2014) 81–84. https://doi.org/10.1016/j.scriptamat.2014.01.003.

[17] Y. Zhao, M.N. Polyakov, M. Mecklenburg, M.E. Kassner, A.M. Hodge, The role of grain boundary plane orientation in the β phase precipitation of an Al-Mg alloy, Scr Mater 89 (2014) 49–52. https://doi.org/10.1016/j.scriptamat.2014.07.003.

[18] X. Sauvage, N. Enikeev, R. Valiev, Y. Nasedkina, M. Murashkin, Atomic-scale analysis of the segregation and precipitation mechanisms in a severely deformed Al-Mg alloy, Acta Mater 72 (2014) 125–136. https://doi.org/10.1016/j.actamat.2014.03.033.

[19] F. Qin, C. Yang, H. Qi, C. Liu, H. Qi, Grain Size, Precipitation Behavior, and Mechanical Properties through the Thickness of Al-Mg-Si Aluminum Alloy Rings Produced by Compact Cast-Rolling Compound Forming, J Mater Eng Perform 31 (2022) 2329–2340. https://doi.org/10.1007/s11665-021-06326-7.

[20] D.L. Foley, A.C. Leff, A.C. Lang, M.L. Taheri, Evolution of β-phase precipitates in an aluminum-magnesium alloy at the nanoscale, Acta Mater 185 (2020) 279–286. https://doi.org/10.1016/j.actamat.2019.10.024.

[21] M. Lyn, C. Lim, Intergranular Corrosion Propagation in Sensitized Al-Mg Alloys, 2016.

[22] J.H. Ai, M.L.C. Lim, J.R. Scully, Effective hydrogen diffusion in aluminum alloy 5083-H131 as a function of orientation and degree of sensitization, Corrosion 69 (2013) 1225–1239. https://doi.org/10.5006/0987.

[23] J. Desai Choundraj, J. Kacher, Influence of misorientation angle and local dislocation density on β-phase distribution in Al 5xxx alloys, Sci Rep 12 (2022). https://doi.org/10.1038/s41598-022-05948-8.

[24] Designation: E112 − 13 Standard Test Methods for Determining Average Grain Size 1, (n.d.). https://doi.org/10.1520/E0112-13R21.

[25] Standard Test Method for Linear-Elastic Plane-Strain Fracture Toughness of Metallic Materials 1, (n.d.). https://doi.org/10.1520/E0399-22.

[26] R.P. Gangloff, D.C. Slavik, R.S. Piascik, R.H. Van Stone, Direct Current Electrical Potential Measurement of the Growth of Small Cracks, American Society for Testing and Materials (1992) 116–168.

[27] Standard Test Method for Measurement of Fatigue Crack Growth Rates 1, (n.d.). https://doi.org/10.1520/E0647-23A.

[28] Z.D. Harris, J.T. Burns, On the loading rate dependence of environment-assisted cracking in sensitized AA5456-H116 exposed to marine environments, Corros Sci 201 (2022). https://doi.org/10.1016/j.corsci.2022.110267.

[29] R.P. Gangloff, H.M. Ha, J.T. Burns, J.R. Scully, Measurement and modeling of hydrogen environment-assisted cracking in monel K-500, Metall Mater Trans A Phys Metall Mater Sci 45 (2014) 3814–3834. https://doi.org/10.1007/s11661-014-2324-z.

[30] J.X. Zhang, M. Ma, W.C. Liu, Effect of initial grain size on the recrystallization and recrystallization texture of cold-rolled AA 5182 aluminum alloy, Materials Science and Engineering: A 690 (2017) 233–243. https://doi.org/10.1016/j.msea.2017.03.015.

[31] P. Ebenberger, P.J. Uggowitzer, B. Gerold, S. Pogatscher, Effect of compositional and processing variations in new 5182-type AlMgMn alloys on mechanical properties and deformation surface quality, Materials 12 (2019). https://doi.org/10.3390/ma12101645.

[32] W. Gao, D. Wang, M. Seifi, J.J. Lewandowski, Anisotropy of corrosion and environmental cracking in AA5083-H128 Al-Mg alloy, Materials Science and Engineering: A 730 (2018) 367–379. https://doi.org/10.1016/j.msea.2018.06.021.

[33] J.L. Searles, P.I. Gouma, R.G. Buchheit, Stress Corrosion Cracking of Sensitized AA5083 (Al-4.5Mg-1.0Mn), n.d.

[34] A.J. Davenport, Y. Yuan, R. Ambat, B.J. Connolly, M. Strangwood, A. Afseth, G.M. Scamans, Intergranular Corrosion and Stress Corrosion Cracking of Sensitised AA5182, Materials Science Forum 519–521 (2006) 641–646. https://doi.org/10.4028/www.scientific.net/msf.519-521.641.

[35] C.: Yuan, Yudie, Localised corrosion and stress cracking of aluminium-magnesium alloys, University of Birmingham, 2005.

[36] R. Zhang, S.P. Knight, R.L. Holtz, R. Goswami, C.H.J. Davies, N. Birbilis, A survey of sensitization in 5xxx series aluminum alloys, in: Corrosion, National Assoc. of Corrosion Engineers International, 2016: pp. 144–159. https://doi.org/10.5006/1787.

[37] C.B. Crane, R.P. Gangloff, Stress corrosion cracking of Al-Mg alloy 5083 sensitized at low temperature, in: Corrosion, National Assoc. of Corrosion Engineers International, 2016: pp. 221–241. https://doi.org/10.5006/1766.

[38] M.E. McMahon, P.J. Steiner, A.B. Lass, J.T. Burns, The effect of temper and composition on the stress corrosion cracking of Al-Mg alloys, Corrosion 73 (2017) 347–361. https://doi.org/10.5006/2317.

[39] Z.D. Harris, J.T. Burns, On the loading rate dependence of environment-assisted cracking in sensitized AA5456-H116 exposed to marine environments, Corros Sci 201 (2022). https://doi.org/10.1016/j.corsci.2022.110267.

[40] M.E. McMahon, J.R. Scully, J.T. Burns, Mitigation of Intergranular Cracking in Al-Mg Alloys via Zn-Based Electrode Potential Control in Sodium Chloride Solution, Corrosion 75 (2019) 911–928. https://doi.org/10.5006/3185.

[41] R. Sanders, J. Staley, A History of Wrought Aluminum Alloys and Applications, in: Properties and Selection of Aluminum Alloys, ASM International, 2019: pp. 157–201. https://doi.org/10.31399/asm.hb.v02b.a0006516.

[42] N. Brown, P. Kramer, F. Friedersdorf, M. Schindelholz, J. Siegel, Environmentally assisted cracking measurements in structural aluminum alloys under accelerated test conditions, Corrosion 72 (2016) 1351–1362. https://doi.org/10.5006/2085.

[43] C. Liu, J. Srinivasan, R.G. Kelly, Editors' Choice—Electrolyte Film Thickness Effects on the Cathodic Current Availability in a Galvanic Couple, J Electrochem Soc 164 (2017) C845–C855. https://doi.org/10.1149/2.1641713jes.

[44] F. Ge, L. Zhang, H. Tian, M. Yu, J. Liang, X. Wang, Stress Corrosion Cracking Behavior of 2024 and 7075 High-Strength Aluminum Alloys in a Simulated Marine Atmosphere Contaminated with SO2, J Mater Eng Perform 29 (2020) 410–422. https://doi.org/10.1007/s11665-019-04537-7.

[45] M. WANG, L. WANG, K. PANG, Y. LIU, Y. WANG, Z. CUI, Understanding stress corrosion cracking behavior of 7085-T7651 aluminum alloy in polluted atmosphere, Chinese Journal of Aeronautics 36 (2023) 408–421. https://doi.org/10.1016/j.cja.2023.06.011.

[46] E.M. Arnold, J.J. Schubbe, P.J. Moran, R.A. Bayles, Comparison of SCC thresholds and environmentally assisted cracking in 7050-T7451 aluminum plate, J Mater Eng Perform 21 (2012) 2480–2486. https://doi.org/10.1007/s11665-012-0204-5.

[47] PENAIR ® M5571, n.d.

[48] G.A. Truesdale, A.L. Downing, Solubility of Oxygen in Water, Nature 173 (1954) 1236.

[49] I.W. Huang, B.L. Hurley, F. Yang, R.G. Buchheit, Dependence on Temperature, pH, and Cl- in the Uniform Corrosion of Aluminum Alloys 2024-T3, 6061-T6, and 7075-T6, Electrochim Acta 199 (2016) 242–253. https://doi.org/10.1016/j.electacta.2016.03.125.

[50] C.N. Panagopoulos, E. Georgiou, K.I. Giannakopoulos, P.G. Orfanos, Effect of ph on stress corrosion cracking of 6082 al alloy, Metals (Basel) 8 (2018). https://doi.org/10.3390/met8080578.

[51] W.-T. Tsai, J.-B. Duh, J.-J. Yeh, J.-T. Lee, Y.-C. Chang"', Effect of pH on Stress Corrosion Cracking of 7050-T7451 Aluminum Alloy in 3.5 wt% NaCl Solution *, 1990. http://meridian.allenpress.com/corrosion/article-pdf/46/6/444/1530787/1_3585130.pdf.

[52] Z. Dan, I. Muto, N. Hara, Effects of environmental factors on atmospheric corrosion of aluminium and its alloys under constant dew point conditions, Corros Sci 57 (2012) 22–29. https://doi.org/10.1016/j.corsci.2011.12.038.

[53] T.F. Cui, D.X. Liu, P.A. Shi, J.J. Liu, Y.H. Yi, H.L. Zhou, Effect of NaCl concentration, pH value and tensile stress on the galvanic corrosion behavior of 5050 aluminum alloy, Materials and Corrosion 67 (2016) 72–83. https://doi.org/10.1002/maco.201408189.

[54] E. Bumiller, INTERGRANULAR CORROSION IN AA5XXX ALUMINUM ALLOYS WITH DISCONTINUOUS PRECIPITATION AT THE GRAIN BOUNDARIES A Dissertation Presented to, 2011.

[55] J.A. Lyndon, R.K. Gupta, M.A. Gibson, N. Birbilis, Electrochemical behaviour of the β-phase intermetallic (Mg2Al3) as a function of pH as relevant to corrosion of aluminium-magnesium alloys, Corros Sci 70 (2013) 290–293. https://doi.org/10.1016/j.corsci.2012.12.022.

[56] B. Zaid, D. Saidi, A. Benzaid, S. Hadji, Effects of pH and chloride concentration on pitting corrosion of AA6061 aluminum alloy, Corros Sci 50 (2008) 1841–1847. https://doi.org/10.1016/j.corsci.2008.03.006.

[57] C.B. Crane, R.G. Kelly, R.P. Gangloff, Crack chemistry control of intergranular stress corrosion cracking in sensitized Al-Mg, in: Corrosion, National Assoc. of Corrosion Engineers International, 2016: pp. 242–263. https://doi.org/10.5006/1852.

Chapter 6: Conclusions and Future Work

In summary of the work presented above, there are several major findings of Alloy 1. First, there is a moderate level of grain directionality of Alloy 1, which resulted in little effect on crack growth kinetics of in-plane loading orientation study. To determine this, grain microstructures were obtained and grain sizes were measured. A linear elastic fracture mechanics-based testing approached showed no change in intergranular stress corrosion cracking susceptibility in the L-T and T-L loading orientations, which was explained by the negligible difference in crack path tortuosity. In addition, the amount of beta phase was measured using a pixel-based measurement of amount of beta phase on the grain boundaries. It was found that the as-received material had similar amounts of grain boundary beta phase as the sensitized condition. However, the crack growth kinetics of the sensitized Alloy 1 were faster than the as received condition, marking some change in the IGSCC propagation when the alloy was sensitized.

Through an explicit study of the applied potential dependence of Alloy 1, it was determined that the mechanism of crack growth was the same as other Al-Mg alloys which had the same applied potential dependence, pointing towards the anodic dissolution enabled hydrogen embrittlement crack growth mechanism. This study showed a decreased susceptibility of Alloy 1 with increasing applied cathodic overpotential (decreasing the applied potential). A distinct full mitigation of crack growth was achieved at potentials below the beta breakdown potential.

In a more relevant solution environment, Alloy 1 had increased IGSCC susceptibility when a benign solution (low chloride containing, slightly basic pH) water layer thickness decreased (going from full immersion to an atmospheric environment). This was explained by the increase in available cathodic current necessary to supply the anodic reactions at the crack tip. It was concluded that a combination of the benign solution chemistry and atmospheric environment increases the IGSCC susceptibility of Alloy 1. However, when subjected to different solution chemistries in atmospheric environments, Alloy 1 susceptibility is bounded by the most acidic solution chemistry (more aggressive crack growth kinetics – most susceptible) and the least chloride containing solution (least susceptible). In conclusion, Alloy 1 has crack growth kinetics that are sensitive to both changes in electrolyte geometry and electrolyte chemistry.

All of the work presented does leave some knowledge gaps in terms of the IGSCC susceptibility of Alloy 1. The following questions can be thought of as starting points for future work to follow:

1. What are the changes in beta morphology from the as received condition to the sensitized condition, and how can they be characterized?

2. As a related question, what is the reason for an increase in Stage II crack growth kinetics of the sensitized Alloy 1 compared to the as received?
3. Why is the full mitigation of crack growth of Alloy 1 at applied potentials lower than for other Al-Mg alloys?
4. Can the operative mechanism for available cathodic current be predicted in an atmospheric environment? For more context, it should be noted that the available cathodic current can either be influenced by the water layer thickness (as was the case for Alloy 1) to increase IGSCC susceptibility, or by the ohmic drop (as was the case for other Al-Mg alloy) to decrease IGSCC susceptibility.
5. Does the solution conductivity contribute to the increased IGSCC kinetics of Alloy 1 exposed to benign solution chemistries in an atmospheric environment?
6. What are the reasons for the differences in misting vs. wicking atmospheric conditions, and why do they exist?

Some suggestions for future testing would be to gather TEM images for the as received and sensitized conditions of Alloy 1 and note any differences on the beta phase precipitation, which were not captured in the linear grain boundary beta study. In order to study the effect of the applied potential on the full mitigation of IGSCC of Alloy 1, a loading orientation study should be completed at the same loading rate as other Al-Mg alloys, and differences should be noted. In order to determine the role of the atmospheric environment to predict increases or decreases in IGSCC susceptibility, the solution conductivity could be predicted using OLI and therefore the relative conditions of the crack tip could be simulated. This could be one way to explain differences in how the available cathodic current is affected. Lastly, more studies are needed to determine the differences in the misting and wicking atmospheric environments, one first step would be to complete this test with changing solution chemistry and note significant differences.